NASA CONTRACTOR
REPORT

N73-23938

NASA CR-2241

NASA CR-2241

NET VAPOR GENERATION POINT IN BOILING FLOW OF TRICHLOROTRIFLUOROETHANE AT HIGH PRESSURES

by R. S. Dougall and T. E. Lippert

Prepared by
UNIVERSITY OF PITTSBURGH
Pittsburgh, Pa. 15213
for Lewis Research Center

NATIONAL AERONAUTICS AND SPACE ADMINISTRATION • WASHINGTON, D. C. • MAY 1973

1. Report No.
NASA CR-2241

2. Government Accession No.

3. Recipient's Catalog No.

4. Title and Subtitle
NET VAPOR GENERATION POINT IN BOILING FLOW OF TRICHLOROTRIFLUOROETHANE AT HIGH PRESSURES

5. Report Date
May 1973

6. Performing Organization Code

7. Author(s)
R. S. Dougall and T. E. Lippert

8. Performing Organization Report No.
None

10. Work Unit No.

9. Performing Organization Name and Address
University of Pittsburgh
Pittsburgh, Pennsylvania 15213

11. Contract or Grant No.
NGL 39-011-079

13. Type of Report and Period Covered
Contractor Report

12. Sponsoring Agency Name and Address
National Aeronautics and Space Administration
Washington, D. C. 20546

14. Sponsoring Agency Code

15. Supplementary Notes
Project Manager, Yih-Yun Hsu, Physical Science Division, NASA Lewis Research Center, Cleveland, Ohio

16. Abstract

The conditions at which the void fraction in subcooled boiling starts to undergo a rapid increase were studied experimentally. The experiments were performed in a 12.7x9.5 mm rectangular channel. Heating was from a 3.2 mm wide strip embedded in one wall. The pressure ranged from 9.45 to 20.7 bar, mass velocity from 600 to 7000 kg $m^{-2}s^{-1}$, and subcooling from 16 to 67 C. Photographs were used to determine when detached bubbles first appeared in the bulk flow. Measurements of bubble layer thickness along the wall were also made. Results showed that the point of net vapor generation is close to the occurrence of fully-developed boiling.

17. Key Words (Suggested by Author(s))
Two-phase flow; Flow boiling; Freon-113; Net vapor generation

18. Distribution Statement
Unclassified - unlimited

19. Security Classif. (of this report)
Unclassified

20. Security Classif. (of this page)
Unclassified

21. No. of Pages
90

22. Price*
$3.00

* For sale by the National Technical Information Service, Springfield, Virginia 22151

NET VAPOR GENERATION POINT IN BOILING FLOW OF TRICHLOROTRIFLUOROETHANE AT HIGH PRESSURES

by R. S. Dougall and T. E. Lippert

University of Pittsburgh

SUMMARY

The conditions at which the void fraction in subcooled boiling starts to undergo a rapid increase (point of net vapor generation) were studied experimentally using trichlorotrifluoroethane (R-113 or Freon-113) as the fluid. The flow regime was a bubbly flow. The experiments were performed in a rectangular channel, 12.7x9.5 mm in cross section. Heating was from a 3.2 mm wide strip embedded in the longer side of the channel. The pressure range studied was from 9.45 to 20.7 bar, mass velocities from 600 to 7000 kg m^{-2}s^{-1}, and subcoolings from 16 to 67 C. Photographs were used to determine when detached bubbles first appeared in the bulk flow. Measurements of bubble layer thicknesses along the wall were also made.

Two current theories of bubble detachment (or point of net vapor generation) were evaluated based on the data obtained in this study. The first theory was based on a bubble-force model which contained an empirical factor (contact angle parameter) that was assumed to remain constant. The experimental data show that this assumption is incorrect. The data also show the theory to be inconsistent with the actual behavior of the contact angle parameter Furthermore, the agreement between theory and experiment is only fair. The second theory was based on an energy-transport model. The data were within ±25 percent of this theory at low and moderate pressures. This agreement is within the experimental uncertainty expected. The high pressure data showed slightly larger errors.

A correlation of the present test data was obtained relating the point of bubble detachment (or point of net vapor generation) with a subcooling parameter, S. The equation is:

$$q''_d = S\, q''_{fdb}$$

where q''_d and q''_{fbd} are the detachment and fully-developed boiling heat-flux values, respectively, at a given wall superheat. The product $S \cdot q''_{fbd}$ defines a line that falls parallel to the fully-developed boiling curve and represents the locus of all bubble detachment points for a given pressure and subcooling. Then, for a given flow velocity, bubble detachment corresponds to the intersection of the local boiling curve with the $S \cdot q''_{fbd}$ line.

The subcooling parameter S is given by:

$$S = 1 + 0.0417\left(h_{fg}/c_p \Delta T_{sub}\right)^{1.432}$$

and is a function only of system pressure and subcooling. This equation was determined from a least square fit of some 29 data points and encompasses three pressure levels and a wide range of flow conditions. The correlation does not apply to very low subcoolings and additional data is needed in this region.

The bubble boundary-layer thickness at the onset of detached voidage was measured and found to depend primarily on mass velocity and only slightly on subcooling. The subcooling dependency was shown to agree with prior water studies. A correlation of the present experimental results was obtained which agreed with the data to ±30 per cent.

INTRODUCTION

Boiling heat transfer has come under considerable interest in recent years because of the many engineering applications in which high heat-transfer rates are required at modest temperature differences. Applications include such systems as nuclear reactors and rocket motors where heat transfer rates of the order of 500 to 5000 kW m^{-2} are common. Boiling is also important in boilers, evaporators, and more recently in the cooling of high-speed computer components. In this last example, the heat fluxes are modest, but the requirements of a reasonably uniform heated surface temperature is achieved by operating under boiling conditions in the cooling channels (ref. 1). The performance of each of these systems depends extensively on the heat-transfer process. Since higher performance from existing systems is an economical necessity and with the continual development of new systems, there is a need for the continual broadening of the engineer's understanding of all aspects of the boiling heat-transfer process.

One of the areas that has not been adequately described is the conditions under which the void fraction in subcooled boiling starts to undergo a rapid increase (point of net vapor generation). The flow structure of subcooled boiling is dependent on the subcooling of the liquid (T_s-T_b). At high liquid subcoolings, the bubbles are small and remain attached to or slide along the heating surface. The average void fraction is small and frequently the density of the fluid is assumed to be approximately that of a single-phase liquid. This regime is often referred to as wall voidage. As subcooling decreases or heat flux increases, the bubbles become larger and begin to detach from the wall and move into the bulk fluid. This flow regime is now called detached voidage, and the local void fraction begins to increase much more rapidly. A schematic representation of wall voidage and detached voidage is shown in Figure 1.

There are several semi-analytical techniques for predicting void fraction in the detached voidage region (refs. 2 to 4). The accuracy of these predictions, as pointed out by Bergles et al (ref. 1), is contingent on having an accurate assessment of the bubble-detachment point (point B in figure 1, often called the point of net vapor generation). In this work, the effort was aimed at determining the character of the wall voidage and in evaluating the bubble-detachment point as a function of system parameters. The experimental data include photographs of the bubbles, measurement of the wall heat flux, system pressure flow rate, and bulk liquid temperature. From the photographs, measurements of the bubble layer are made and evaluated. The data encompasses a relatively wide range of system parameter, allow an evaluation of the physical character of the bubble layer, and yield an assessment of the different theories used for predicting the point of bubble detachment.

Many of the applications involving boiling heat transfer employ water as the working medium (e.g. pressurized and boiling water reactors), but some of the experimental investigations are done with fluids other than water. Results are then interpreted or modeled to fit the water systems based on one or more scaling parameters between water and the actual test fluid. The results reported in this investigation were conducted using refrigerant-113 (also known as R-113, Freon-113, Genetron-113 and trichlorotrifluoroethane). This fluid is useful as a modeling fluid for water because it has a much lower critical pressure and much smaller latent heat. Both of these factors make tests much easier and less expensive than corresponding water tests.

THEORIES OF BUBBLE DETACHMENT

In subcooled forced convection boiling there can exist four distinct regions as schematically illustrated in figure 1. To the left of point A, the flow is single phase. From A to C, the bulk liquid is subcooled, where from A to B, the bubble structure is described as attached voidage and detached voidage from B to C. To the right of C, the bulk liquid is at the saturation temperature. Point A is the inception of boiling, B is called the point of net vapor generation, and C the onset of bulk boiling. In the attached voidage region, the thickness of the superheated liquid layer close to the wall is small, and the bubbles cannot grow to any reasonable size. The void fraction is small. At point B, the first bubbles detach from the heated wall, and the vapor volumetric fraction thereafter begins to increase rapidly. From B to C the bulk flow is in non-thermal equilibrium, and the local vapor weight fraction is higher than would be calculated from a heat balance. At C, thermal equilibrium conditions have been established in the main flow.

Although the particulars of the flow details may vary from one application to the next, the general applicability of the four regions is well documented. Obviously, the particular value of the void fraction at a given point along the channel length is not known unless the transverse voidage profile curve can be predicted for the particular geometry. A knowledge of the amount of vapor present in the channel is required to enable the accelerative and static head components of the pressure gradient to be calculated. In the particular case of the design of liquid-cooled nuclear reactors, information on the void fraction under subcooled conditions is often required because of its influence upon the reactivity of the system. Only recently has the analysis and data on transverse void profiles become prevalent in the literature. A brief review of some of this work follows.

Griffith, Clark, and Rohsenow (ref. 2) from a photographic study of subcooled boiling identified the two distinct bubble regions (as previously described). Their calculation scheme in the attached voidage region assumes that no significant fraction of the wall heat flux is used in the formation of net vapor. The total heat flux supplied to the surface is assumed to be in part removed by single phase forced convection, and in part by subcooled nucleate boiling. In the detached subcooled region, they consider a net vapor generation in the heat balance and assume a constant condensing film coefficient. The transition from attached to detached voidage is taken as that point where 80 percent of the surface heat flux goes into steam generation.

Bowring (ref. 5) offers a comprehensive development of an empirical method of calculating void fraction. The model neglects fractional changes in the bubble volume due to condensation. Heat is assumed to be removed by convection caused by bubble agitation, by single phase heat transfer, and by latent heat. The development leads to relationships for predicting the void fraction and also for calculating the point of net vapor generation. Bowring's model adequately predicts the high pressure water data reported in reference 6 but overestimates the void fraction at the low mass velocities. The subcooling at the point of bubble detachment is given by:

$$\Delta T_{sub,d} = \eta \frac{q''}{u_f}$$

where η is an empirical factor derived from experimental data with water and found to depend only on the system pressure.

Zuber, Staub, and Bijward (ref. 7) in their model postulate a profile for the liquid temperature during non-thermal equilibrium conditions and derive an expression for the void fraction which accounts for the vapor concentration profile across the flow duct and the local relative velocity between the two phases. The analysis does not prescribe an expression for obtaining the transition points.

The model of Thom et al (ref. 8) relates the subcooled void fraction to a reduced steam quality defined in terms of the fluid enthalpy at the start of the detached subcooled voidage. The fluid enthalpy at the detachment point is related to the enthalpy of the saturated liquid (water) by an empirical relation.

Levy (ref. 3) develops a model by postulating a relation between the true local vapor weight fraction and the corresponding thermal equilibrium value. The vapor volumetric fraction is obtained from the true local vapor weight fraction and an accepted relationship between vapor weight fraction and volumetric fraction. The test data shows best agreement over the lower mass velocity range.

Rouhani (ref. 9) uses theoretical arguments leading to equations for the calculation of volume fraction and true liquid subcooling. It is assumed that heat is removed by vapor generation, heating of the liquid that replaces the detached bubbles, and to some extent by single-phase heat transfer. Condensation of vapor in the subcooled liquid is analyzed, and the relative velocity of vapor with respect to the liquid is neglected. Both regions of subcooled boiling, attached and detached voidage, are analyzed and the transition point located. The agreement between the calculated and measured data is good, in some cases, but will not yield satisfactory results in the case of very low mass velocity.

Larson and Tong (ref. 4) present a semi-analytic model for the prediction of void fraction. The model is based on the formation and growth of a bubble boundary layer adjacent to the heated surface at a rate determined by the difference between the imposed surface heat transfer and the heat removal capability of the subcooled liquid core of the flow. The latter heat transfer rate is determined by the analogy between heat and momentum transfer in the liquid employing empirical friction factor data for low-quality two-phase flow. The model provides for evaluating the point of net vapor generation.

Each of the models discussed above gives a means for calculating the void fraction growth in subcooled flow boiling, and each shows experimental data in support of their model, at least over a limited range of operating conditions. However, the accuracy of these models inherently depends on an accurate assessment of the point of net vapor generation, point B, figure 1. This then fixes the void growth curve. In each of the models discussed, the authors use various degrees of sophistication to define this point. In some of the models, the criteria for bubble detachment is based solely on prior data and/or empirical equations, while in others, more analytical approaches are attempted. The empirical relations generally apply only to one fluid. The more analytical approaches usually involve one or more empirical constants, the nature of which are essentially untested, except for water.

In more recent papers, efforts have been directed toward quantitatively describing bubble detachment in subcooled forced convection boiling. This work has led to more general type equations. The ones considered herein are the works of Staub (ref.10), Levy (ref. 3) and Larson and Tong (ref. 4). Both Levy and Staub, in similar treatments, consider the details of the forces acting on individual bubbles to establish criteria for detachment, while Tong takes a more macroscopic treatment of the bubbles but considers the details of the heat transfer mechanism in the bubble layer. A review of the details of these models follow.

Staub's model is a modification and extension of Bowring's work and allows for the prediction of the net vapor generation point as a function of fluid transport properties, geometry, and liquid velocity. The equations take into account the liquid temperature profile and the convective shear effects on the bubbles attached to the heated wall. Physically, Staub argues that the beginning of detached voidage occurs when the point is reached where the mean bubble population diameter is large enough to allow this bubble size to detach from, or slide along, the heated surface. Since the wall superheat is sufficient to allow nucleation, new bubbles are rapidly created at these sites. From this reasoning, according to Staub, a less empirical formulation for $\Delta T_{sub,d}$ (departure subcooling) must include: a set of relations governing the mean population diameter of the departing bubbles, and a method for calculating the local subcooling at which this mean departure diameter exists. To formulate an expression for mean departure diameter, Staub considers a force balance on an individual bubble. The geometry assumes essentially hemispherical bubbles on a vertical wall. However, a contact angle not necessarily 90 degrees is assumed to exist where the bubble contacts the wall. The forces acting on a bubble attached to the surface include surface tension, dynamic force due to the momentum change of the liquid resulting from the growing bubble (the comparable vapor force is small), dynamic force due to liquid inertia (vapor inertia neglected), vapor thrust force, buoyancy, and drag force. The vapor thrust force, liquid momentum change force, and the liquid inertia force are reported by Staub to be negligible near the bubble departure point. Remaining is a balance of the surface tension, buoyancy, and drag forces. These are written:

Surface tension, $F_{st} = \pi D_d \sigma f(\beta)$

where f(β) is the bubble contact angle function;

Buoyancy, $F_B = \frac{1}{12} \pi D_d^3 (\rho_f - \rho_g) g$

and

Drag, $F_D = \frac{1}{32} \pi f u_{fi}^2 \rho_f D_d^2$

An averaging process is assumed for the drag force in that the surface is considered to be well covered by a bubble layer whose bubbles can be represented by a mean departure diameter D_d. The correct friction factor is calculated by employing a surface roughness equivalent to

$$\frac{e}{D_e} = \frac{D_d}{2\,D_e}$$

in conjunction with the liquid bulk inlet velocity, u_{fi}. Writing the force balance gives after some rearrangement:

$$\frac{f\,\rho_f\,u_{fi}^2\,D_d}{32\,\sigma\,f(\beta)} + \frac{(\rho_f - \rho_g)\,g\,D_d^2}{12\,\sigma\,f(\beta)} = 1.0 \qquad (1)$$

After Fritz (ref. 11) Staub assumes that f (β) is not velocity dependent and takes its value as approximately 0.03. Thus, the mean diameter of the departing bubble size can be predicted. Now, it becomes necessary to calculate the mean bulk temperature of the liquid to obtain the local subcooling. To calculate this quantity, the liquid temperature profile outside the bubble layer, whose thickness is defined as $D_d/2$, is assumed the same as the temperature profile for single-phase flow, i.e., established turbulent flow with an eddy diffusivity ratio of 1.0. The liquid temperature at a distance $D_d/2$ from the wall is taken equal to the saturation temperature. Staub's analysis leads to the following expressions for evaluating liquid subcooling at bubble departure:

Laminar sublayer $0 < Y_d^+ < 5$

$$\theta_d = \left[\frac{\Delta T_{sub}}{q''}\right]_d = \frac{1}{c_f\,\rho_f\,u_{fi}\sqrt{f/8}}\left\{P_r\,(5 - Y_d^+) + 5\,\ln(1 + 5P_r) + 2.5\left[\frac{\ln Y_d^+/30}{1 - 30/Y_d^+} - 1\right]\right\} \qquad (2)$$

Buffer layer $5 < Y_d^+ < 30$

$$\theta_d = \frac{1}{c_f \rho_f u_{fi} \sqrt{f/8}} \left\{ 5 \ln \frac{1 + 5 P_r}{1 + P_r (Y_d^+/5 - 1)} + 2.5 \left[\frac{\ln Y_{cl}^+/30}{1 - 30/Y_{cl}^+} - 1 \right] \right\} \tag{3}$$

Turbulent core $30 < Y_d^+$

$$\theta_d = \frac{2.5}{c_f \rho_f u_{fi} \sqrt{f/8}} \left[\frac{\ln Y_{cl}^+/Y_d^+}{1 - Y_d^+/Y_{cl}^+} - 1 \right] \left[1 - \frac{Y_d^+}{Y_{cl}^+} \right] \tag{4}$$

where

$$Y_d^+ = \frac{(D_d/2) \rho_f u_{fi} \sqrt{f/8}}{\mu_f} \tag{5}$$

and

$$Y_{cl}^+ = \frac{(D_e/2) \rho_f u_{fi} \sqrt{f/8}}{\mu_f} \tag{6}$$

For a given fluid, specified inlet velocity and the specified local heat flux, a solution for $\Delta T_{sub,d}$ is obtained by first calculating D_d from equation (1). This fixes the value of Y^+_d, equation (5). Then, corresponding to the location of Y^+_d, laminar sublayer, buffer layer or turbulent core, equation (2), (3), or (4) is employed to calculate θ_d.

Levy (ref. 3) presents a similar model but the drag controlled term in equation (1) is based on a single-phase friction factor. With Staub (ref. 10) the force balance is based on a bubble layer, and the greater friction factor and heat transfer coefficient associated with this layer is employed.

Larson and Tong (ref. 4) do not attempt to describe the dynamics of the bubble growth and motion. Rather, they concentrate on determining the energy and enthalpy fluxes in the flow. It is assumed that the imposed wall heat flux, q''_w, is transmitted across the bubble layer by liquid convection and latent heat transport within the bubbles to the liquid core-bubble layer interface. At this point, a portion of the heat transfer, q''_1, causes a net vapor formation contributing to the bubble boundary-layer growth, while the remaining portion $q''_2 = q''_w - q''_1$ is transmitted to the subcooled liquid core contributing to decreasing its subcooling. The liquid core consists of subcooled (or saturated) liquid in developed turbulent motion, the core-bubble layer interface being kept at the saturation temperature. The analysis is based on a differential-integral formulation that considers separately the continuity and energy equations for the bubble layer and liquid core. The formulation is reduced to three coupled nonlinear first order differential equations that are functions of wall heat flux q''_w and the liquid core heat transfer q''_2. The specific form of the differential equations depend on the test section geometry. The key to the model is evaluation of the heat transfer to the liquid core, q''_2, which is based on (a) quasi-developed turbulent flow, (b) the analogy between heat and momentum transfer, and (c) the use of empirical friction factor data from low-quality two-phase flow. This last criteria has been slightly modified herein to adjust for an asymmetric geometry.

The analysis for the present rectangular test geometry is summarized. The procedure and assumptions are essentially that of Larson and Tong, but the equations have been appropriately adjusted to reflect the rectangular geometry and asymmetric heating. The assumed physical geometry and accompanying nomenclature is given in figure 2. The conservation of mass equations for the bubble boundary layer and subcooled liquid core, are written; respectively,

$$\frac{d}{dz}\int_{H-\delta}^{H} \rho_b u \, dx - \dot{m}''_z = 0 \qquad (7)$$

$$\frac{d}{dz}\int_{0}^{H-\delta} \rho_f u \, dx + \dot{m}''_z = 0 \qquad (8)$$

where m_2'' is the mass flux from the subcooled liquid core to the bubble layer, and u is the local axial velocity. The respective energy equations for the bubble boundary layer and the subcooled liquid core are written,

$$\frac{d}{dz}\int_{H-\delta}^{H} \rho_b u h_b \, dx - m_2'' h_f = (q_w'' - q_z'') \tag{9}$$

$$\frac{d}{dz}\int_{0}^{H-\delta} \rho_f c_f T u \, dx + m_2'' h_f = q_z'' \tag{10}$$

where h is the enthalpy and T temperature. The conditions on T, u and ρ_b are approximated in the integrals in equations (7) to (10) by the following substitution:

$$u(T_s - T)_{CORE} = K_T u_{cl} (T_s - T_{cl})$$

$$u = u_{cl} \quad \text{for} \quad 0 < x < (H-\delta)$$

$$u = K_b u_{cl} \quad \text{for} \quad (H-\delta) < x < H$$

$$\rho_b \neq f(x) \quad \text{for} \quad (H-\delta) < x < H$$

where K_T and K_b are constants and u_{cl} and T_{cl} are the average velocity and temperature for the core liquid. Applying the above condition to equations (7) and (8), integrating and then combining to eliminate m_2'' yields, for the continuity equation,

$$\frac{d}{dz}\left\{\rho_f u_{cl} H \left[1 + \frac{\delta}{H}\left(K_b \frac{\rho_b}{\rho_f} - 1\right)\right]\right\} = 0 \tag{11}$$

where ρ_b is given by

$$\rho_b = \rho_f (1 - \alpha_b) + \rho_g \alpha_b$$

Integrating the energy equations (9) and (10) gives for the bubble boundary layer and subcooled liquid core, respectively,

$$\rho_b K_b (h_b - h_f) \frac{d}{dz} (u_{cl} \delta) = q_w'' - q_2'' \qquad (12)$$

and,

$$\rho_f K_T \frac{d}{dz} \left[u_{cl} (T_{cl} - T_s)(H - \delta) \right] = q_2'' \qquad (13)$$

Equations (11), (12), and (13) constitute three differential equations to solve for the four unknowns u_{cl}, δ, q_2'' and T_{cl}. A relationship for q_2'', is needed. To evaluate q_2'', the heat flux to the liquid core, the momentum and heat flux equations in the turbulent core are written in the usual form:

$$\tau/\rho_f = (\nu + \epsilon_M) \frac{du}{dx} \qquad (14)$$

and

$$q''/\rho_f c_f = -(\alpha_H + \epsilon_H) \frac{dT}{dx} \qquad (15)$$

where ν, α_H and ϵ_m, ϵ_H represent the molecular and eddy diffusivities in the liquid core, respectively, for momentum and heat. Ignoring molecular diffusion, dividing equations (15) by (14) and incorporating the turbulent Prandtl number ($P_T = \epsilon_m/\epsilon_H$), gives the following expression for q_2''.

$$q_2'' = -\frac{\tau c_f}{P_T} \frac{dT}{du} \cong \frac{\tau_2 c_f}{P_T} \left[\frac{T_s - T_{cl}}{u_{max} - u_2} \right] \qquad (16)$$

where u_2 is the velocity at $y = \delta$.

Following Schlichting (ref.12), the shear stress is written for the present geometry,

$$\tau = \tau_w \left(1 - \frac{2y}{H} \right) \tag{17}$$

The Prandtl universal velocity distribution law is written as:

$$u_{max} - u = \frac{u^*}{K} \ln \left(\frac{H}{2y} \right) \tag{18}$$

where the friction velocity u* is given by

$$u^* = \sqrt{\tau_w / \rho} \tag{19}$$

Evaluating the above equation at the bubble layer-liquid core interface gives

$$u_{max} - u_2 = \frac{u^*}{K} \ln \left(\frac{H}{2\delta} \right) \tag{20}$$

Eliminating $u_{max} - u_2$ from equation (16) gives for q_2'':

$$q_2'' = \frac{\rho_f c_f}{P_T} \cdot \frac{u^* K (T_s - T_{cl})(1 - \frac{2\delta}{H})}{\ln (H/2\delta)} \tag{21}$$

The friction velocity u*, again following Larson and Tong, is evaluated in terms of the two-phase friction factor f_{tp} defined as

$$f_{tp} = 8 \tau_w / (\rho_f u_{tp}^2) = \frac{8 u^{*2}}{u_{tp}^2} \tag{22}$$

where

$$u_{tp} = \frac{G}{\rho_f(1-\alpha)} \qquad (23)$$

and α is the average void fraction which for the present geometry is related to the bubble layer void fraction, α_b, by

$$\alpha = \alpha_b \frac{\delta b}{H w} \qquad (24)$$

Tong uses an empirical relation for f_{tp} given by

$$f_{tp} = C_2 \, Re_{tp}^{-n} \qquad (25)$$

where

$$Re_{tp} = \rho_f u_{tp} D_e / \mu_f$$

Considering the asymmetric heating arrangement in the present test section, the friction factor is calculated from turbulent flow considerations and equation (25) but weighted according to the ratio of heated to wetted perimeter, i.e.,

$$\bar{f} = \frac{P_W}{P_T} f_t + \frac{P_H}{P_T} f_{tp} \qquad (26)$$

where P_T is the total wetted perimeter, P_W the wetted perimeter that sees no bubbles, and P_H is the heated perimeter. f_{tp} is calculated from equation (25) with $C_2 = 16.5$ and $n = 0.6$ and f_t from the usual turbulent flow equation

$$f_t = \frac{0.046}{Re_{tp}^{0.20}} \qquad (27)$$

A graphical representation of $\bar{f}$ is given in figure 3.

With this definition of the friction factor, the friction velocity is written:

$$u^{*} = u_{fi}\sqrt{\bar{f}/8}\Big/\left[1 - \alpha_b \frac{\delta b}{H w}\right] \tag{28}$$

where b is the width of the heating strip.

Substituting equation (28) into equation (21) gives q_2'',

$$q_2'' = \frac{\rho_f c_f K \sqrt{f/8}\left(1 - \frac{2\delta}{H}\right) u_{fi} \Delta T_{sub}}{P_T \left(1 - \alpha_b \frac{\delta b}{H w}\right) \ln\left(\frac{H}{2\delta}\right)} \tag{29}$$

where $(T_s - T_{cl})$ is approximated by ΔT_{sub}. According to Larson and Tong, whenever $q_2''/q_w'' \geq 1$, the bubble layer is suppressed corresponding to attached voidage. The onset of significant void formation occurs once $q_2''/q_w'' < 1$. Thus, the bubble detachment criteria becomes,

$$q_w'' - q_2'' = 0 \tag{30}$$

Therefore, the wall heat flux at bubble detachment becomes,

$$q_w''\Big|_d = q_d'' = q_2''\Big|_d = \frac{\rho_f c_f K \sqrt{f/8}\left(1 - \frac{2\delta_d}{H}\right) u_{fi} \Delta T_{sub}}{P_T\left(1 - \alpha_b \frac{\delta_d b}{H w}\right) \ln\left(\frac{H}{2\delta_d}\right)} \tag{31}$$

where the subscript d refers to bubble detachment conditions.

EXPERIMENTAL APPARATUS

The R-113 was contained in a closed loop system and circulated using a canned rotor, centrifugal pump. The pump delivered a head in excess of 5 bar. The main loop piping was 25.4mm diameter type 304 stainless steel tube. A schematic of the loop is shown in figure 4.

As shown, the flow would proceed from the pump through the lines into a horizontal preheater (item 2). The preheater had the capability of producing a total of 25 kw of power. This power was provided by five Chromolox immersion heaters, each with a rated output of 5 kw at 240 Volts. Four of the heaters were connected as either simply on or off, depending on the amount of heat needed. The remaining heater was connected to a variable transformer and used for the fine control.

From the preheater, the flow would divide and some pass through a standard A.S.M.E. venturi flow measuring meter (item 3) and then through the main throttling valve and into the test section (item 4) while the latter flow proceeds through a by-pass line (item 5) and then rejoins the test section flow prior to entering the coolers. The quantity of flow entering the test section was controlled by the throttling valve on the by-pass line and with the main throttling valve which was located upstream of the entrance of the test section. This arrangement permitted adjustment of the pressure drop taken at the test section.

After rejoining, the flow would enter two helical concentric tube single pass heat exchangers (item 6). Cooling water was provided directly from the city line and controlled with a valve. From the coolers, the R-113 flow would enter the suction side of the pump. A Sprolan high water capacity filter (item 7) was incorporated on a by-pass line at the suction side of the pump.

The system pressure was maintained by a separate pressurizing unit that had a capacity of about 21 liters (item 8). The fluid in this unit was maintained at saturation by heating it, using a 5 kw Chromolox immersion heater whose power output was controlled with a variable transformer. The liquid level in the pressurizer was monitored by visual observation through a sight gage (item 9). The unit was controlled automatically by a temperature controller (Assembly Products Model 429). A bourdon tube type gage 0-70 bar was used to measure the loop system pressure at the outlet of the pump. Pressure at the suction side of the pump was also monitored.

Provided on the loop were two safety relief valves. One was a 48 bar blowout disk (item 10). The second was a pressure regulator relief valve that could be set to any pressure up to 27 bar (item 11).

The test section was 1.32 meter long rectangular duct 12.7 by 9.5mm through which R-113 (Trichlorotrifluoroethane) was circulated and heated from one side wall. A photograph of the section assembly is shown in figure 5. The duct was vertically orientated in the flow loop with the R-113 flowing against gravity. The channel assembly consisted of an inlet transition section, a heated section, and an unheated exit section. The transition section extended approximately 45 diameters upstream of the heated portion of the test section and was designed to allow a smooth flow transition from the 25.4 mm diameter circular tubing to the rectangular geometry of the duct. The transition section helped to dampen out flow disturbances that were caused by pipe fittings and allowed for a fully-developed velocity profile at the beginning of the heated length. The heated section was 0.526 m long and of the same rectangular geometry as the transition section. The exit section extended approximately 28 diameters downstream of the exit of the heated length.

The test section assembly was constructed from a 140 bar stainless steel sight gage so visual observation of the flow was possible. This was accomplished by slightly modifying the side window construction of the sight gage. Actually, the windows had been constructed from two separate pieces of glass, as seen from the fanned view of the section assembly in figure 6. The 3.2 mm thick inside pieces of glass formed the two opposite side walls of the channel. Each of these pieces of glass had been chemically pre-stressed for high tensile strength to resist cracking at high temperature. The 19 mm thick back support pieces were high pressure gauge glass. These pieces sealed the section by pressing against gaskets made of Durable when the steel frames of the housing were tightly bolted together. There were two viewing windows on each of the two sides of the duct, each measuring 32 mm by 350 mm. The third wall of the duct corresponds to the inside portion of the sight gage. The fourth side, the heated wall of the duct, contained a stainless steel strip, 3.2 mm wide, 0.80 mm thick, and 510 mm long imbedded in and bonded to a 6.4 mm thick piece of fibrous impregnated plastic insulating material (Lamitex). The insulation was in turn bonded to the sight gage wall. The heating strip was also brazed at both ends to small brass support blocks. Copper electrodes were threaded into each of these supports. The electric power was supplied by a continuous duty selenium rectifier with a rated dc output of 18 volts, 200 amperes. The electrical leads to the heating strip were passed through the test section housing wall by employing Conax pressure glands that threaded into the steel housing.

Actually, three different stainless steel heating strips were tested. Each was of the same geometry, but with two of them, thermocouples had been attached to the back side of the strip in an effort to obtain the temperature of the heated wall surface. In one case, the thermocouples were tack welded directly to the back of the strip, while in the second design the thermocouples were press fitted against the back of the strip but electrically insulated from it by a 0.127 mm thick strip of mica. (This design proved inadequate.) The third design had no thermocouples attached to the heating strip.

The test section assembly and adjacent piping were insulated prior to testing with several layers of 50 mm thick spun fiberglass (except for the glass window portion of the test section). This minimized the heat loss from the section assembly. The heat loss from the back side of the stainless steel strip was calculated to be less than one percent.

The basic measurements made on the test section include: section pressure, the inlet and outlet centerline fluid temperature, flow rate of the R-113, and the voltage and current through the heating strip. From these measurements all the system variables and test quantities were calculated or derived. An estimate of the error involved in these measurements is given below. The subsequent cumulative effect of these errors on the derived quantities is given in the Error Analysis section, Appendix A.

The test section pressure was measured from a 3.2 mm tap located approximately 127 mm from the inlet of the heated portion of the duct. This pressure was recorded with a Bourdon type pressure gage 0-500 psi in 5 psi sub-division, U.S. Gauge Model Number 19011. The gage had been calibrated using a double area dead weight tester. The gage could be read to a ± 0.07 bar accuracy. This is not the accuracy at which the system pressure is known because the temperature in the loop pressurizing unit was a quasi-equilibrium situation. With careful operation and some practice, however, the pressurizing unit could be trimmed so that the system pressure could be maintained and read to within the following tolerances:

$$p = 9.45 \pm 0.14 \text{ bar}$$

$$p = 13.1 \pm 0.21 \text{ bar}$$

$$p = 20.7 \pm 0.28 \text{ bar}$$

Temperatures of the bulk fluid at the inlet and exit of the channel were obtained using calibrated, commercially purchased iron-constantan thermocouples. They were ungrounded, had a stainless steel sheath (1.59 mm OD), and a guaranteed nominal accuracy of $\pm 1.1^{\circ}C$. A calibration using an oil bath arrangement showed that the accuracy of these thermocouples could be taken as $\pm 0.6^{\circ}C$ over the temperature range encountered in this investigation.

All thermocouple outputs were connected through a selector switch and ice bath assembly to a Leeds and Northrup Model 8686 precision portable potentiometer. The reading accuracy of this instrument was taken as 0.0005 millivolts or approximately $0.1^{\circ}C$.

The flow through the test section was measured using either a standard ASME venturi meter with a 6.85 mm throat or a standard ASME 6.60 mm sharp-edged orifice. Both devices were calibrated with the usual weight tank arrangement. The following equations represent the best fit curves to the calibration data:

For Venturi: $$C_v = 0.954 \left[1 - \frac{2990}{Re_v}\right]$$

For Orifice: $$C_o = 0.605 \left[1 + \frac{423}{Re_p}\right]$$

The respective data and curves are shown in figures 7 and 8. The maximum uncertainty in the discharge coefficient in either case was taken as ± 3 percent.

The venturi or orifice pressure drop (as the case may be) was measured using a 70 inch well type mercury manometer with 0.10 inch graduations. The manometer could be read to ± 0.025 inch. During test runs, a slight oscillating of the mercury occurred which frequently negated this accuracy. In these cases, the maximum uncertainty in the mercury height was taken to be less than ± 2.5 percent.

The power to the test section heating strip was calculated from measurements of voltage and current. Voltage was measured using a direct current precision type PX-4, 1000 ohms/volt voltmeter with a rated accuracy of 0.5 percent of the full scale reading.

Measurements of the voltage drop at increments along the heating strip length were made. This data for two different heat flux values are plotted in figure 9. Results indicate the expected linear profile, i.e., uniform heat flux.

The current to the test section was determined by measuring the voltage drop across a precision shunt rated at 50 millivolts per 300 amperes, ± 1/2 percent. The readings were made using a potentiometer similar to that used in measuring the temperatures. Actually, some variation in the current of the heating strip was obtained during the tests. The maximum uncertainty in the current reading was estimated to be within ± 2.5 percent.

All photographs were obtained using a Nikon Automatic Reflex Photomic 35 mm camera with the Medical-Nikkor fixed focus master lens. Six auxiliary lens were available and could be attached singly or in pairs to the master lens. This allowed for a wide range of reproduction ratios. Best pictures were obtained with the reproduction ratios 1.5X and 2X (object fields of 0.67 x 0.98 and 0.47 x 0.71, respectively) and F-stop numbers of 45 and 32. The combination of these parameters yielded a depth of field that could be varied from approximately 0.81 mm (F = 32, 2X) to about 2.77 mm (F = 45, 1.5X). The photographs were taken on Kodak 35 mm Tri-X Pan, Fast Black and White film (ASA-400).

The photographic subjects, in this case the R-113 bubbles, were back lighted using a General Radio type 1431-A electronic Strobotac. The strobotac operated in synchronization with the camera shutter, both being triggered by a 10-second delay timer that is built into the camera. The high intensity (11 million beam candelas), short duration (3 second) flash from the strobotac was diffused by a piece of frosted glass that was located between the light source and test section.

EXPERIMENTAL PROCEDURE

The following test procedure was observed during the course of the data acquisition. First, instrumentation was set up, balanced, and the camera and flash unit mounted at the test section. The loop was then filled, pressurized to test conditions, and checked for leaks. Next, the loop pump was started and the R-113 allowed to circulate through the Sporlon filter for a minimum of fifteen minutes. This procedure was repeated prior to beginning each test day.

After the above preparations, the loop parameters were set to the particular test conditions. First the flow rate was adjusted to its approximate value and the test section pressure drop fixed to an acceptable value. Both these settings were made by throttling the main valve at the inlet of the test section and the valve on the by-pass line. Controlling the pressure drop at the test section allowed for optimum use of the coolers and heaters and prevented vapor from being generated at the suction side of the pump. The temperature of the bulk R-113 was brought to the desired value. This was accomplished by turning on the loop preheater and allowing the liquid temperature to increase in small increments. Once the desired temperature was attained, a final adjustment was made on the flow rate. The loop was now operating at a quasi-equilibrium condition that was suitable for data acquisition. The above outlined procedure took approximately three hours.

Once the system was operating at equilibrium, the thermocouples located at the inlet and exit of the test section were calibrated. This involved recording the millivolt output of each thermocouple while the test section was in the power-off condition, i.e., no power to the heating strip. This calibration was repeated both prior and immediately following a test run. Also, this procedure was repeated if during the course of the day the flow rate or fluid temperature was set to a new value.

Test runs lasted from eight to ten hours. Data was obtained (approximately) on an alternate day basis for a two-month period. During this time, the R-113 was changed three times, each time being replaced by a new or recently distilled batch.

EXPERIMENTAL RESULTS

Values of .bubble detachment data are given in Table I. The values of detachment heat flux were obtained by evaluating photographs of the flow and deciding whether there was only attached (wall) voidage or some detached voidage (bubbles in the bulk flow). The values for detachment heat flux presented in Table I were calculated by averaging the values corresponding to the last photograph with attached bubbles and the value corresponding to the first photograph with detached bubbles. Similarly, measurements of the average thickness of the bubble layer were made. This data was obtained directly from the photographs by measuring the thickness of the bubble layer on them with vernier calipers and then multiplying by the magnification factor.

Several sets of these photographs will now be discussed. Additional photographs are shown in reference 13. A complete collection of the photographs (and/or negatives) are on file. A listing is given in Table II summarizing the range of test parameters covered in the total collection of photographs.

The photographs show the flow in the test section as the pressure, mass velocity, subcooling and heat flux vary. The photographs are grouped into sets where all the variables are held constant except heat flux. Figure 10 shows a typical sequence of pictures at a pressure of 9.45 bar, a relatively low mass velocity, and medium subcooling range. The lower value of pressure and mass velocity allow fairly large bubbles to form after the bubble detachment point is reached. Figures 10(a) and (b) show attached voidage. In figure 10(c), the heat flux has increased enough so that bubbles are now present in the bulk flow. Finally, in figure 10(d), very large bubbles break off from the wall and probably continue to grow until they reach the colder fluid outside the boundary layer.

The sequence shown in figure 11 is at the same pressure and subcooling. However, the mass velocity has increased by 50 percent. Near the bubble detachment point figure 11(c) and for higher heat fluxes, figure 11(d), the bubbles have a much smaller size than those in figure 10. In figure 12, the mass velocity has been increased by a factor of 4.5 over figure 11 while the subcooling has been cut almost in half. The result is much smaller bubble size. In fact, the bubble size is becoming so small that it is difficult to interpret the photographs.

In the sequence shown in figures 13 and 14, system pressure has been increased to 13.1 bar. These photographs are similar to those taken at 9.45 bar. However, figure 14(d) shows a flow with a high heat flux. The bubble population is very high near the wall. In fact, there are dark areas shown near the surface that could be vapor patches or regions of bubbles packed very closely together.

The final two sequences, figures 15 and 16, show conditions where the system pressure is 20.7 bar. Since the critical pressure of R-113 is equal to 34.4 bar, this corresponds to a reduced pressure of 0.6. This increased pressure further reduces the bubble size. At the high mass velocities such as those shown in figure 16, the bubbles are so small and highly concentrated that they appear only as a cloud on the photograph rather than as distinct bubbles.

DISCUSSION OF RESULTS

Attention is now turned to the discussion and comparison of test data and theoretical models for predicting the bubble detachment point (the point of net vapor generation). A comparison of the data with Staub's model is given in figure 17 where the theoretical detachment parameter is plotted against the experimental value. Perfect agreement between theory and data would be indicated if all the data would fall on the 45° line. The theoretical values are calculated from equations (1) through (6) as previously described and $f(\beta)$, the contact angle function, is taken as 0.03. This value is based on pool boiling data (ref.10). The test data as indicated on the figure are not in overall agreement with the model. Agreement is seen only at the higher mass velocities for the low and moderate pressures ($p = 9.45$ and 13.1 bar) and at the low mass velocity for the 20.7 bar case.

In addition to the above data, measurements of the thickness of the bubble layer on the surface at the detachment point were made from the photographs. These data are listed in Table I. The values were obtained by averaging the bubble layer thickness measured from the photograph showing the last attached and from the photograph showing the first detached bubbles. Solving equation (1) for $f(\beta)$ and using the averaged bubble layer thickness δ_d for D_d, values of $f(\beta)$ can be calculated. These results are shown in figure 18 where $f(\beta)$ is plotted against mass velocity using pressure as a parameter. As indicated, the contact angle function is not a constant as assumed in the model but varies with mass velocity. It is worthwhile to note, however, that the calculated values of $f(\beta)$ tend to converge to that value predicted from pool boiling (0.03) at the low mass velocities. This is particularly notable with the 9.45 and 13.1 bar data. Thus, at the low mass velocities $f(\beta)$ may be taken as a constant, the pool boiling value being a reasonable first approximation. The 20.7 bar data exhibit the same trend but are somewhat removed from the other data.

This behavior of $f(\beta)$, from a physical basis, may be indicative of the relative magnitudes of the static forces that contribute to bubble detachment. These forces are buoyancy and drag. Only the drag term has an explicit dependency on the mass velocity. Thus, the constancy exhibited by $f(\beta)$ over the low mass velocities as seen from figure 18, would indicate negligible drag. Increasing the mass velocity, even slightly, significantly increases the relative contribution of the drag (because of the velocity squared dependency) and, in fact, beyond G = 250 $kg\,m^{-2}s^{-1}$, the buoyancy contribution becomes negligible; the slope of the curves approaches two.

The best agreement between the model and detachment data occurs at the high mass velocities (except at p = 20.7 bar, figure 17. However, f (β) as shown in figure 18 has a value of 0.03 (that value used in developing the theoretical model) only at the low mass velocities. Accordingly, one might expect that the detachment data and model would agree, if anywhere, at the low mass velocities. The agreement between the data at the high mass velocities (for p = 9.45 and 13.1 bar) may in part be attributable to the fact that at these conditions the actual bubble structure very nearly conforms to that assumed in the model. However, the inconsistent agreement between this theory and the data cause serious doubts on the usefulness of Staub's theory.

The comparison of the bubble detachment test data and the model of Larson and Tong is shown in figures 19, 20 and 21. The theoretical curves were obtained by writing equation (31) as,

$$q_d'' \frac{\left[\ln\left(\frac{H}{2\delta_d}\right)\right]\left(1-\alpha_b\frac{\bar{\delta}_d b}{Hw}\right)}{1-\frac{2\bar{\delta}_d}{H}} = q_d'' f(\bar{\delta}_d) = \frac{K}{P_T}\rho_f c_f \sqrt{\bar{f}/8}\, u_{fi}\Delta T_{sub} \tag{32}$$

where K and Pr_T are taken as 0.4 and 1.0 respectively, and ΔT_{sub}, $\bar{\delta}_d$, q_d'' and u_{fi} are measured quantities. The solid curves in the figures represent solutions of equation (32) at the specified subcoolings. The data points are grouped accordingly but their exact subcooling value can vary somewhat from the values specified for the theoretical curves (see the data tabulations as given in each figure). Thus, in comparing the theory and data, account should be taken of these slight differences. As is indicated in the figures, the test data points show good agreement with the model, particularly at the low and moderate pressures thus indicating that the significant independent parameters have been appropriately accounted for. Like Staub's model however, to apply Larson and Tong's equation requires knowledge of a parameter that is not usually (nor easily) measured in heat transfer experiments. In this case its the bubble layer thickness, δ.

In view of the complicated and differing bubble layer structures observed from the photographs, it is not surprising that Staub's model, a model that is more or less based on a "microscopic" description of the bubble layer, yields inconsistent results. The photographs show that the bubble layer structure varies considerably with the different operating parameters, i.e., mass velocity, subcooling, etc. Such differences imply differing orders of magnitude in the governing forces. On the other hand, the model of Larson and Tong ignores the details of the bubble layer structure and deals principally with the heat transfer across the layer. The model is basically insensitive to changes in the structure of the bubble layer, as long as the thickness of the layer is known. The success of the model in predicting the data suggests that the heat transfer could be the controlling process in the dynamics of bubble detachment. Such an observation is not entirely unfounded. Zuber (ref. 14) in an earlier work has studied the growth and collapse of vapor bubbles in subcooled liquids. He reports that the heat transfer across the bubble interface can, in certain instances, control the growth rate of the bubble. The resultant dynamic forces can conceivably be comparable in magnitude to the surface tension and the hydrodynamic drag forces.

A comparison of the data is made in figure 22 with a correlation first suggested by Bowring (ref. 5), where the subcooling parameter at bubble detachment is plotted against the inlet subcooling. The solid curve represents the form of Bowring's equation, where the product of θ_d and u_{fi} is taken to be $0.22\,^{o}\mathrm{C}\ \mathrm{m}^3\ \mathrm{kJ}^{-1}$ the average value. Actually, the product of the subcooling parameter θ_d (in $\mathrm{m}^2\ {}^{o}\mathrm{K}\ \mathrm{kW}^{-1}$) and inlet fluid velocity (in meter per second) is not a constant (for a given pressure) as was originally suggested by Bowring. This is shown very clearly in figure 23 for the present test data. The product of subcooling parameter and velocity is seen to increase as the velocity increases.

Another interesting discovery was made regarding the point of net vapor generation and its relative location on a boiling curve (plot of heat flux versus wall superheat). Boiling curves were constructed for R-113 in reference 13 as part of the bubble inception studies. The correlation of Panian (ref. 15) was used for the fully-developed boiling region. The fully-developed boiling region is that part of the boiling curve where the effects of bulk temperature and fluid velocity disappear. Panian's correlation for fully-developed boiling heat fluxes is:

$$q''_{fdb} = 0.0581\, p^{1.57} \left(T_w - T_s\right)^{2.86} \tag{33}$$

where q" is in $\mathrm{kW\ m^{-2}}$, pressure is in bars and temperature difference is in $^{o}\mathrm{C}$. This correlation was developed for the forced-convection boiling of R-113 from a stainless-steel surface between pressures of 10.0 to 17.5 bar. From the point of bubble inception toward increasing superheats, the boiling curve was approximated by the correlation of Bergles and Rohsenow (ref. 16). This correlation merges asymptotically into equation (33) at high heat fluxes. Their approximation is:

$$q'' = q''_{fc} \left\{ 1.0 + \left[\frac{q''_{fdb}}{q''_{fc}} \left(1 - \frac{q''_{bi}}{q''_{fdb}} \right) \right]^2 \right\}^{1/2} \tag{34}$$

This correlation involves a weighting of various heat flux values. At a given wall superheat, the fully-developed boiling heat flux, q''_{fbd}, the heat flux due to forced convection if there were no boiling, q''_{fc}; and the heat flux for fully-developed boiling at the bubble inception superheat are combined according to equation (34).

Some boiling curves obtained by this procedure are shown in figures 24, 25, and 26. Also shown on these figures are the bubble detachment data of Table I. As can be seen, these values lie quite close to the fully-developed boiling line given by equation (33), but slightly to the left. These results suggest that a quantitative relationship might be established that relates the wall heat flux at bubble detachment to corresponding values at fully-developed boiling and a subcooling parameter, S such that,

$$q''_d = S\, q''_{fdb} \tag{35}$$

To investigate the applicability of such a correlation, values of (q''_d/q''_{fbd}) were determined from the test data for the various flow rates and subcooling conditions. This involved determining the wall superheat for each data point using equation (34) and calculating the corresponding q''_{fbd} value using equation (33). The forced convection correlation used was that determined in reference (13) for this specific geometry of a heated strip in one wall of a rectangular channel. The single-phase, turbulent forced-convection equation is:

$$Nu = 0.0578\, Re^{0.762}\, Pr^{0.4} \left(\frac{\mu_L}{\mu_w}\right)^{0.14} \tag{36}$$

The heat flux ratios or S defined in equation (35) as determined for the experimental data are shown plotted against a dimensionless subcooling parameter $(c_f \Delta T_{sub}/h_{fg})$ in figure 27. The solid curve drawn through the data points has the following equation.

$$S = 1 + 0.417 \left(c_f \Delta T_{sub}/h_{fg}\right)^{-1.432} \tag{37}$$

This equation was determined by the method of least squares and fits the data within ± 15 percent. The effect of pressure on S seems to be adequately treated by using the dimensionless subcooling relationship $c_f \Delta T_{sub}/h_{fg}$.

The effect of increasing subcooling is to shift the bubble detachment point closer to the onset of fully-developed boiling. It is unclear from the present data as to what value the heat flux ratio approaches when subcooling nears zero. Therefore, equation (37) is not expected to apply at very low subcoolings. However, near zero subcooling, it is not unreasonable to expect that q''_d

would approach q''_{incp}, i.e.,

$$S = \frac{q''_{incp}}{q''_{li}} \quad as \quad \Delta T_{sub} \to 0. \tag{38}$$

Data in this region are needed.

Equation (35) provides a relatively simple means of determining bubble detachment from boiling curve information. For a given subcooling and pressure, the product $S \cdot q''_{fdb}$ defines a line that falls parallel to the fully-developed boiling line as shown in figure 28. This line represents the locus of points for bubble detachment for the given pressure, and subcooling, ΔT_{sub}. Then, for a given mass velocity, G, bubble detachment corresponds to the point of intersection of the $S \cdot q''_{fdb}$ line and the local boiling curve which is defined by this particular value of G, as schematically illustrated in figure 28.

Combining the Larson and Tong analysis, equation (31) with the above correlation, equation (37) yields a convenient means of obtaining a solution for the bubble boundary layer thickness at detachment, $\bar{\delta}_d$, the remaining variable. Two such solutions are shown in figure 39 along with the corresponding experimental data. In obtaining solutions, it was assumed that $(2/H)\,\bar{\delta}_d$ and $\alpha_b\left(\frac{\bar{\delta}_d b}{H w}\right)$ are much less than 1.0. Comparison of the data and model shows at least fair agreement. It should be noted however that $\bar{\delta}_d$ appears in equation (31) as a logarithmic function and therefore even a small discrepancy in the exponent can make a significant difference in the $\bar{\delta}_d$ calculations. Conversely, this means that the product

$$\left[\frac{K}{P_T} \rho_f c_f \sqrt{\bar{f}/8}\; u_{fi} \; \frac{\Delta T_{sub}}{q''_d} \right] \tag{39}$$

is relatively insensitive to changes in $\bar{\delta}_d$. Thus, equation (31) could be used to approximate (q''_d) if some average value of $\bar{\delta}_d$ is assumed.

To correlate the bubble layer thickness data obtained in this study, a regression analysis was performed to determine the best least squares fit of the equation

$$\bar{\delta}_d = C \,(\Delta T_{sub})^{a} (G)^{b} (p)^{c} \tag{40}$$

where $\bar{\delta}_d$ is in mm, ΔT_{sub} in $^{\circ}C$, G in kg $m^{-2}s^{-1}$ and p in bars. The independent variables were chosen to correspond to the major system parameters. Results give for the correlation,

$$\bar{\delta}_d = 9.87 (\Delta T_{sub})^{0.068} (G)^{-0.464} (p)^{-0.354} \tag{41}$$

The test data and correlation are shown in figure 30. It is interesting to note that according to equation (41) the dependence of $\bar{\delta}_d$ on subcooling is to the positive exponent. Thus, increasing subcooling means that the bubble layer tends to get larger before the bubbles depart. This would imply higher void volumes (at departure) at the higher subcoolings. At the same time, it should be noted, however, that the dependence of $\bar{\delta}_d$ on the magnitude of ΔT_{sub} is relatively small (as indicated by the small exponent). Thus for even fairly large changes in subcooling, the change in $\bar{\delta}_d$ is very minimal.

Jiji and Clark (ref. 17) have made measurements of the bubble boundary layer thickness in the subcooled boiling of water. They correlate their data by the equation,

$$\bar{\delta} = C (\Delta T_{sub})^{-1.163} (G)^{-0.504} (q'')^{1.256} (\Delta L)^{0.534} \tag{42}$$

where C is a constant and ΔL the distance from the point of initial inception of boiling to the point in question. Evaluating equation (42) at the bubble detachment point gives

$$\bar{\delta}_d = C (\Delta T_{sub})^{-1.163} (G)^{-0.504} (q''_d)^{1.256} (\Delta L)^{0.534} \tag{43}$$

Approximating q''_d from equation (31) as

$$q''_d \cong C_1 \sqrt{\bar{f}/8}\, G\, \Delta T_{sub}$$

and substituting into equation (43) gives,

$$\bar{\delta}_d = C_2 (\bar{f})^{0.628} (G)^{0.752} (\Delta L)^{0.534} (\Delta T_{sub})^{0.093} \tag{44}$$

Comparing equations (44) and (41) it is interesting to note that the two equations approximately agree in the exponent on the subcooling term (in both sign and magnitude). The mass velocity terms, however, do not correlate. Part of this difference can be attributed to the $\bar{f}$ term since $\bar{f}$ is a function of throughput. The effect of pressure is not clearly shown in equation (44) but Jiji and Clark indicate that the bubble boundary layer thickness is not affected by changes in pressure in a simple manner. Increasing pressure from a low (14 bar) to moderate value (34 bar), they observed the bubble layer to increase; but in going from the moderate to high pressure (55 par), the thickness of the layer decreased and, in fact, decreased below that value measured at

14 bar. A similar behavior is noted in the data obtained in this study.

CONCLUSIONS

In this report, theoretical predictions of bubble detachment were compared with experimental data for the forced convection boiling of refrigerant-113 at pressures from 9.45 to 20.7 bar. Bubble detachment was determined by photographing the flow in the test section and determining the conditions for which detached bubbles first appeared in the bulk flow. These results were compared with existing theories which lead to the following conclusions.

1. Staub's microscopic model based on static and dynamic forces did not give consistent agreement with the data. In particular, the best agreement with the data was found under conditions where some of the theoretical assumptions used in the model were known to be false.

2. The Larson and Tong model based on a macroscopic energy balance yielded results that were within ± 25 percent of the data. This agreement is within the experimental uncertainty expected in the data. This theory required a minimum number of assumptions.

3. A correlation was found between the bubble detachment point and boiling curve. It was found that the location of the bubble detachment point on the boiling curve was only a function of the dimensionless subcooling. The correlation does not apply to very low subcoolings and additional data is needed in this region.

4. The bubble boundary layer thickness at bubble detachment, δ_d, was measured and found to depend primarily on mass velocity and only slightly on subcooling. The subcooling dependency was shown to agree with prior water studies by Jiji and Clark. A correlation of the present data with major system parameters was obtained which agreed with the data within ± 30 percent.

APPENDIX A

ERROR ANALYSIS

The data from any experiment can only be interpreted within the limits of the accuracy and reliability of the measurements. These limits are difficult and often impossible to ascertain in single sample experiments. Nevertheless, it is necessary for the experimenter to attempt to describe the uncertainties in the data in order to add credence to the results. Such an analysis would first be extremely helpful in selecting the apparatus best suited for the experiment, and secondly, give the experimenter a basis for evaluating his data.

An analysis has been conducted to describe the uncertainties in the data reported herein. The calculations are based on the equations presented by Kline and McClintock (ref. 18), who show that the uncertainty interval W_r in some function R of n independent variables V_i is given by

$$W_r = \left[\left(\frac{\partial R}{\partial V_1} W_1\right)^2 + \left(\frac{\partial R}{\partial V_2} W_2\right)^2 + \ldots + \left(\frac{\partial R}{\partial V_n} W_n\right)^2\right]^{1/2} \qquad (A.1)$$

where W_i is the uncertainty interval in the variable V_i. In developing the above equation, it was assumed that the same odds exist for each of the variable intervals and for the result, i.e., if the confidence intervals of the W_i variables are 90 percent, then the confidence interval on W_r will also be 90 percent. Using this equation, the uncertainty in the variables can be estimated. The basic measured quantities and their respective uncertainty intervals are summarized in Table A.1. The confidence intervals in the variables were arbitrarily set at 90 percent.

The calculations for the error in the derived quantities are summarized below.

(A) For the mass velocity G, the equation is written

$$G = KC\sqrt{Z} ,$$

where K is a constant dependent on the geometry of the metering device and the fluid properties, $K = K\ (\rho, D_h, D_1, D_2)$, C is the coefficient of discharge, and Z the mercury displacement in the

TABLE A.1

	Quantity	Symbol and Unit	Quantity Value and Confidence Interval (max.)
1.	Pressure	P (bar)	9.45 ± 0.14 bar
2.	Mercury displacement	Z (inch)	1.0 ± 0.05 inch
3.	Temperature difference	ΔT (°C)	25 ± 5°F
4.	Temperature	T (°F) V (volts)	100 ± 2°F
5.	Voltage	V (volts) A (amps)	10 ± 0.25 volts
6.	Current	A (amps)	50 ± 1.25 amps
7.	Length of heated strip	l (mm)	526 ± 6.3 mm
8.	Width of heated strip	b (mm)	3.18 ± 0.08 mm
9.	Channel width	w (mm)	12.70 ± 0.25 mm
10.	Channel height	a (mm)	9.50 ± 0.25 mm

manometer. Using Eq. (A.1), the uncertainty in G is written

$$\frac{W_G}{G} = \left[\left(\frac{W_K}{K}\right)^2 + \left(\frac{W_C}{C}\right)^2 + \left(\frac{1}{2}\ \frac{W_Z}{Z}\right)^2\right]^{1/2} \qquad (A.2)$$

K and C are not basic measured variables and their respective uncertainty interval must be derived. The uncertainty in the discharge coefficient C was determined from calibration data to be ± 3 percent, while the uncertainty in K was calculated by examining the functional relationship $K = K(\rho, D_h, D_1, D_2)$. The uncertainty in ρ, the fluid density and D_1 and D_2 the inlet and throat diameters of the venturi (or orifice) were taken to be small, compared to the uncertainty in D_h, the hydraulic diameter:

$$D_h = 2\frac{(a).(w)}{(a + w)} \quad .$$

The uncertainty in D_h using the values for the uncertainties in a and w from Table A.1 is (after applying Eq. (A.1)),

$$\frac{W_{D_h}}{D_h} = \pm \quad 0.04 \ ,$$

Thus, substituting the values for the uncertainties of K, C, and Z into Eq. (A.2) yeilds the uncertainty in the mass velocity,

$$\frac{W_G}{G} = \pm \quad 0.055 \quad .$$

This represents the maximum error. At the higher mass velocities this error is expected to reduce to around 5 percent, because the error in the manometer mercury displacement W_Z becomes small with increasing Z.

(B) For the heat flux, q", which is determined from voltage, amperage and geometry measurements, the equation is written:

$$q = \text{Constant} \quad . \quad \frac{V \ . \ A}{b \ . \ l},$$

where V is the voltage, A the amperage, and b and l are the width and length of the heating strip, respectively. The equation describing the uncertainty in q" is:

$$\frac{W_{q''}}{q''} = \left[\left(\frac{W_V}{V}\right)^2 + \left(\frac{W_A}{A}\right)^2 + \left(\frac{W_b}{b}\right)^2 + \left(\frac{W_l}{l}\right)^2\right]^{1/2} \qquad \text{(A.3)}$$

Substituting for the uncertainty intervals of the basic measured quantities from Table A.1 into Eq. (A.3) yields:

$$\frac{W_{q''}}{q''} = \pm \ 0.036 \ .$$

The uncertainty in b and l are fixed. Data indicates that the uncertainty in V and A remains approximately constant. Thus, the uncertainty $W_{q''}$ is reasonably insensitive to change in q".

(c) The error in ΔT_{sub} is the composite error in T_s and T_b. The local bulk temperature T_b at some given point in the channel was calculated from measurements of the inlet temperature and an energy balance, while the saturation temperature, T_s, was determined from the system pressure measurement and saturation tables.

The local bulk temperature could be calculated from

$$T_b = T_{in} + \frac{x}{L} (T_{out} - T_{in}) \qquad (A.4)$$

The increase in the channel bulk temperature, as represented by the last term in the above equation, was always small compared to T_{in} (less than 10 percent). Thus, even a substantial error in the last term would not be significantly reflected in the sum. The error in determining the local bulk temperature T_b was therefore assumed to be that error associated with the bulk inlet temperature, T_{in}, i.e., $\pm 0.6^{o}C$. To find the uncertainty in the saturation temperatures, it was first necessary to determine the error in the measurements of the system pressure. Results are tabulated below.

$p = 9.45 \pm 0.14$ bar ; $T_s = 136 \pm 1.7^{o}C$

$p = 13.1 \pm 0.21$ bar ; $T_s = 154 \pm 1.7^{o}C$

$p = 20.7 \pm 0.28$ bar ; $T_s = 180 \pm 1.7^{o}C$

The error in the temperature difference ΔT_{sub} was calculated using Eq. (A.1). The bulk temperature was a basic test parameter and was varied in the different test runs. Thus, a minimum, medium, and maximum uncertainty was calculated,

$$\Delta T_{sub} = 97 \pm 1.8^{o}C \ ; \ \frac{W_{\Delta T_{sub}}}{\Delta T_{sub}} = \pm\ 0.019 \text{ minimum,}$$

$$\Delta T_{sub} = 60 \pm 1.8^{o}C \ ; \ \frac{W_{\Delta T_{sub}}}{\Delta T_{sub}} = \pm\ 0.030 \text{ medium,}$$

$$\Delta T_{sub} = 25 \pm 1.8^{o}C \ ; \ \frac{W_{\Delta T_{sub}}}{\Delta T_{sub}} = \pm\ 0.072 \text{ maximum.}$$

(D) For the Nusselt number defined as

$$Nu = \frac{hd_e}{k}$$

where h is the heat transfer coefficient, d_e the hydraulic diameter, and k the thermal conductivity The uncertainty in Nu is given by:

$$\frac{W_{Nu}}{Nu} = \left[\left(\frac{W_h}{h}\right)^2 + \left(\frac{W_k}{k}\right)^2 + \left(\frac{W_{D_h}}{D_h}\right)^2 \right]^{1/2} \qquad (A.5)$$

The heat transfer coefficient h is obtained from:

$$h = \frac{q''}{(T_w - T_b)} \quad .$$

The uncertainty in heat flux q", hydraulic diameter D_h, and the local bulk temperature T_b have been discussed above. The measurement of the wall temperature is discussed in ref. 13. The overall uncertainty in T_w, is a combination of the calibration error (± 2 percent) and that due to heat loss (also about 2 percent). Thus,

$$\frac{W_{\Delta T_{w-b}}}{\Delta T_{w-b}} = \pm \; 0.04 \quad .$$

The uncertainty in the thermal conductivity, k, has been reported to be of the order of ± 20 percent (ref. 1). The uncertainty in the Nusselt number is therefore from eq. (A.5).

$$\frac{W_{Nu}}{Nu} = 0.21.$$

(E) For the Reynolds number defined as

$$Re = \frac{Gd_e}{\mu}$$

the uncertainty is given by:

$$\frac{w_{Re}}{R_e} = \left[\left(\frac{w_G}{G}\right)^2 + \left(\frac{w_{D_h}}{D_h}\right)^2 + \left(\frac{w_\mu}{\mu}\right)^2\right]^{1/2} \qquad (A.6)$$

The error in mass velocity, G, and hydraulic diameter, d_e, have been discussed. The uncertainty in the viscosity was taken as ± 10 percent. The uncertainty in the Reynolds number becomes

$$\frac{w_{Re}}{Re} = \pm\ 0.12\ .$$

This again represents the maximum error in the Reynolds number. When the mass velocity is increased (increasing Re), the uncertainty in the Reynolds number will decrease because the error in z decreases.

(F) For the Prandtl number,

$$Pr = \frac{\mu c_p}{k}$$

the uncertainty is

$$\frac{w_{Pr}}{Pr} = \pm\ 0.17$$

which represents only the contributions of the viscosity and thermal conductivity. The uncertainty in the specific heat, c_p, is ignored.

The above calculations represent an attempt to estimate the uncertainty in the measured and derived test quantities. The results should be considered only in a qualitative sense, since the actual errors of many of the variables are complicated functions of the variables themselves. The values reported above are the expected maximum uncertainties, and thus, most of the data should fall within these values.

APPENDIX B

SYMBOLS

b	width of heating strip, m
c	specific heat, J kg^{-1} K^{-1}
C	discharge coefficient, dimensionless
D	diameter, m
e	surface roughness, m
f	friction factor, dimensionless
$f(B)$	contact angle function, dimensionless
F	force on bubble, N
g	acceleration, m s^{-2}
G	mass velocity, kg m^{-2} s^{-1}
h	specific enthalpy, J kg^{-1}
h_{fg}	latent heat of vaporization, J kg^{-1}
H	height of channel, m
K	constant, dimensionless
m''	mass flux, kg m^{-2} s^{-1}
P	perimeter, m
Pr	Prandtl number of liquid, dimensionless
Pr_T	turbulent Prandtl number, dimensionless
q''	heat flux, W m^{-2}
Re	Reynolds number based on equivalent diameter, dimensionless
S	subcooling parameter, s dimensionless
T	temperature, K
u	axial velocity, m s^{-1}
w	channel width, m
x	distance from unheated wall, m
y	distance from heated wall, m
Y^+	characteristic distance, dimensionless
z	distance along channel, m

GREEK:

α	void fraction, dimensionless
α_H	thermal diffusivity, $m^2\ s^{-1}$
β	contact angle, dimensionless
δ	bubble layer thickness, m
Δ	difference
ϵ	eddy diffusivity, $m^2\ s^{-1}$
η	empirical parameter
θ	subcooling parameter, $m^2\ {}^{o}K\ kW^{-1}$
μ	viscosity of liquid, $kg\ m^{-1}\ s^{-1}$
ν	kinematic viscosity, $m^2\ s^{-1}$
ρ	density, $kg\ m^{-3}$
σ	surface tension, $N\ m^{-1}$
τ	shear stress, $N\ m^{-2}$

SUBSCRIPTS:

b	bulk or bubble
B	bouyancy
bi	bubble inception
cl	core liquid
d	detachment
D	drag
f	liquid
fc	forced convection
fdb	fully-developed boiling
fg	change from liquid to vapor
fi	fluid inlet
g	vapor
max	maximum
s	saturation
st	surface tension

REFERENCES

1. Bergles, A.E.; Bakhru, N.; and Shires, J.W.: Cooling of High-Power-Density Computer Components. Research Report No. 60, Dept. Mech. Eng., M.I.T., Nov. 1968.

2. Griffith, P.; Clark, J.A.; and Rohsenow, W.M.: Void Volumes in Subcooled Boiling Systems. ASME Paper No. 58-HT-19, 1958.

3. Levy, S.: Forced-Convection Subcooled Boiling - Prediction of Vapor Volume Fraction. Int. J. of Heat and Mass Transfer, vol. 10, 1967, pp. 951-965.

4. Larson, P.S.; and Tong, L.S.: Void Fractions in Subcooled Flow Boiling. J. of Heat Transfer, vol. 91, no. 4, November, 1969, pp. 471-476.

5. Bowring, R.W.: Physical Model Based on Bubble Detachment and Calculation of Steam Voidage in the Subcooled Region of a Heated Channel. OECD Halden Reactor Project Report, HPR-10, 1962.

6. Marchaterre, J.F.; Petrick, M.; Lottes, P.A.; Weatherhead, R.J.; and Flinn, W.S.: Natural and Forced Convection Boiling Studies. ANL-5735, May, 1960.

7. Zuber, N.; Staub, F.W.; and Bijward, G.: Vapor Void Fraction in Subcooled Boiling and Saturated Boiling Systems. Proc. of the Third International Heat Transfer Conf., Chicago, Ill., vol. 5, 1966, pp. 24-38.

8. Thom, J.R.S.; Walker, W.; Fallon, T.A.; and Reising, G.F.S.: Boiling in Subcooled Water During Flow Up Heated Tubes or Annuli. Proc. Inst. Mech. Engr., vol. 180, 1965-66, pp. 226-246.

9. Rouhani, Zia S.: Calculation of Steam Volume Fraction in Subcooled Boiling. J. of Heat Transfer, vol. 90, 1969, pp. 158-164.

10. Staub, F.W.: The Void Fraction in Subcooled Boiling - Prediction of the Initial Point of Net Vapor Generation. J. of Heat Transfer, vol. 90, 1968, pp. 151-157.

11. Fritz, W.: Maximum Volume of Vapor Bubbles. Phys. Z., vol. 36, 1935, pp. 379-384.

12. Schlichting, H.: Boundary Layer Theory. 4th ed., McGraw-Hill, 1955, pp. 487-489.

13. Lippert, T.E.: Experimental Determination of the Heat-Transfer and Vapor-Void Characteristics of R-113 in Subcooled Flow at Boiling Inception and at the Point of Net Vapor Generation. Ph.D. Thesis, Mech. Eng. Dept., Univ. of Pittsburgh, 1971.

14. Zuber, N.: The Dynamics of Vapor Bubbles in Nonuniform Temperature Fields. Int. J. of Heat and Mass Transfer, vol. 2, 1961, pp. 83-98.

15. Panian, D.J.: Subcooled Forced Convection Boiling of R-113 (FREON). M.S. Thesis, Mech. Eng. Dept., University of Pittsburgh, 1970.

16. Bergles, A.E.; and Rohsenow, W.M.: The Determination of Forced-Convection Surface-Boiling Heat Transfer. J. of Heat Transfer, vol. 86, 1964, pp. 365-372.

17. Jiji, L.M.; and Clark, J.A.: Bubble Boundary Layer and Temperature Profiles for Forced Convection Boiling in Channel Flow. J. of Heat Transfer, vol. 86, 1964, pp. 50-58.

18. Kline, S.J.; and McClintock, F.A.: Describing Uncertainties in Single Sample Experiments. Mech. Eng., vol. 75, 1953, pp. 3-8.

TABLE I. - BUBBLE DETACHMENT DATA

Run Number	Pressure bar	Mass Velocity $kg\,m^{-2}s^{-1}$	Bulk Subcooling ^{o}C	Detachment Heat Flux $kW\ m^{-2}$	Detachment Bubble Layer Thickness mm
1	9.45	704	58	208	0.425
2	9.45	704	65	236	0.318
3	9.45	813	30	84.0	0.318
4	9.45	1260	30	129	0.221
5	9.45	1260	53	238	0.218
6	9.45	1630	67	358	0.180
7	9.45	1630	39	178	0.208
8	9.45	2710	34	259	0.160
9	9.45	2710	16	111	0.122
10	9.45	3930	25	250	0.104
11	9.45	5750	28	386	0.152
12	9.45	5750	19	236	0.147
13	13.1	771	44	158	0.224
14	13.1	1000	37	162	0.173
15	13.1	1360	33	139	0.112
16	13.1	1360	42	206	0.160
17	13.1	2170	28	192	0.094
18	13.1	2170	40	273	0.104
19	13.1	3050	41	349	0.097
20	13.1	3050	27	216	0.089
21	13.1	4470	18	192	0.069
22	13.1	5820	17	252	0.079
23	20.7	697	47	163	0.280
24	20.7	697	54	173	0.236
25	20.7	1180	43	246	0.170
26	20.7	1180	39	233	0.165
27	20.7	2030	30	215	0.114
28	20.7	3580	36	546	0.102
29	20.7	5410	17	352	0.157

TABLE II. - LISTING OF PHOTOGRAPHS

Film Number	Frames	Pressure bar	Mass Velocity kg m^{-2}s^{-1}	Bulk Subcooling ^{o}C	Heat Flux kW m^{-2}
F113024	1 thru 19	9.45	705	58 - 65	151 - 344
F113025	1 - 21		1110	52 - 63	154 - 340
"	22 - 36		1630	50	154 - 274
F113026	1 - 22		1260	53	53 - 240
"	23 - 36		1630	50	38 - 158
F113027	1 - 12		1630	67	183 - 347
"	13 - 24		1630	39	129 - 274
"	25 - 36		1630	23	129 - 242
F113028	1 - 18		2710	33	158 - 384
"	19 - 35		2710	16	107 - 274
F113029	1 - 20		3930	25	240 - 466
F113030	1 - 18		5760	28	271 - 469
"	19 - 36		5760	18	211 - 469
F113031	6 - 20		813	30	107 - 157
F113032	1 - 16	13.1	1260	30	69 - 183
"	17 - 20		813	30	38 - 69
F113033	1 - 16		1000	57	38 - 180
"	17 - 36		1000	43	38 - 180
F113034	1 - 19		1360	42	69 - 208
"	19 - 36		2170	40	69 - 268
F113035	1 - 26		3050	41	69 - 343
"	27 - 36		4470	39	110 - 343
F113036	1 - 17		4470	39	85 - 381
"	18 - 36		5830	36	129 - 419
F113037	1 - 18		1000	37	69 - 306
"	19 - 36		1360	33	69 - 343
F113038	1 - 18		2170	28	154 - 340
"	19 - 36		3050	27	179 - 422
F113039	1 - 20		772	43	66 - 154
"	21 - 36		4480	18	167 - 463
F113040	1 - 10		4480	18	176 - 466
"	11 - 36		5830	17	176 - 418
F113041	1 - 21	20.7	1180	39 - 47	148 - 296
"	22 - 36		2040	30 - 39	173 - 368
F113042	1 - 19		705	46 - 56	82 - 189
"	20 - 30		3600	32 - 39	227 - 482
F113043	1 - 13		3600	26	66 - 368
"	14 - 36		5420	13 - 24	255 - 491

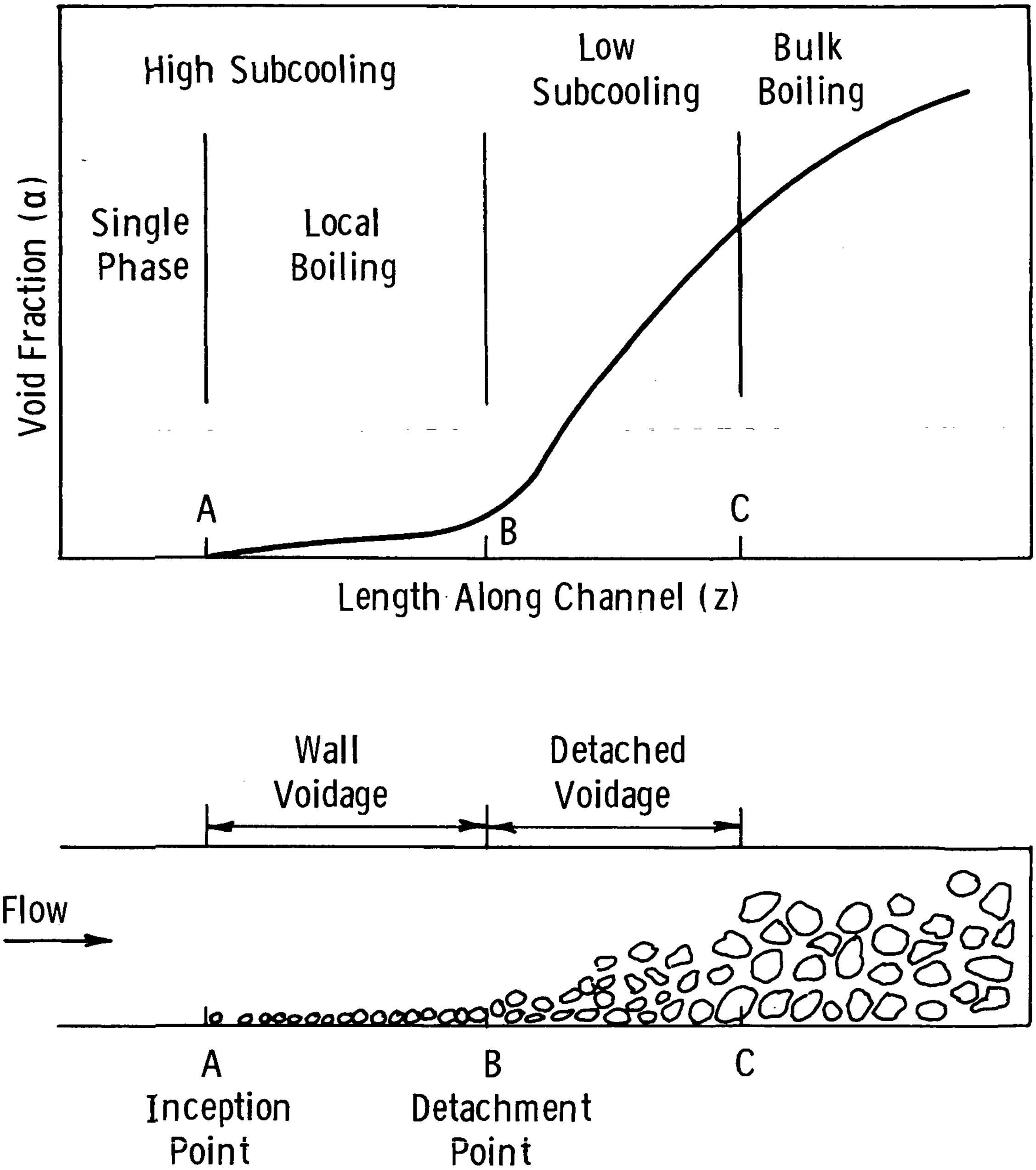

Fig. 1 —Schematic representation of void fraction and flow structure in subcooled flow boiling

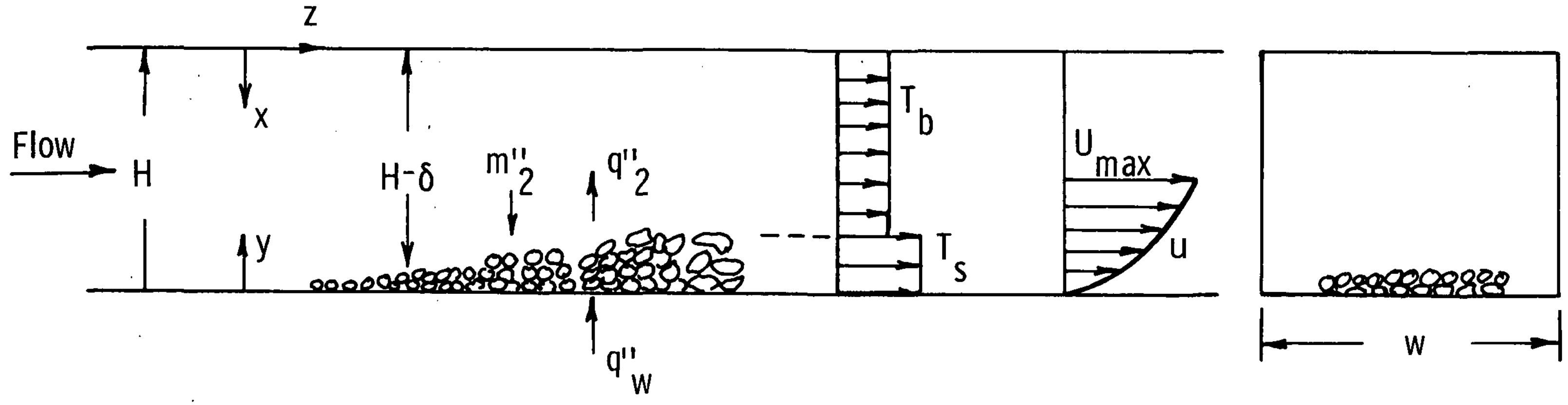

Fig. 2 —Physical geometry for the Larson Tong analysis

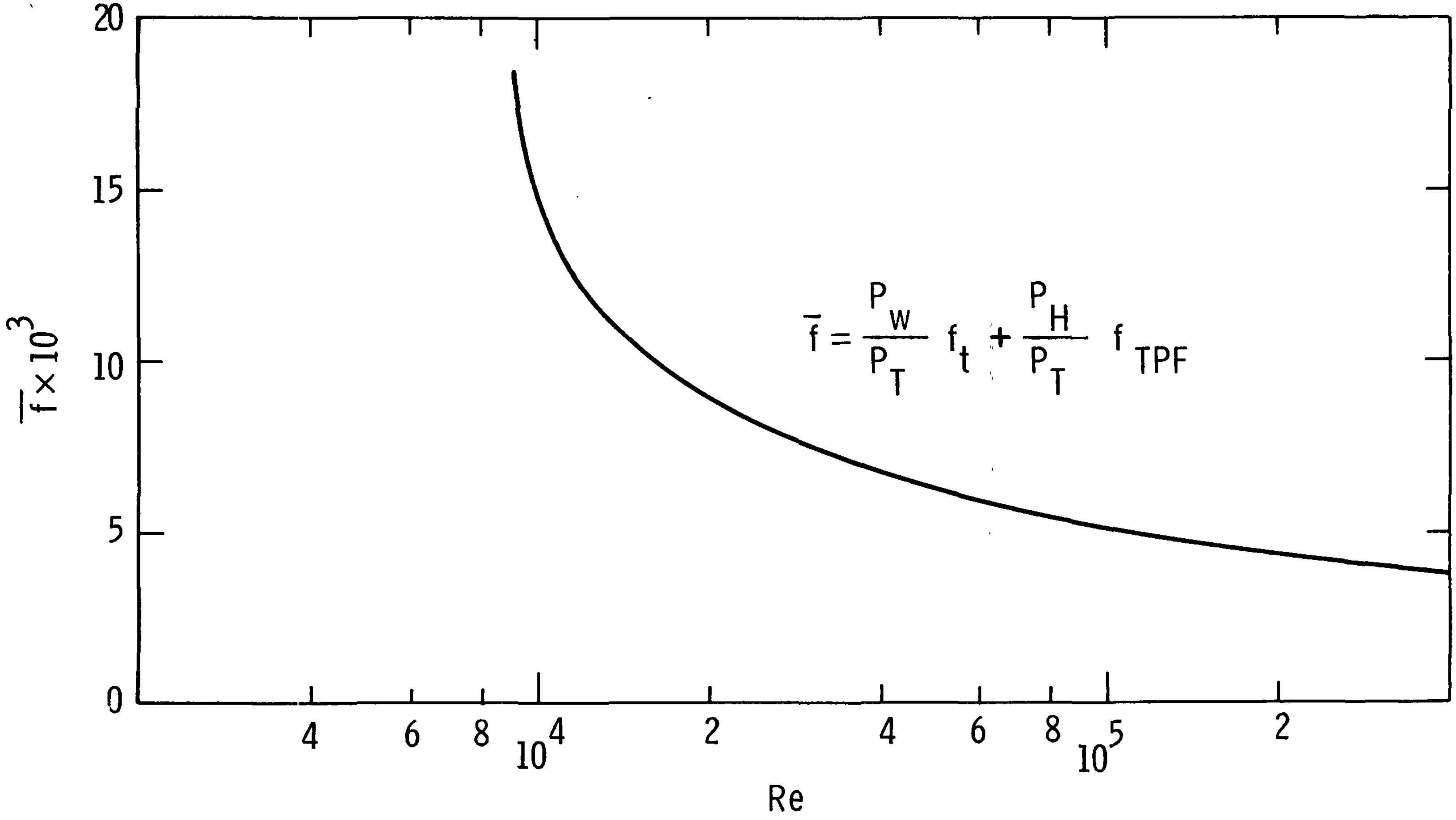

Fig. 3 —Weighted friction factor for asymmetric heating

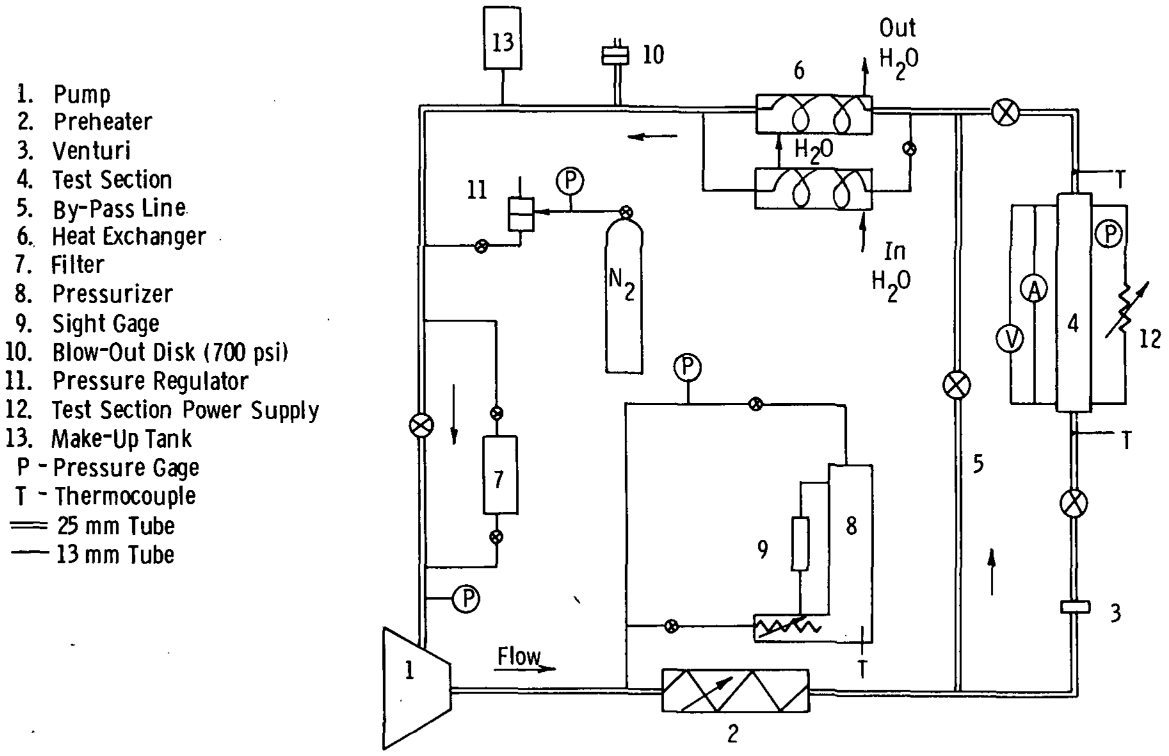

Fig. 4 —Flow loop schematic

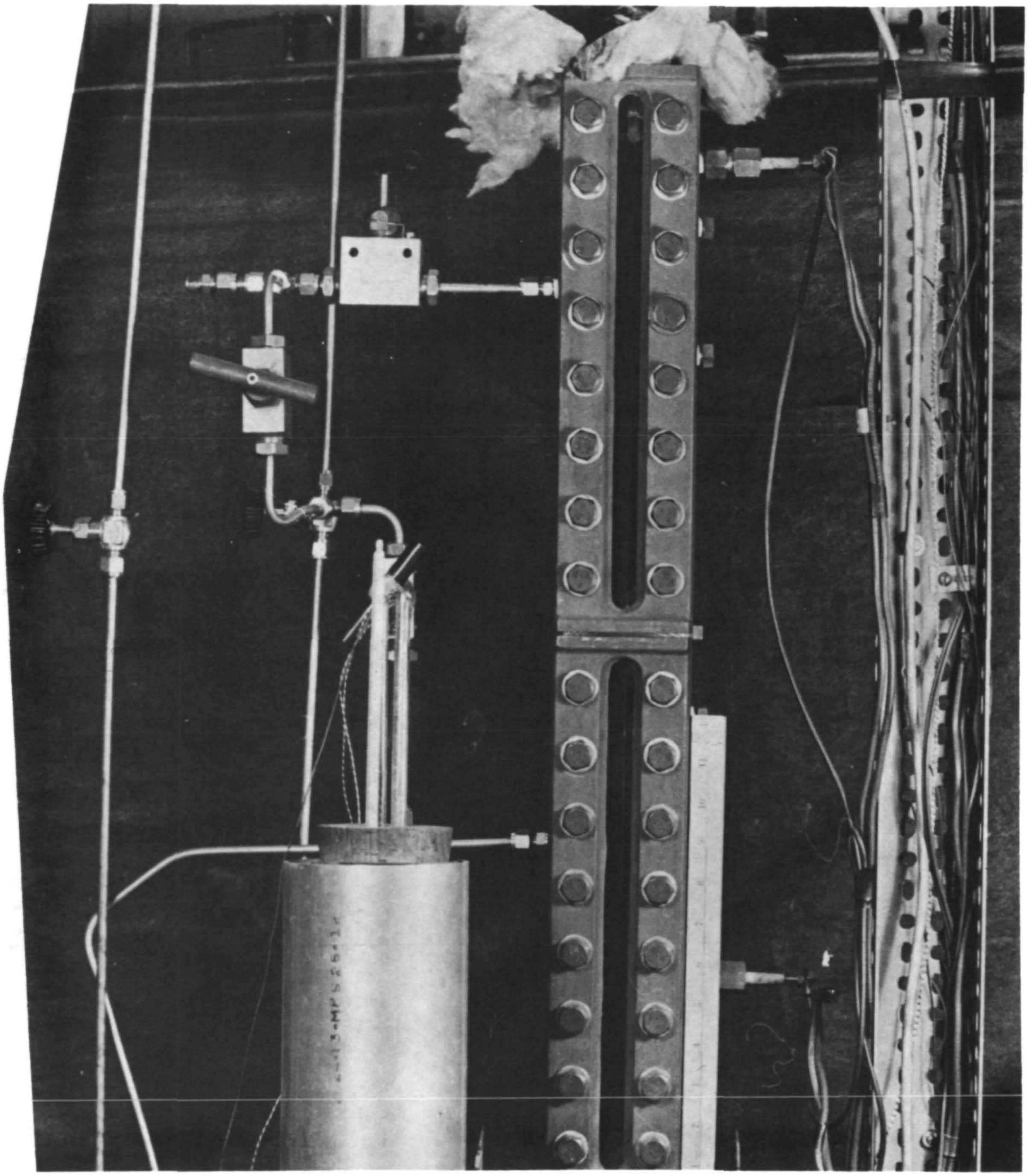

Fig. 5 Section Assembly

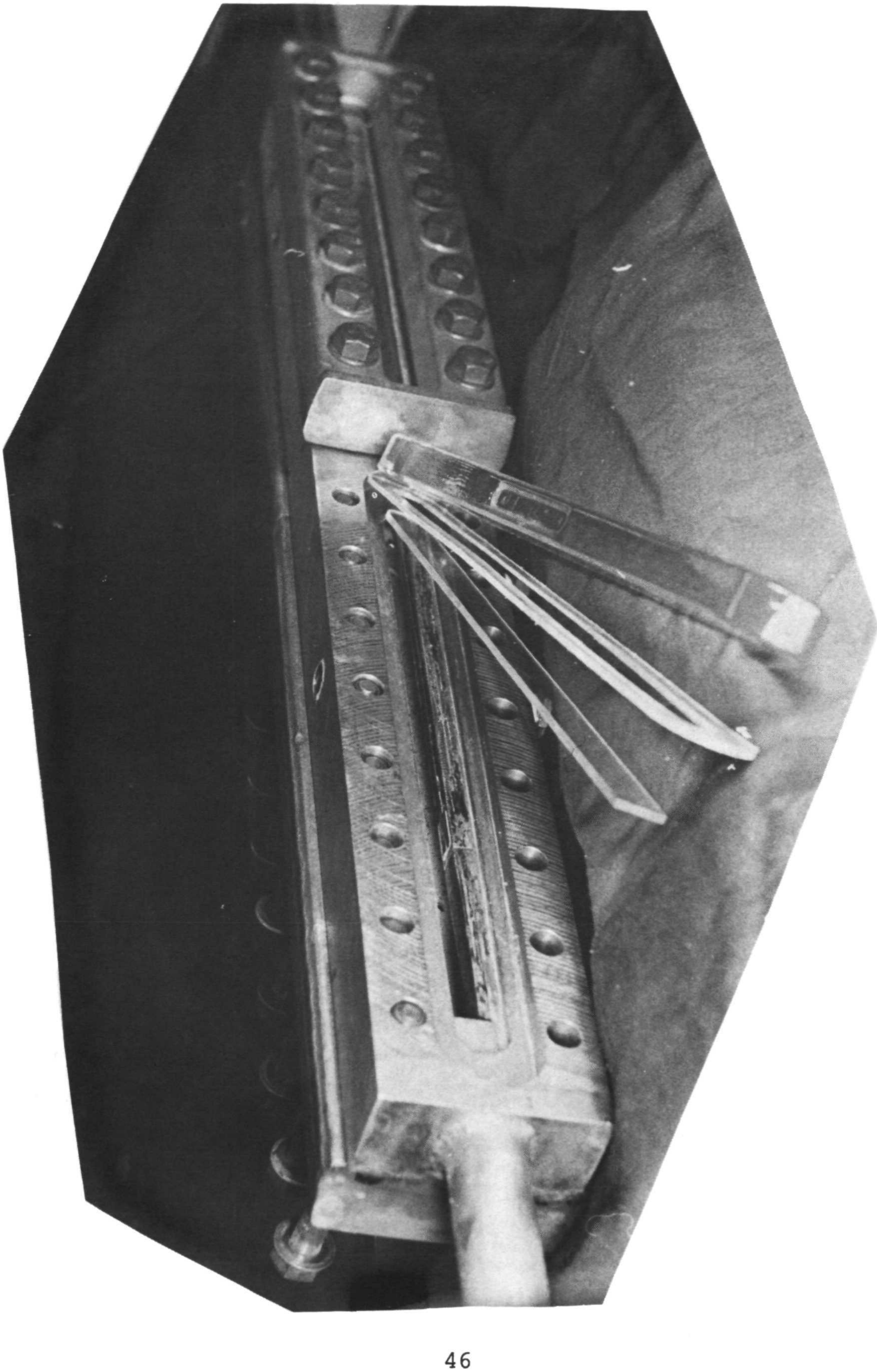

Fig. 6 Fanned View of Test Section

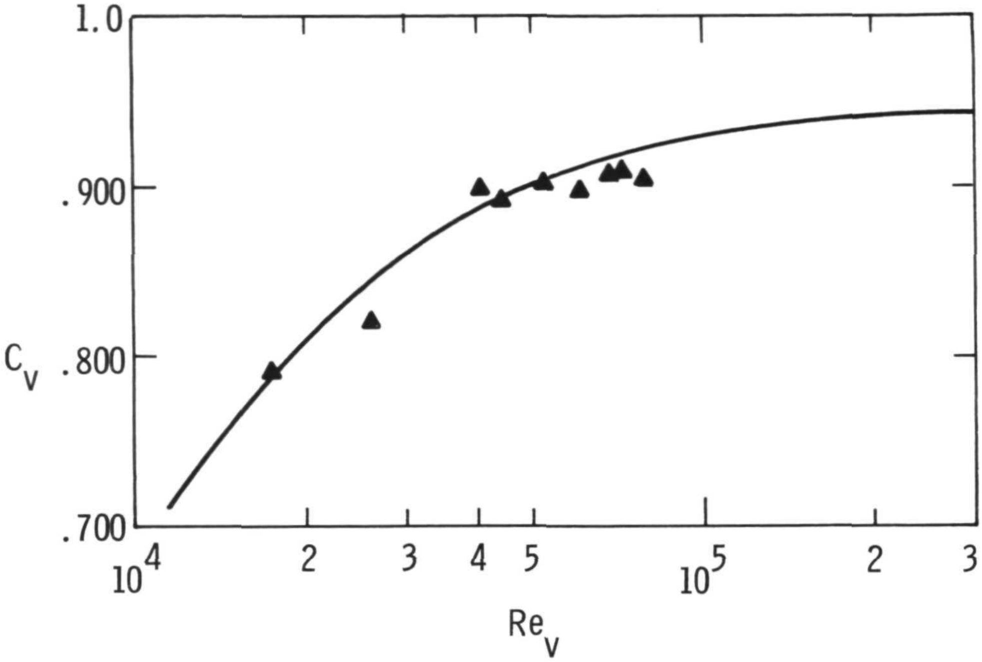

Fig. 7. - Venturi calibration.

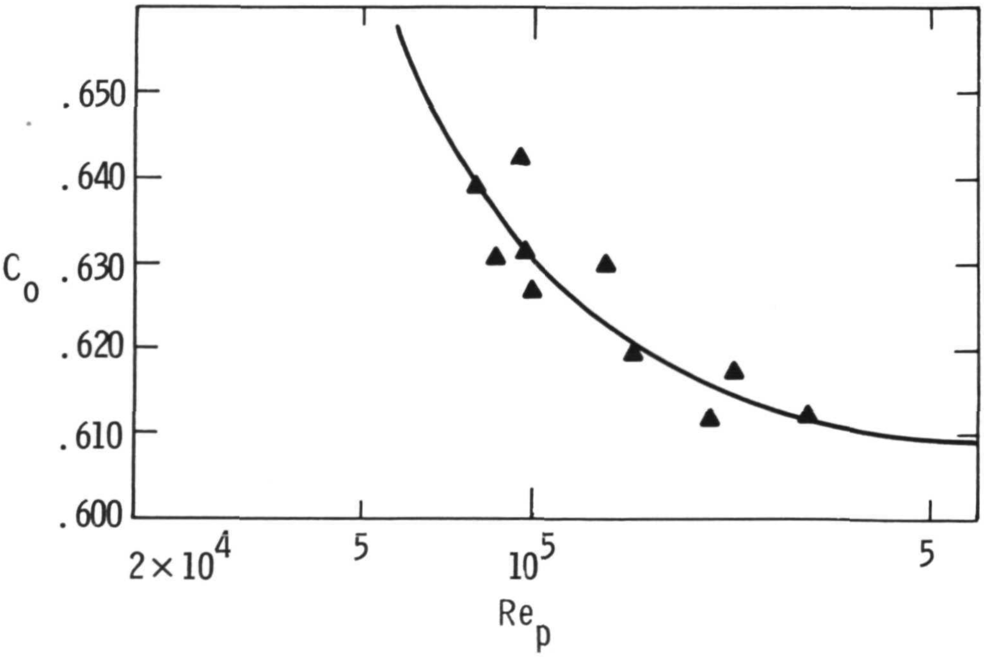

Fig. 8. - Orifice calibration.

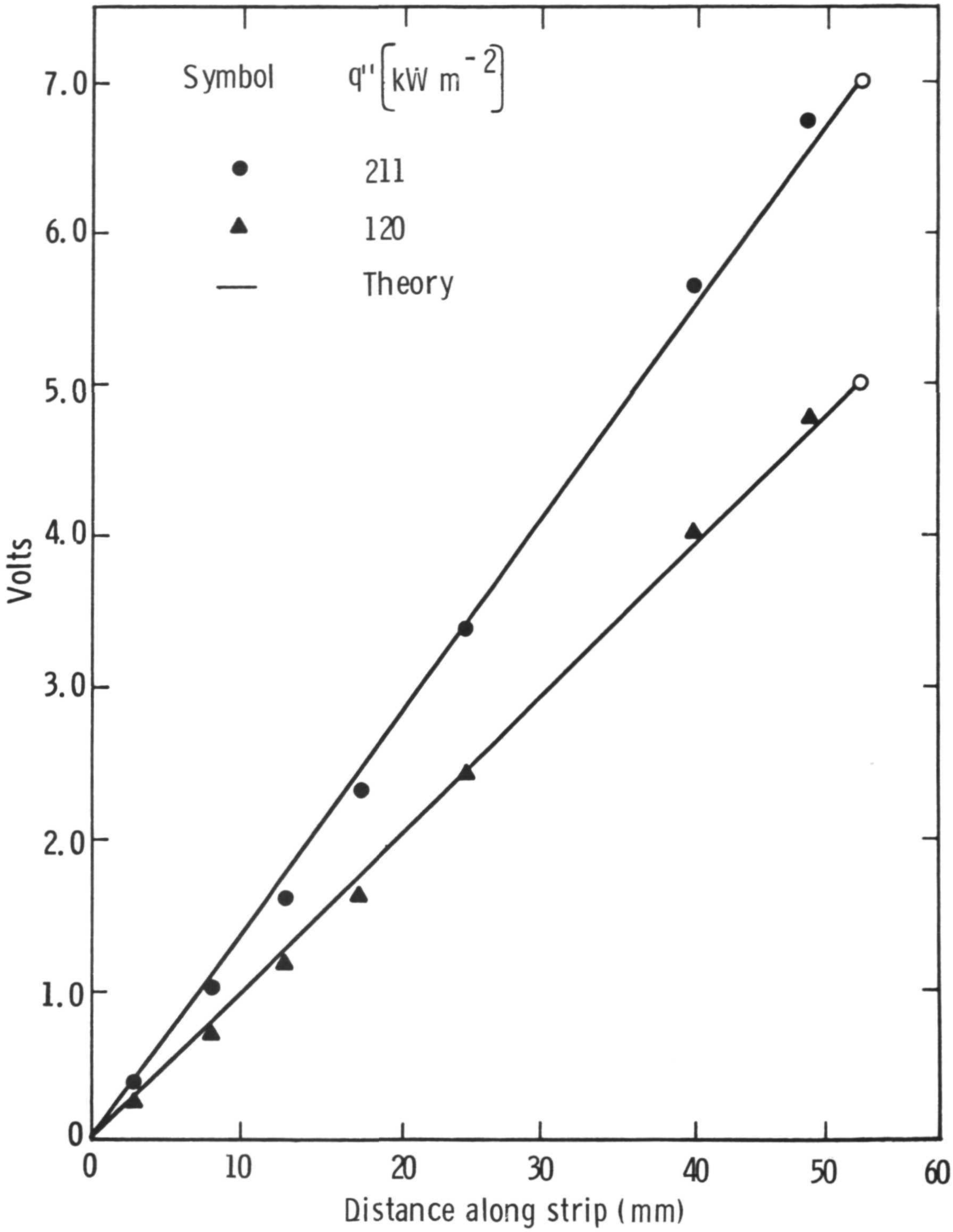

Fig. 9 — Measured voltage drop along heated strip

(a) $p = 9.45$ bar
$G = 813$ kg m^{-2} s^{-1}
$\Delta T_{sub} = 31°C$
$q'' = 53.0$ kW m^{-2}

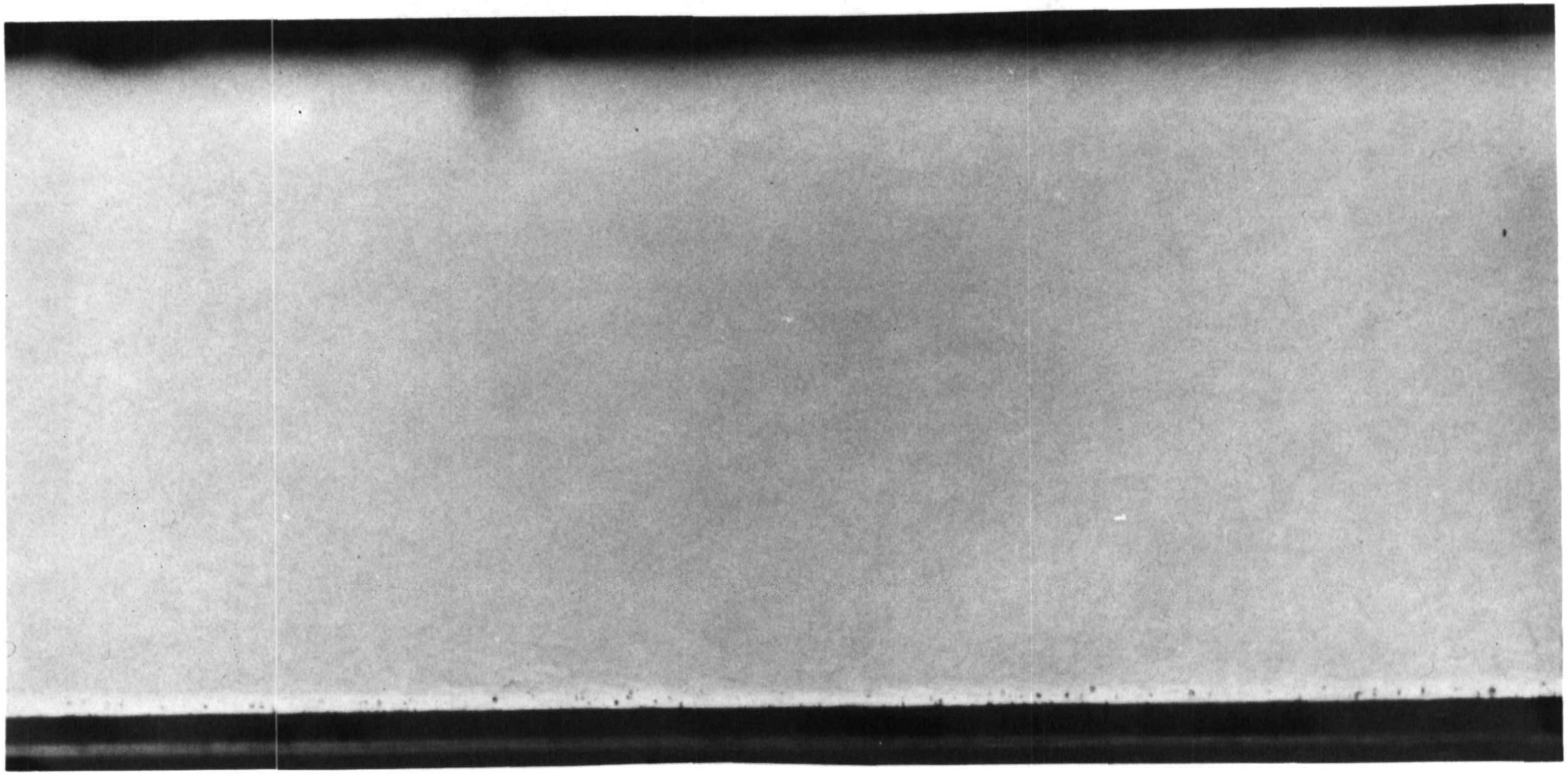

Fig. 10. - Bubbly boundary layer on heating surface.

(b) $p = 9.45$ bar
$G = 813$ kg m^{-2} s^{-1}
$\Delta T_{sub} = 30°C$
$q'' = 69.5$ kW m^{-2}

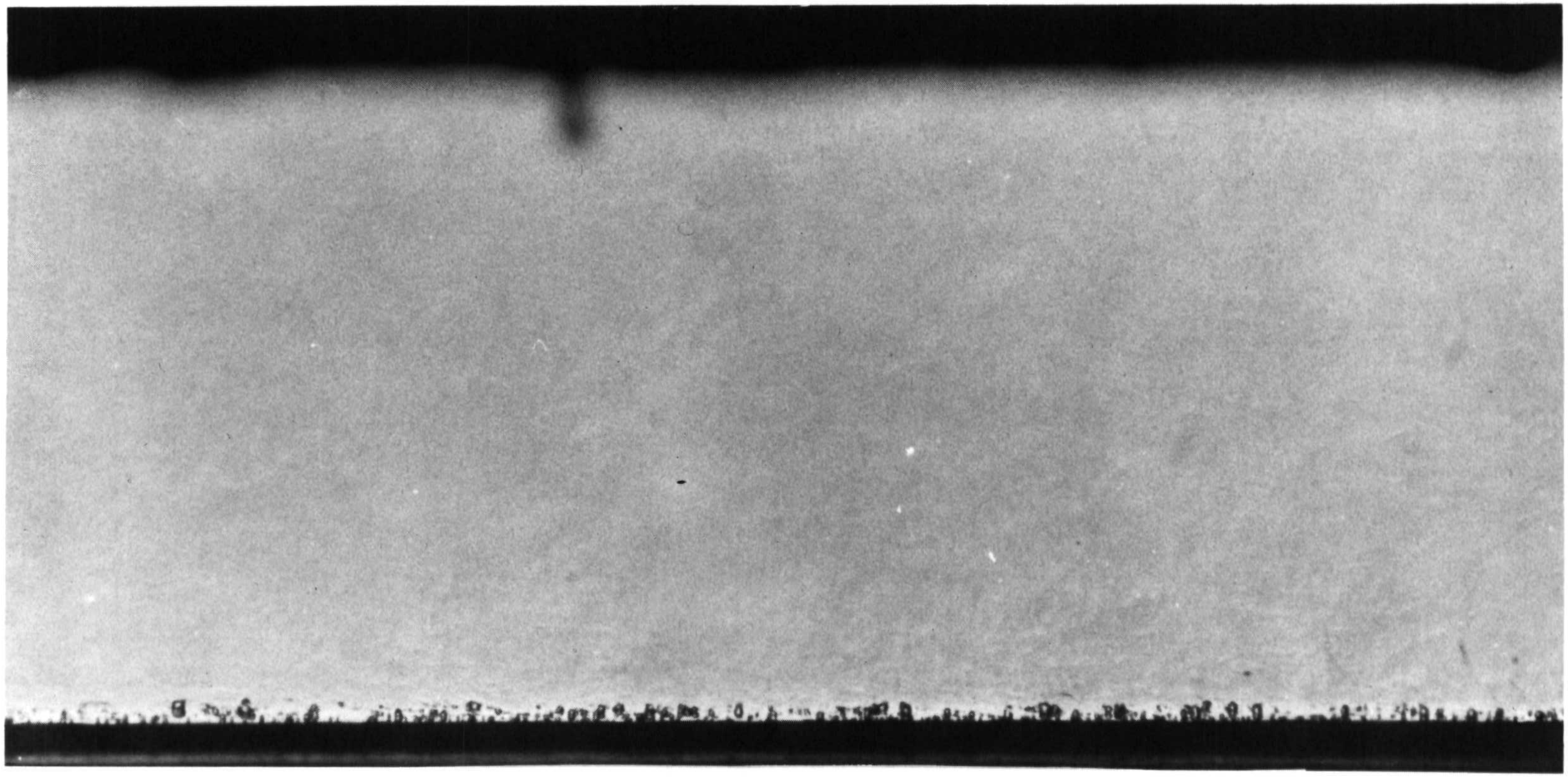

Fig. 10. - Continued.

(c) $p = 9.45$ bar
$G = 813$ kg m^{-2} s^{-1}
$\Delta T_{sub} = 30°C$
$q'' = 108.8$ kW m^{-2}

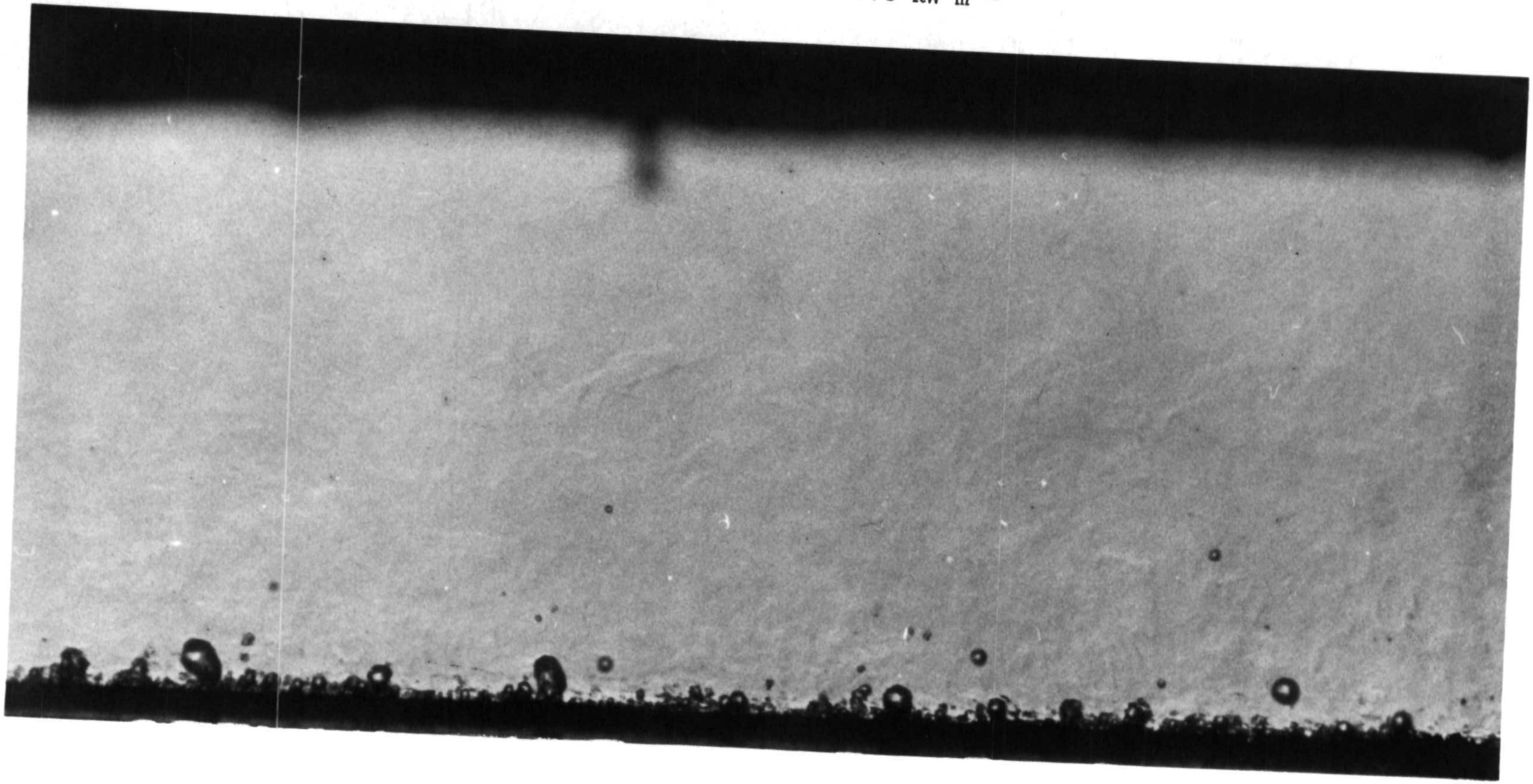

Fig. 10. - Continued.

(d) $p = 9.45$ bar
$G = 813$ kg m^{-2} s^{-1}
$\Delta T_{sub} = 30°C$
$q'' = 156.5$ kW m^{-2}

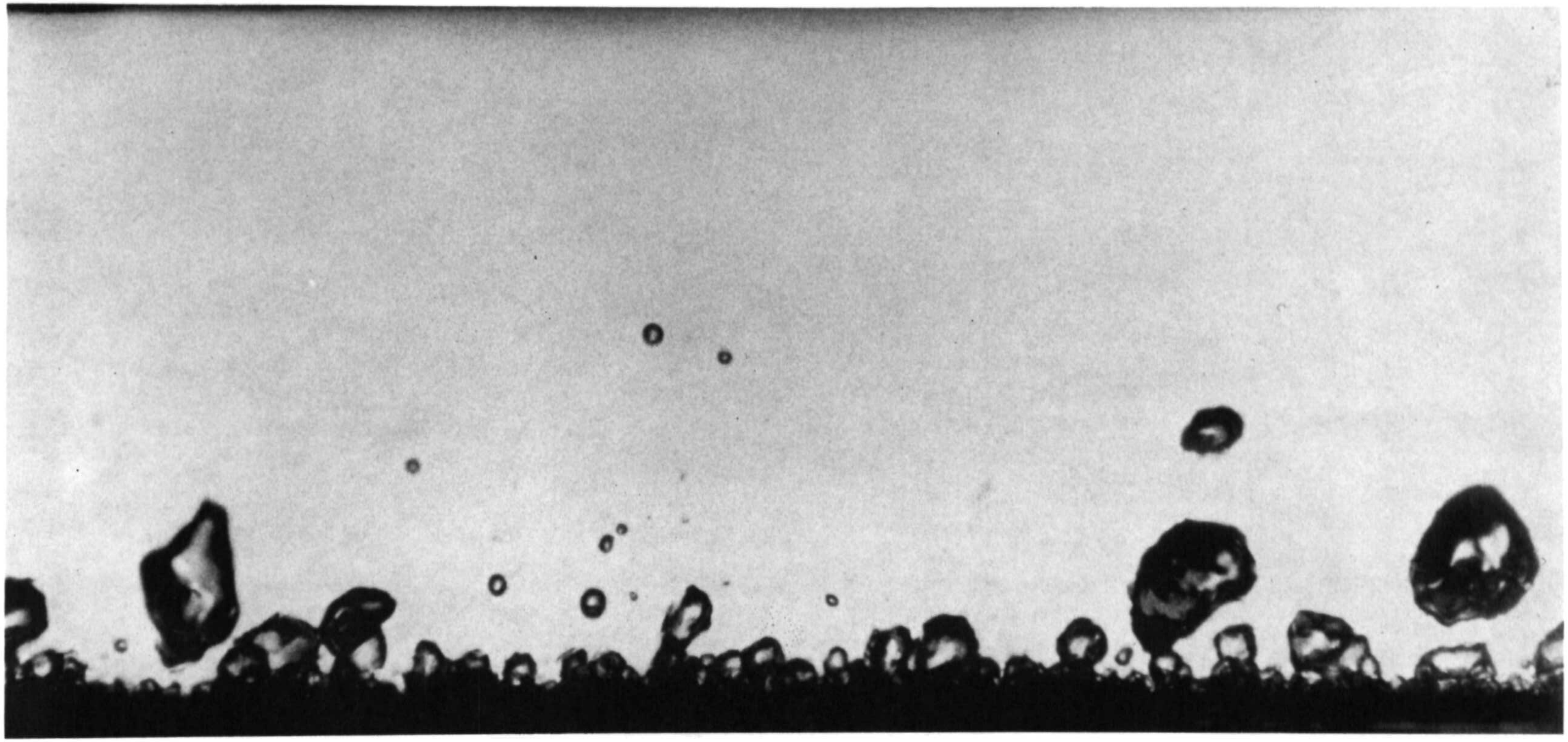

Fig. 10. - Concluded.

(a) $p = 9.45$ bar
$G = 1260$ kg m^{-2} s^{-1}
$\Delta T_{sub} = 30°C$
$q'' = 69.6$ kW m^{-2}

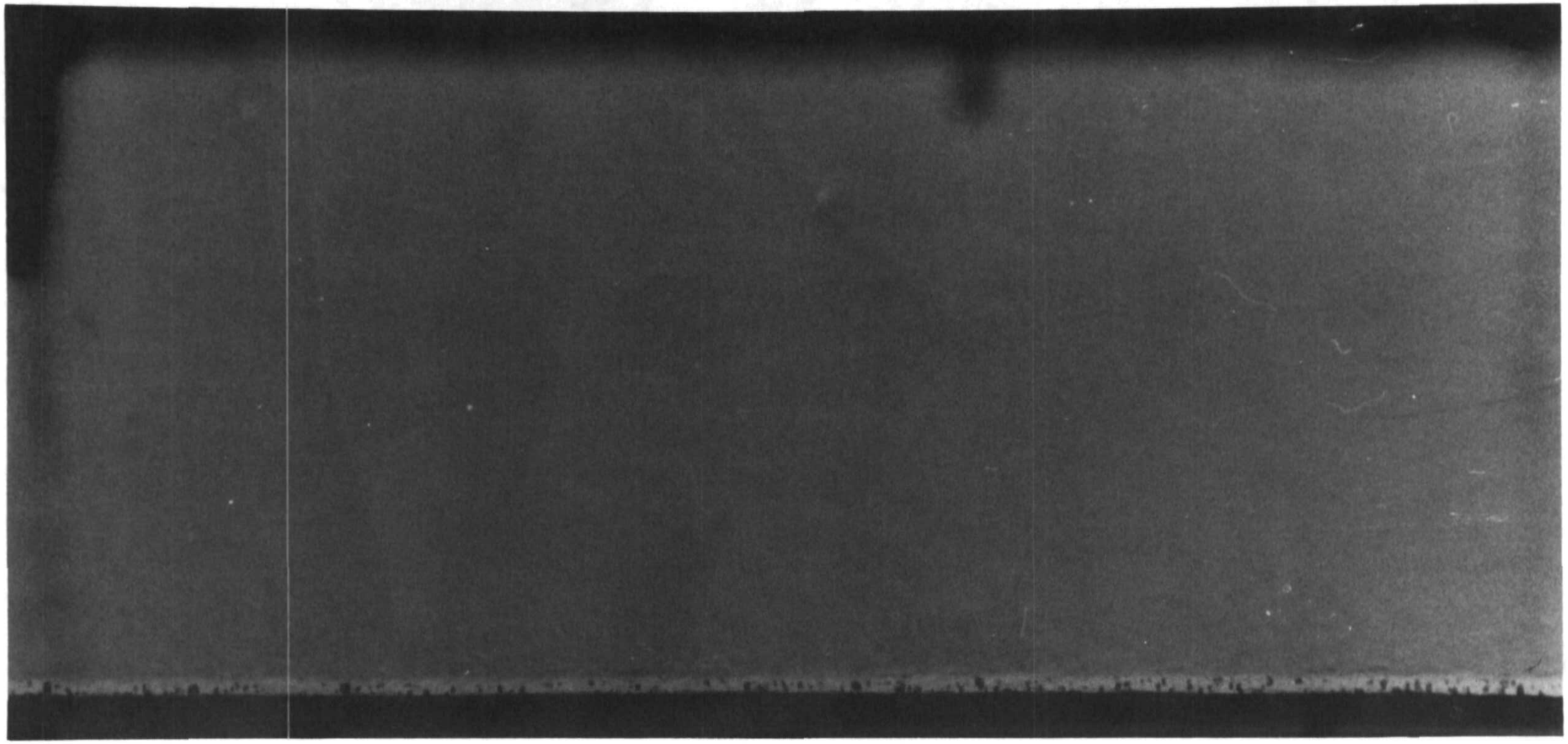

Fig. 11. - Bubbly boundary layer on heating surface.

(b) $p = 9.45$ bar
$G = 1260\ \mathrm{kg\ m^{-2}\ s^{-1}}$
$\Delta T_{sub} = 30°\mathrm{C}$
$q'' = 108.0\ \mathrm{kW\ m^{-2}}$

Fig. 11. - Continued.

(c) p = 9.45 bar
G = 1260 kg m^{-2} s^{-1}
ΔT_{sub} = 30°C
q'' = 131.0 kW m^{-2}

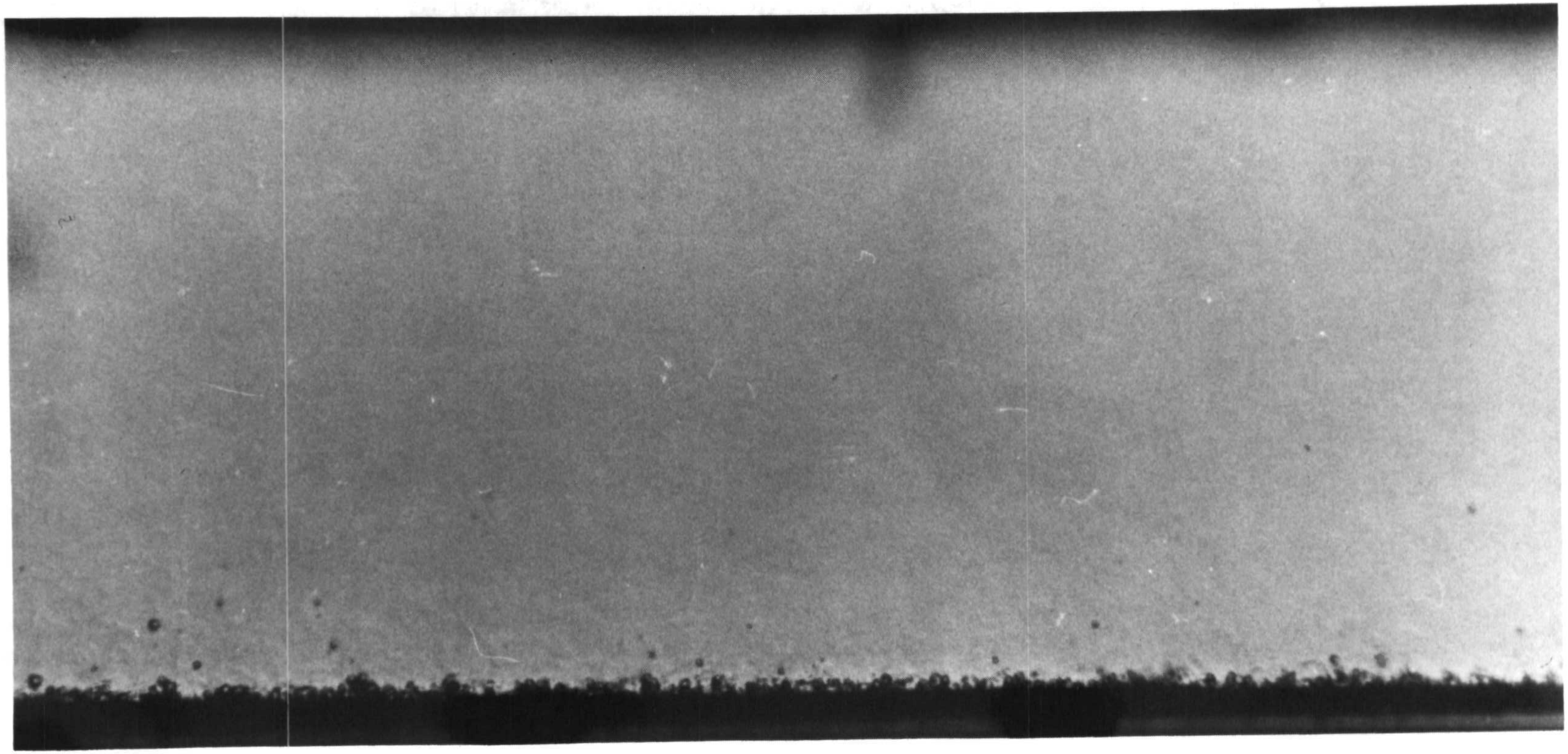

Fig. 11. - Continued.

(d) $p = 9.45$ bar
$G = 1260$ kg m^{-2} s^{-1}
$\Delta T_{sub} = 30°C$
$q'' = 156.6$ kW m^{-2}

Fig 11. - Concluded.

(a) $p = 9.45$ bar
$G = 5840$ kg m^{-2} s^{-1}
$\Delta T_{sub} = 18°C$
$q'' = 211$ kW m^{-2}

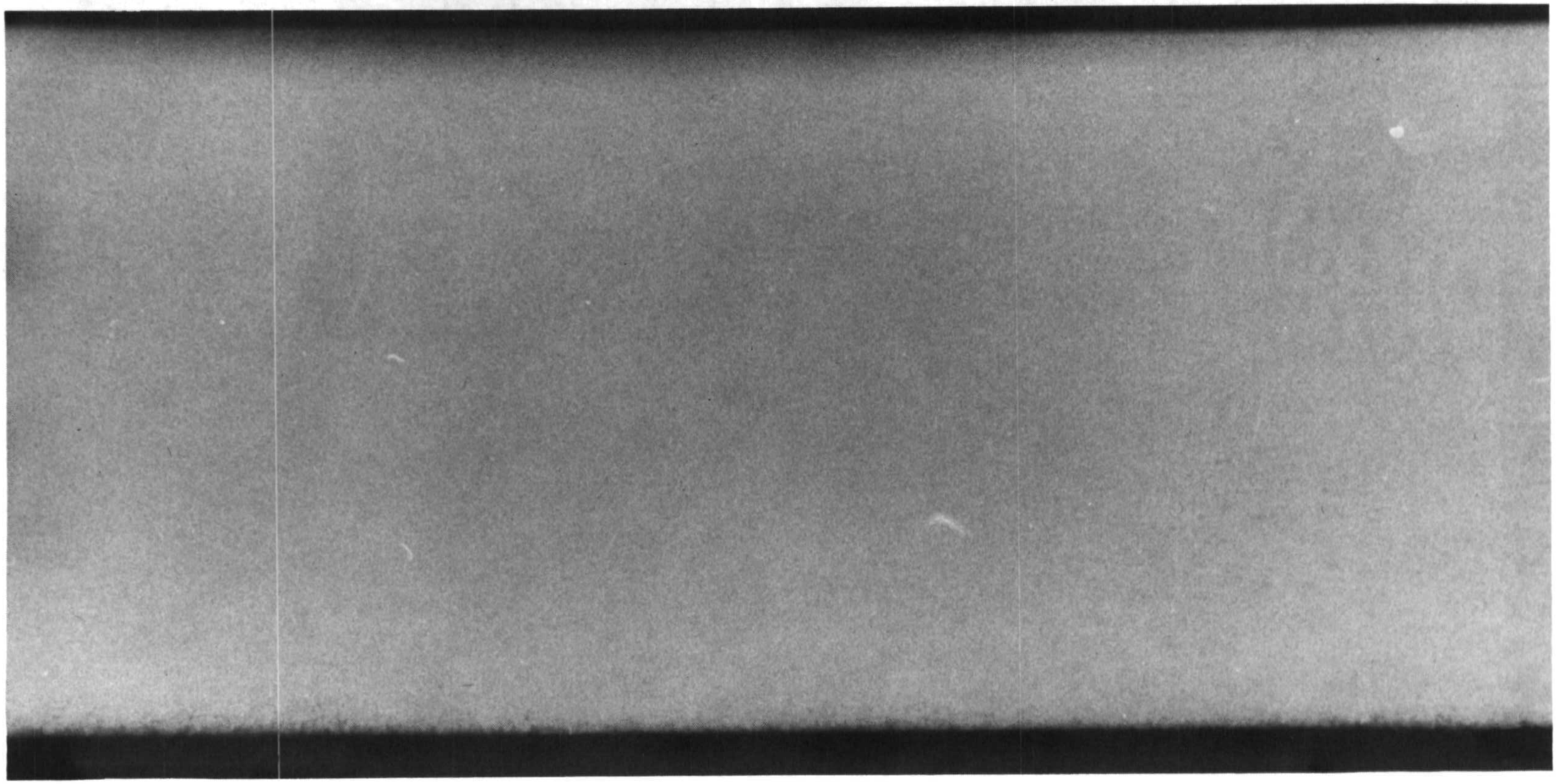

Fig. 12. - Bubbly boundary layer on heating surface.

(b) $p = 9.45$ bar
$G = 5840$ kg m^{-2} s^{-1}
$\Delta T_{sub} = 18°C$
$q'' = 239$ kW m^{-2}

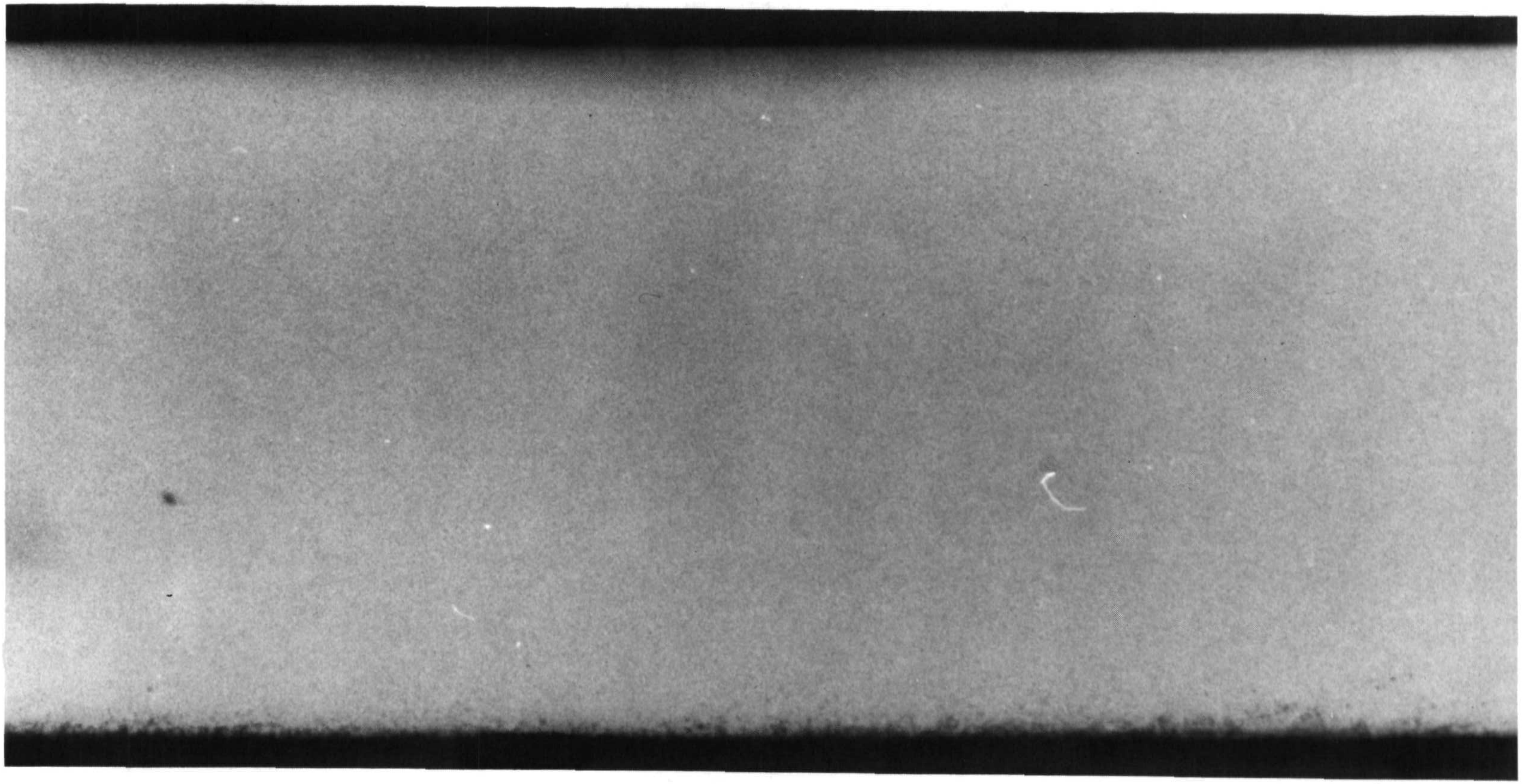

Fig. 12. - Continued.

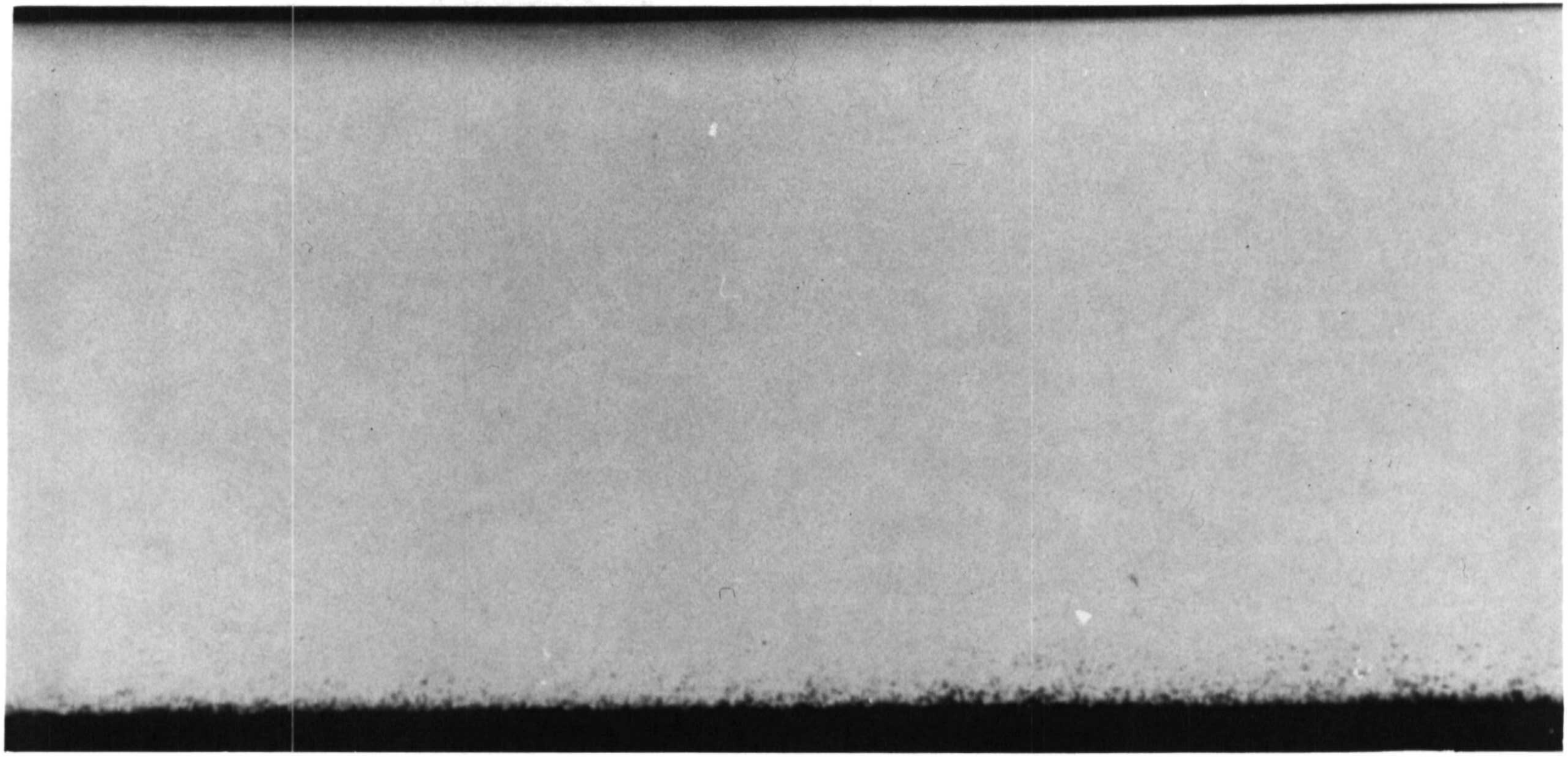

(c) p = 9.45 bar
G = 5840 kg m^{-2} s^{-1}
ΔT_{sub} = 18°C
q'' = 272 kW m^{-2}

Fig. 12. - Continued.

(d) $p = 9.45$ bar
$G = 5840$ kg m^{-2} s^{-1}
$\Delta T_{sub} = 19°C$
$q'' = 463$ kW m^{-2}

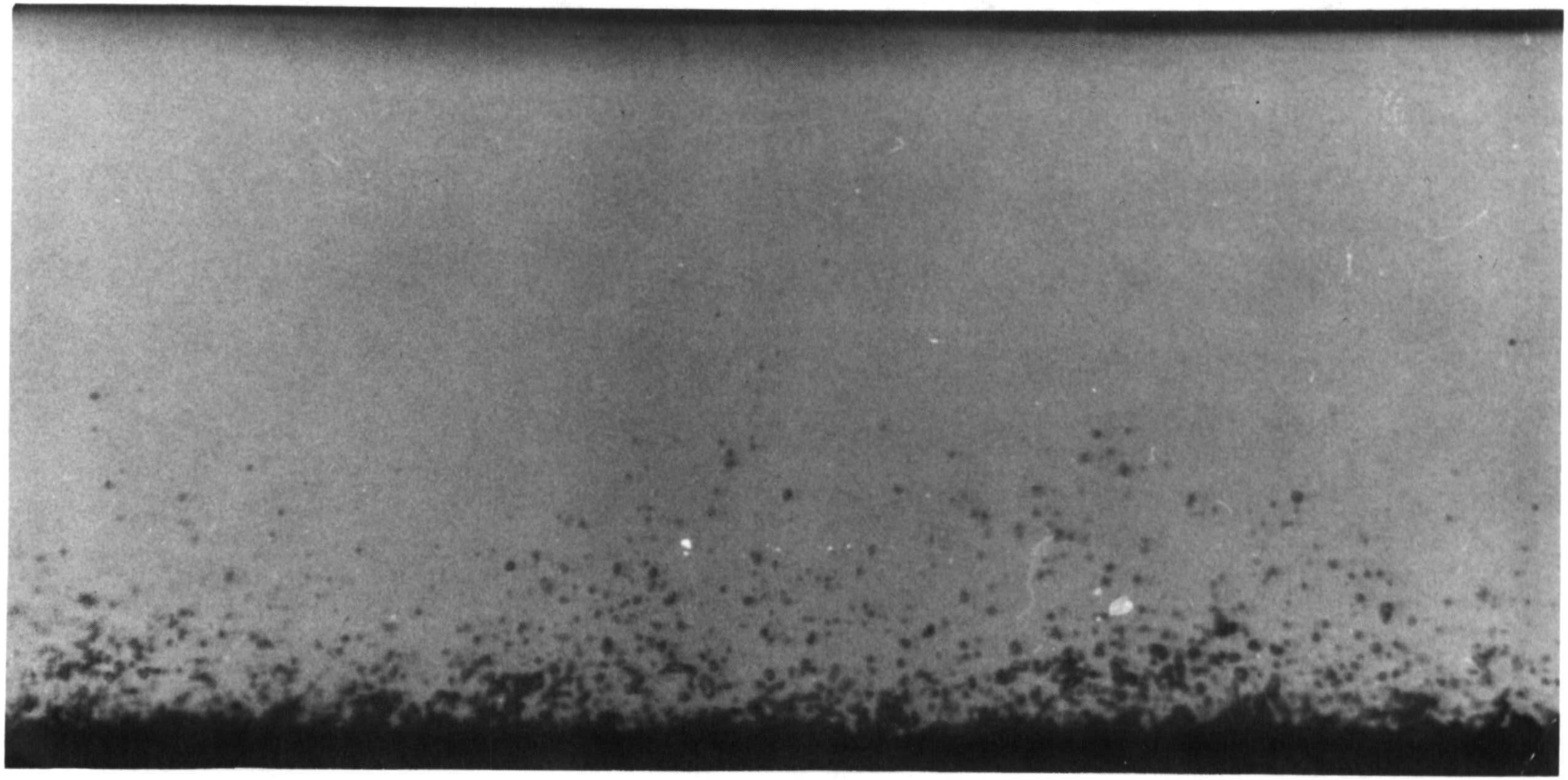

Fig. 12. - Concluded.

(a) $p = 13.1$ bar
$G = 2170$ kg m^{-2} s^{-1}
$\Delta T_{sub} = 28°C$
$q'' = 154$ kW m^{-2}

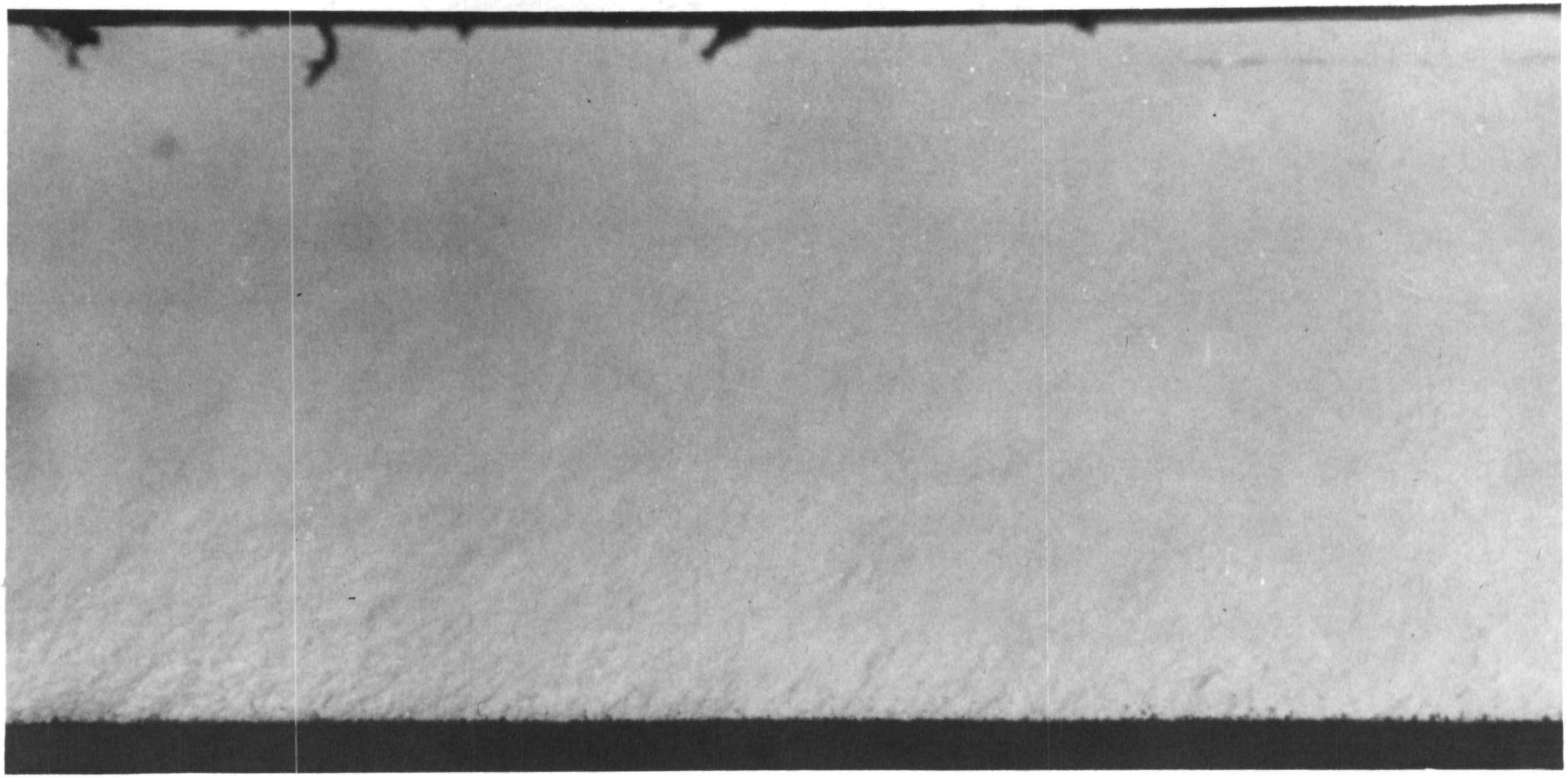

Fig. 13. - Bubbly boundary layer on heating surface.

(b) $p = 13.1$ bar
$G = 2170$ kg m^{-2} s^{-1}
$\Delta T_{sub} = 28°C$
$q'' = 210$ kW m^{-2}

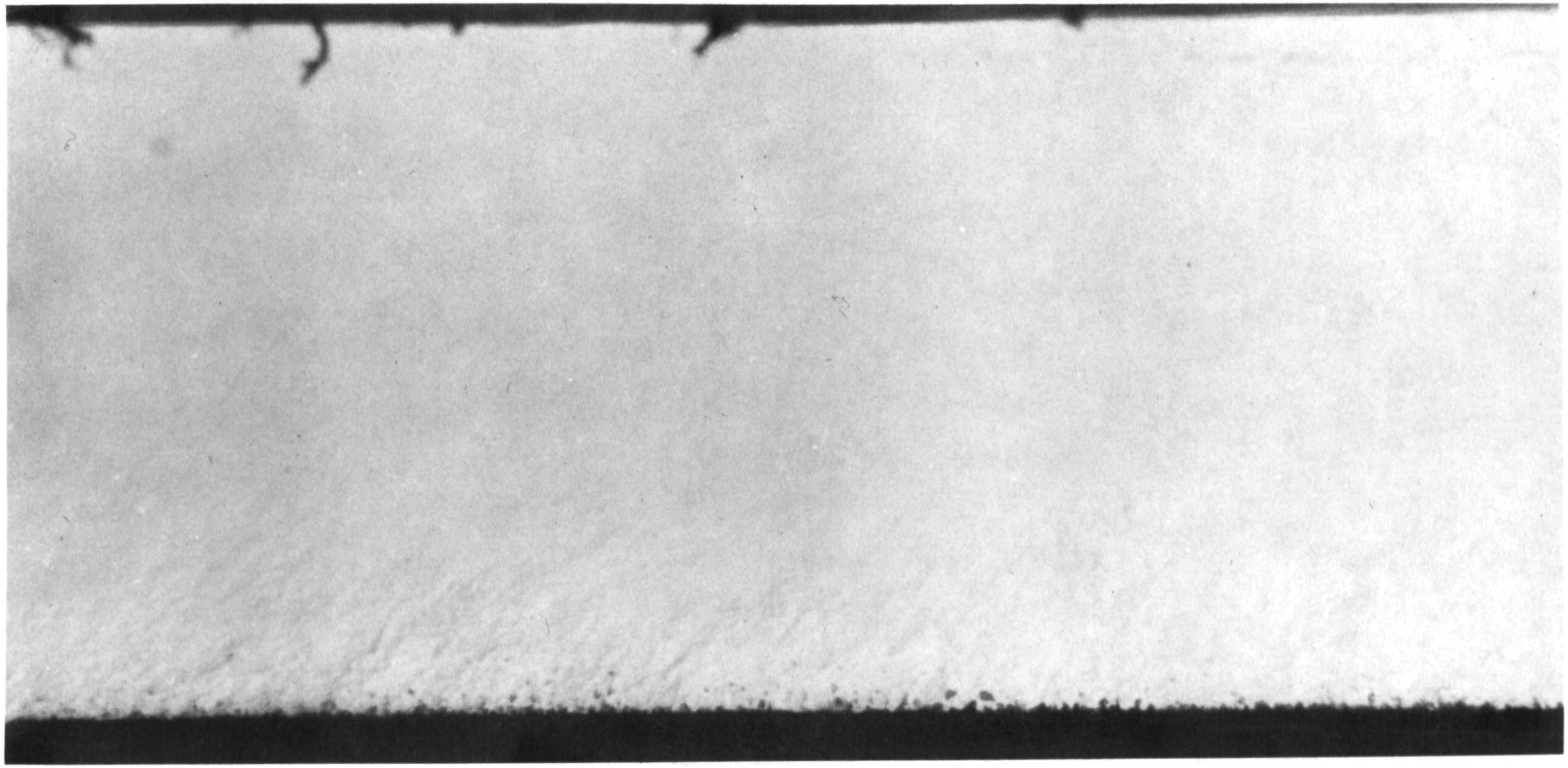

Fig. 13. - Continued.

(c) $p = 13.1$ bar
$G = 2170$ kg m^{-2} s^{-1}
$\Delta T_{sub} = 28°C$
$q'' = 270$ kW m^{-2}

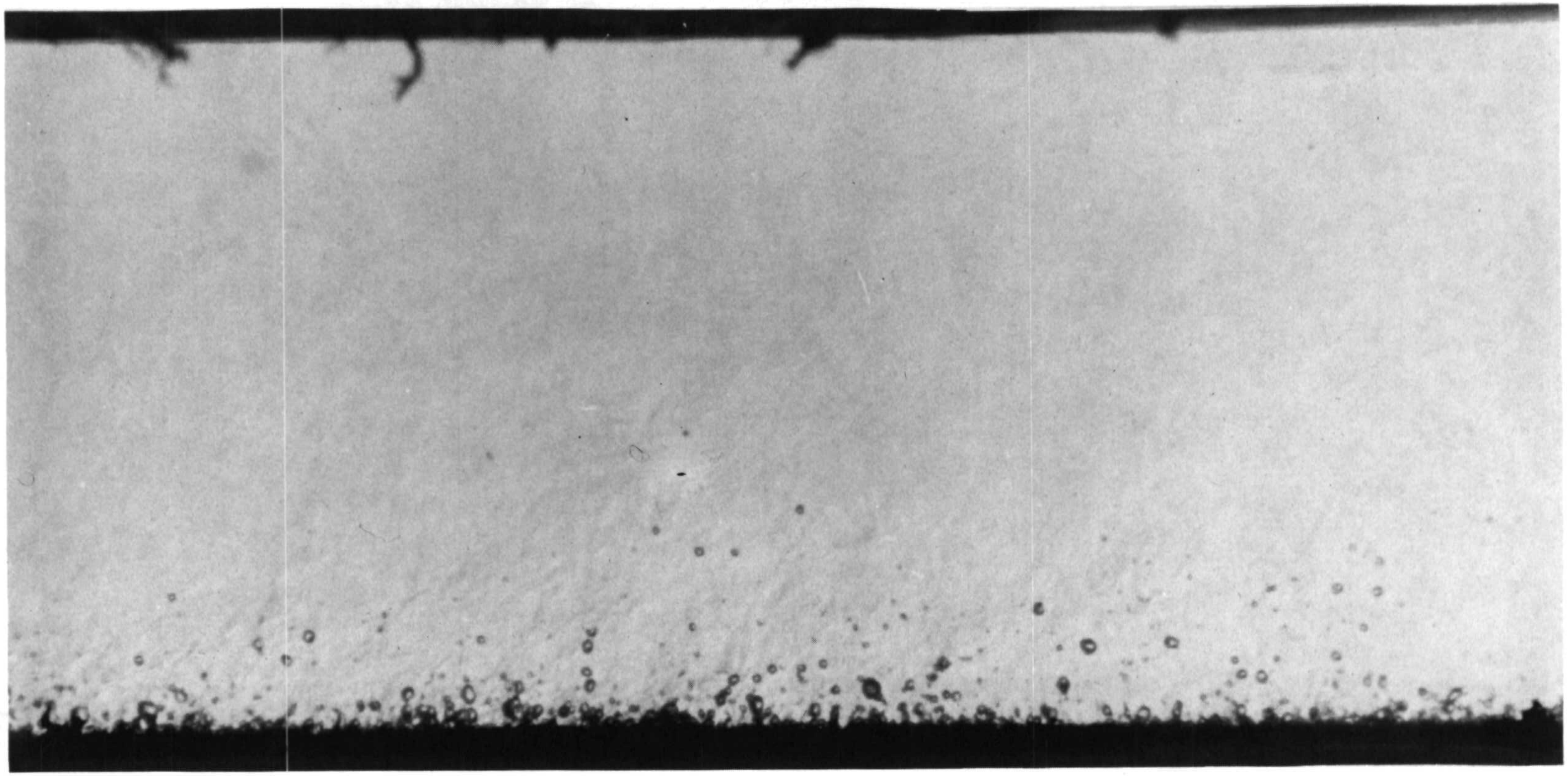

Fig. 13. - Continued.

(d) p = 13.1 bar
G = 2170 kg m^{-2} s^{-1}
ΔT_{sub} = 28°C
q'' = 381 kW m^{-2}

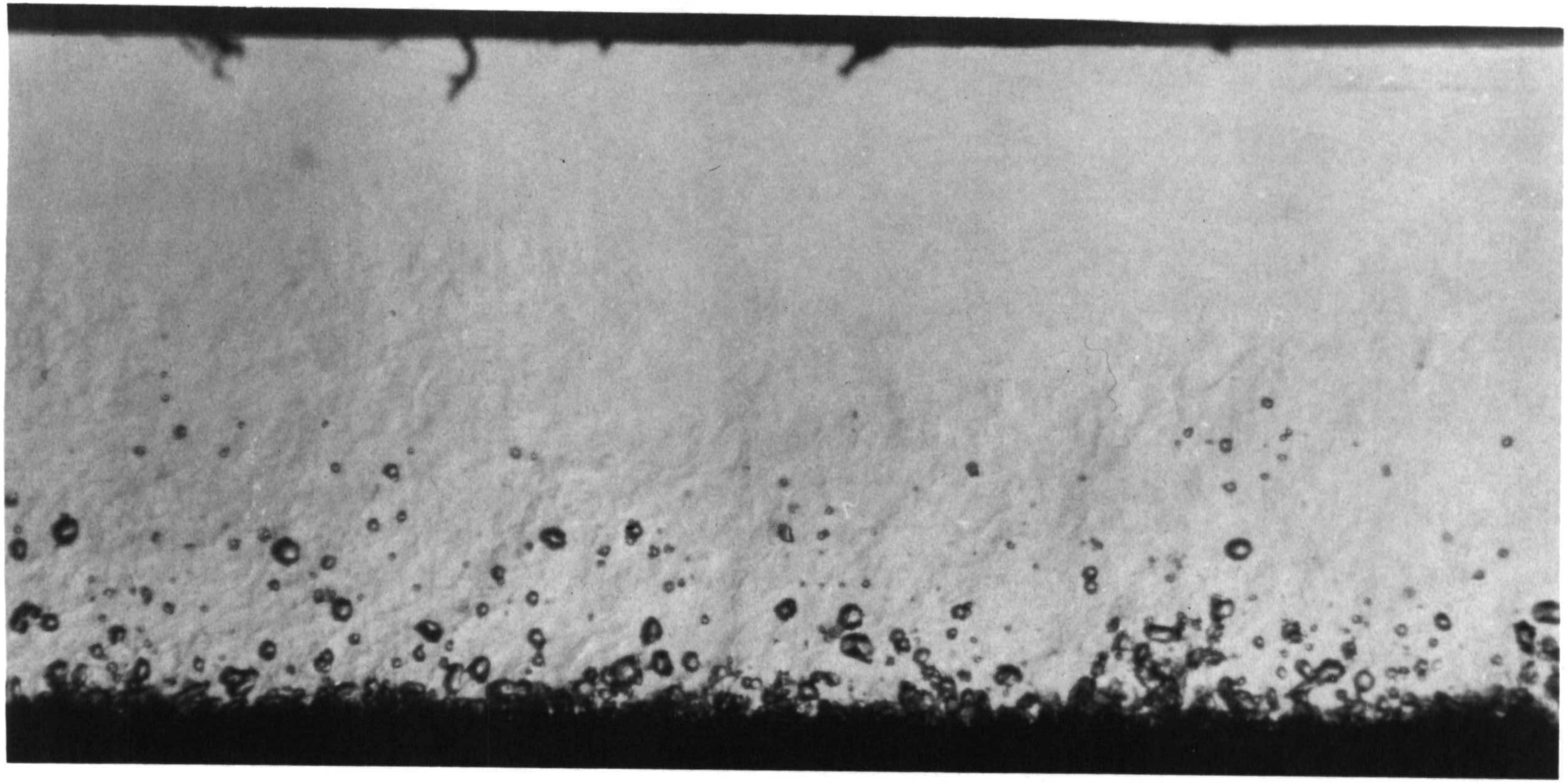

Fig. 13. - Concluded.

(a) $p = 13.1$ bar
$G = 5830$ kg m^{-2} s^{-1}
$\Delta T_{sub} = 17°C$
$q'' = 236$ kW m^{-2}

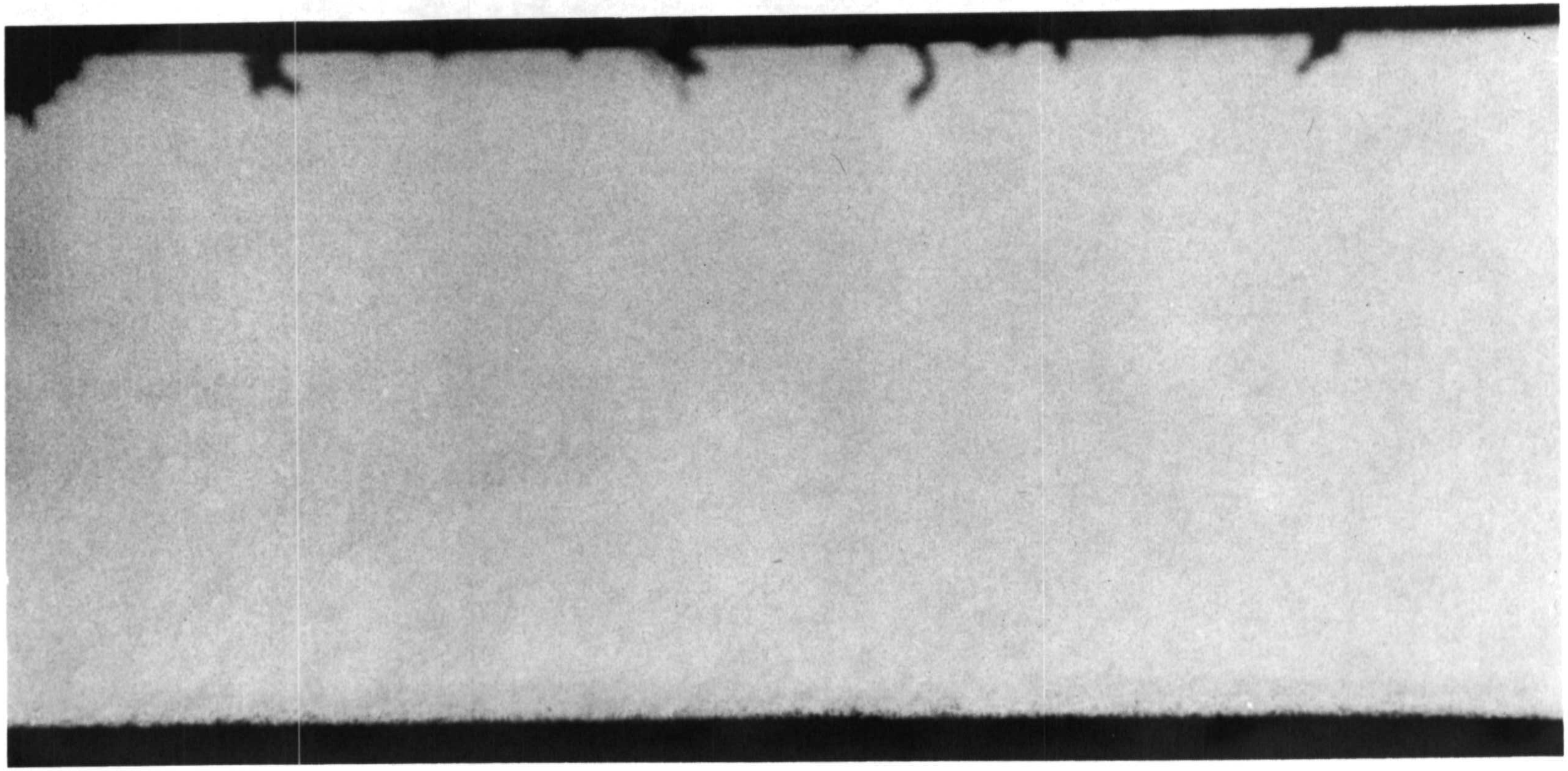

Fig. 14. - Bubbly boundary layer on heating surface.

(b) $p = 13.1$ bar
$G = 5830$ kg m^{-2} s^{-1}
$\Delta T_{sub} = 17°C$
$q'' = 270$ kW m^{-2}

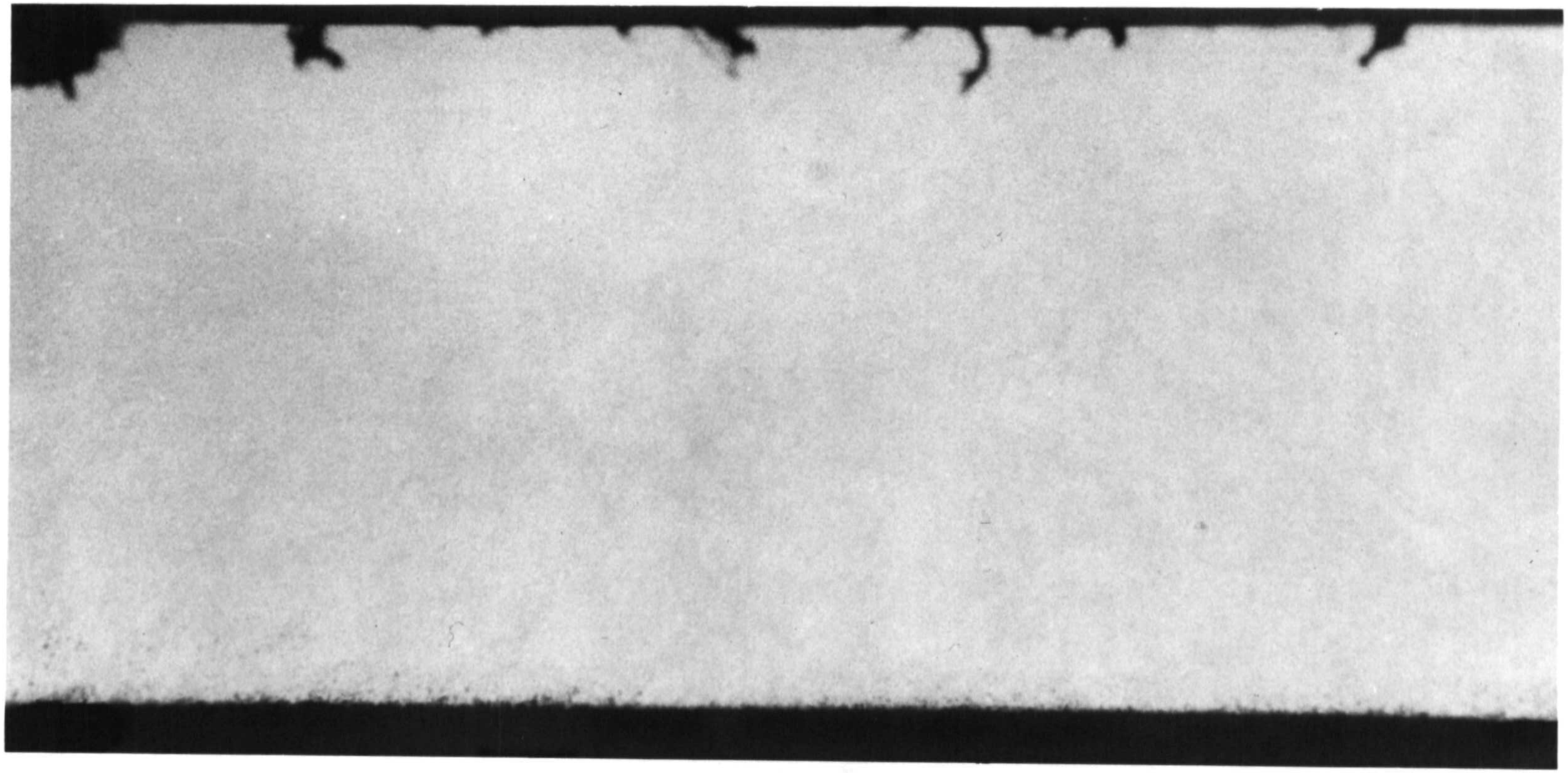

Fig. 14. - Continued.

(c) $p = 13.1$ bar
$G = 5830$ kg m^{-2}
$\Delta T_{sub} = 17$°C
$q'' = 303$ kW m^{-2}

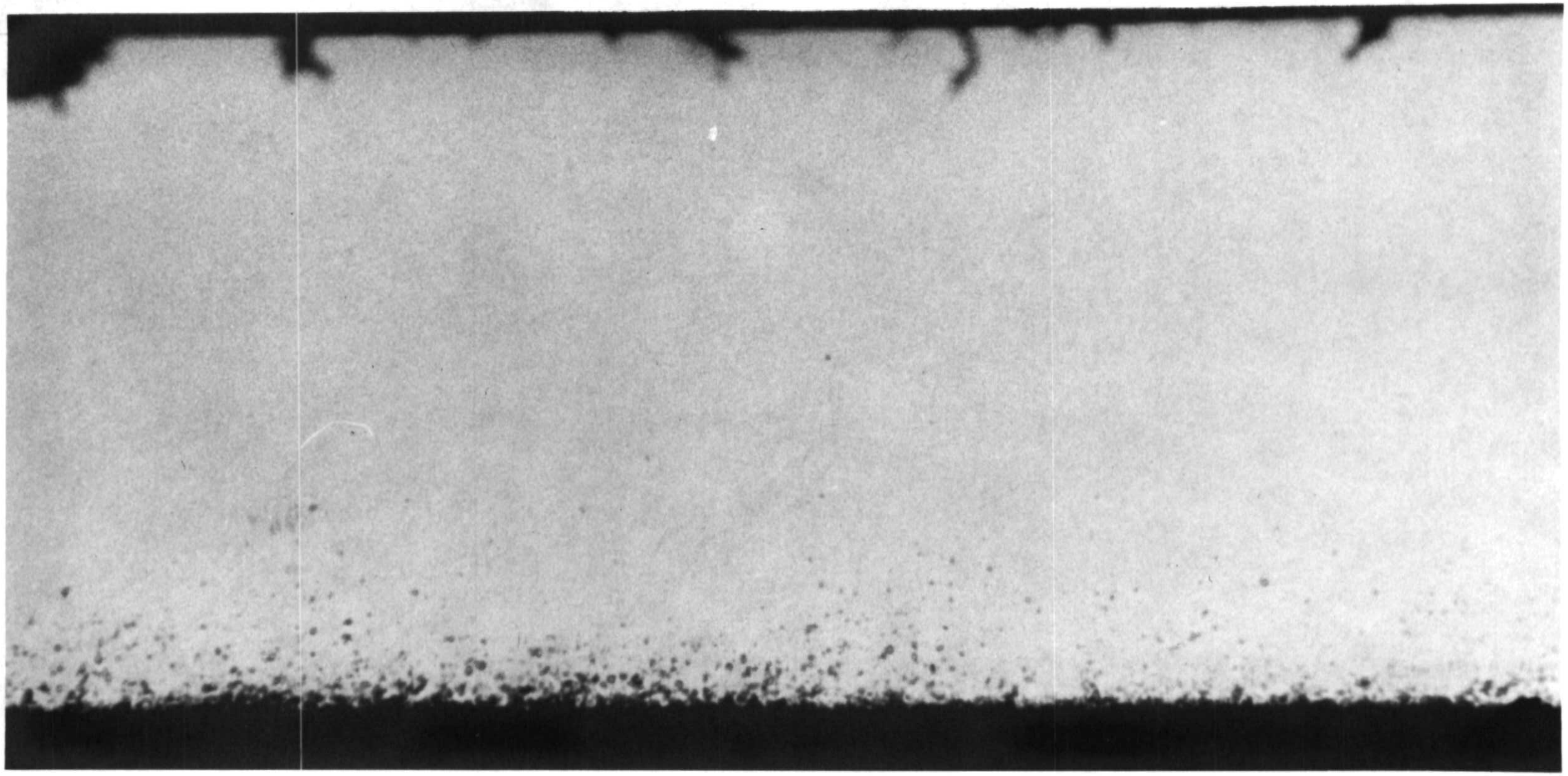

Fig. 14. - Continued.

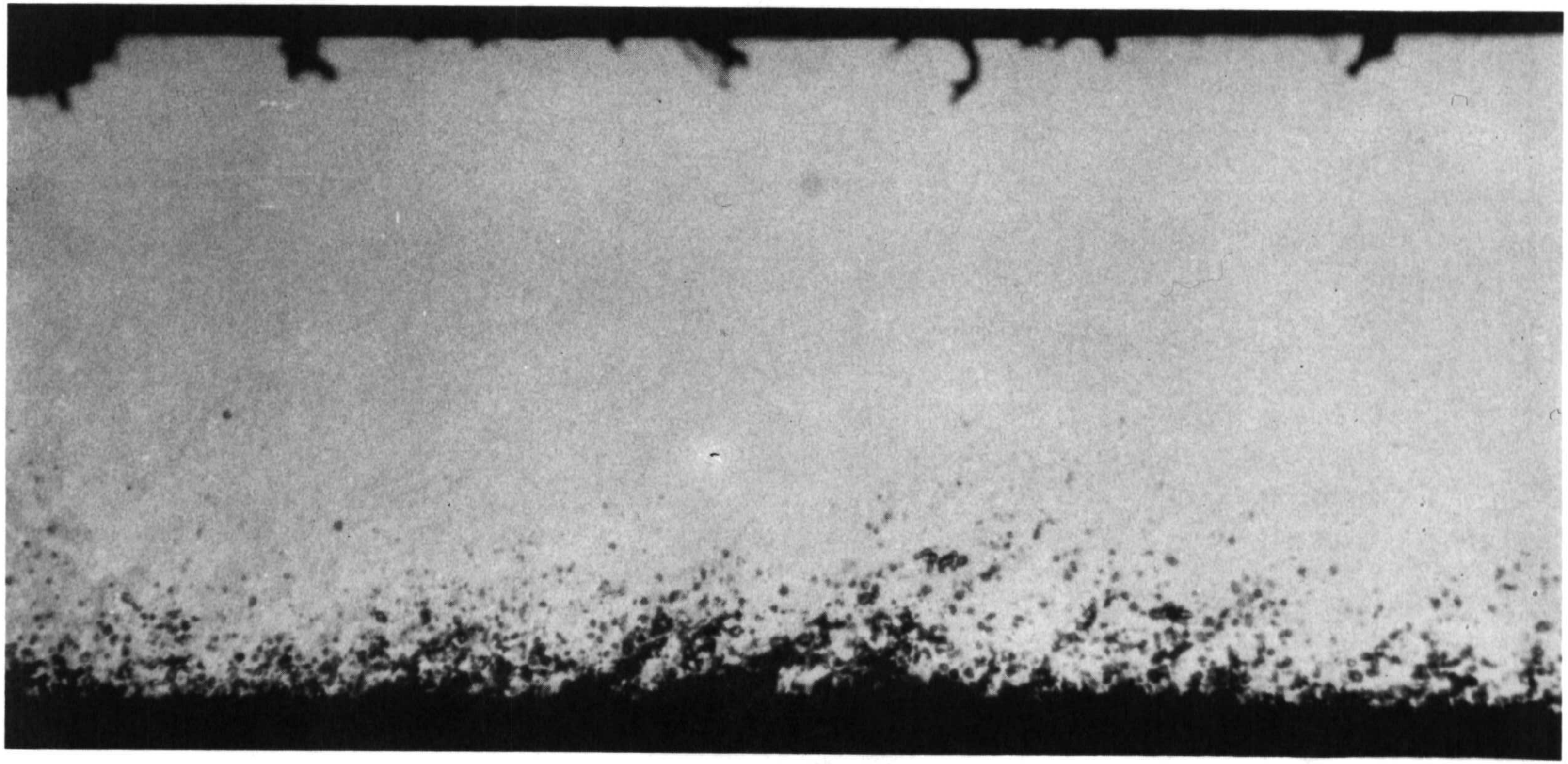

(d) $p = 13.1$ bar
$G = 5830$ kg m^{-2} s^{-1}
$\Delta T_{sub} = 17°C$
$q'' = 419$ kW m^{-2}

Fig. 14. - Concluded.

(a) $p = 20.7$ bar
$G = 2030$ kg m^{-2} s^{-1}
$\Delta T_{sub} = 30$°C
$q'' = 202$ kW m^{-2}

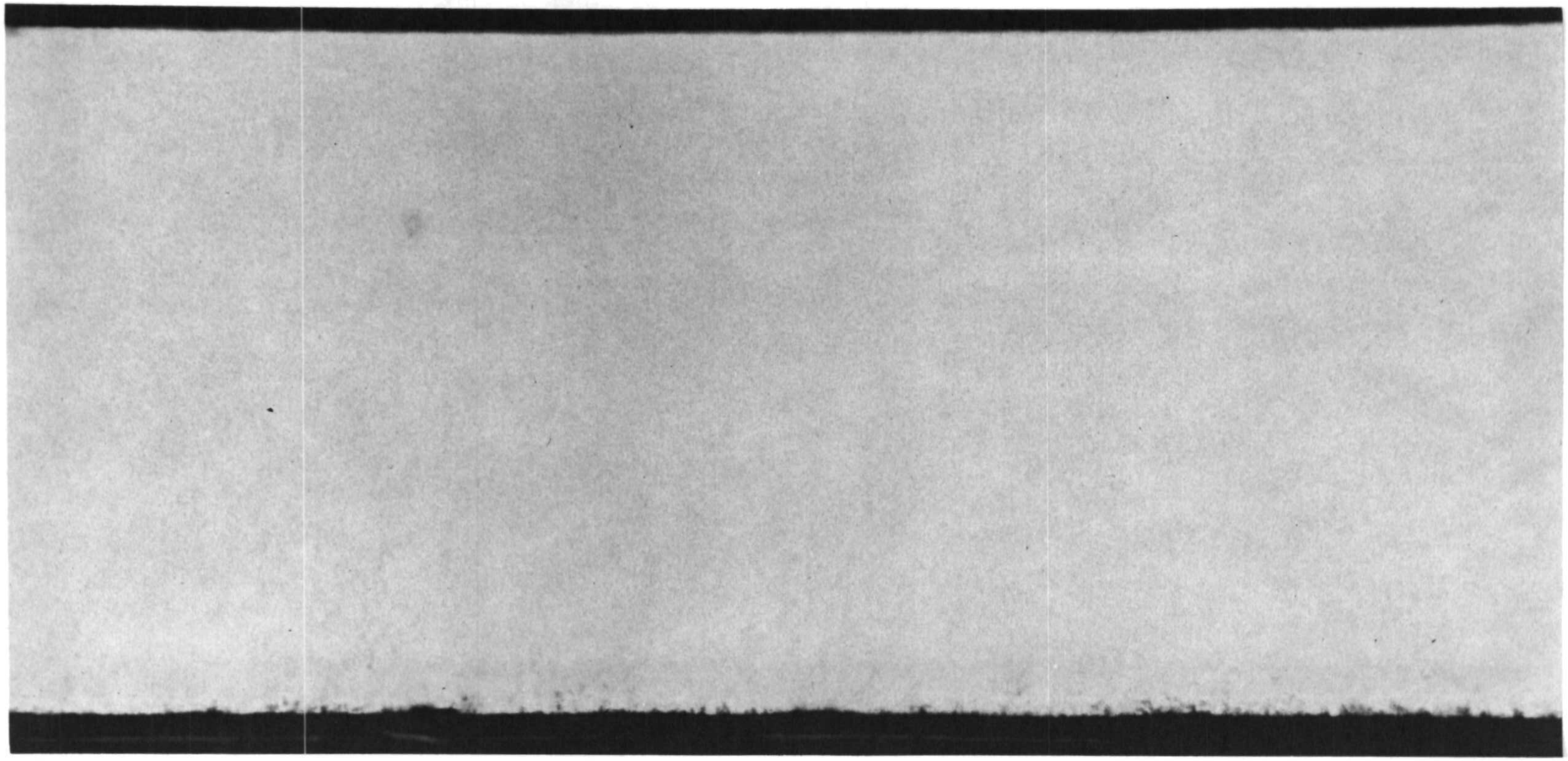

Fig. 15. - Bubbly boundary layer on heating surface.

(b) $p = 20.7$ bar

$G = 2030$ kg m^{-2} s^{-1}

$\Delta T_{sub} = 30°C$

$q'' = 230$ kW m^{-2}

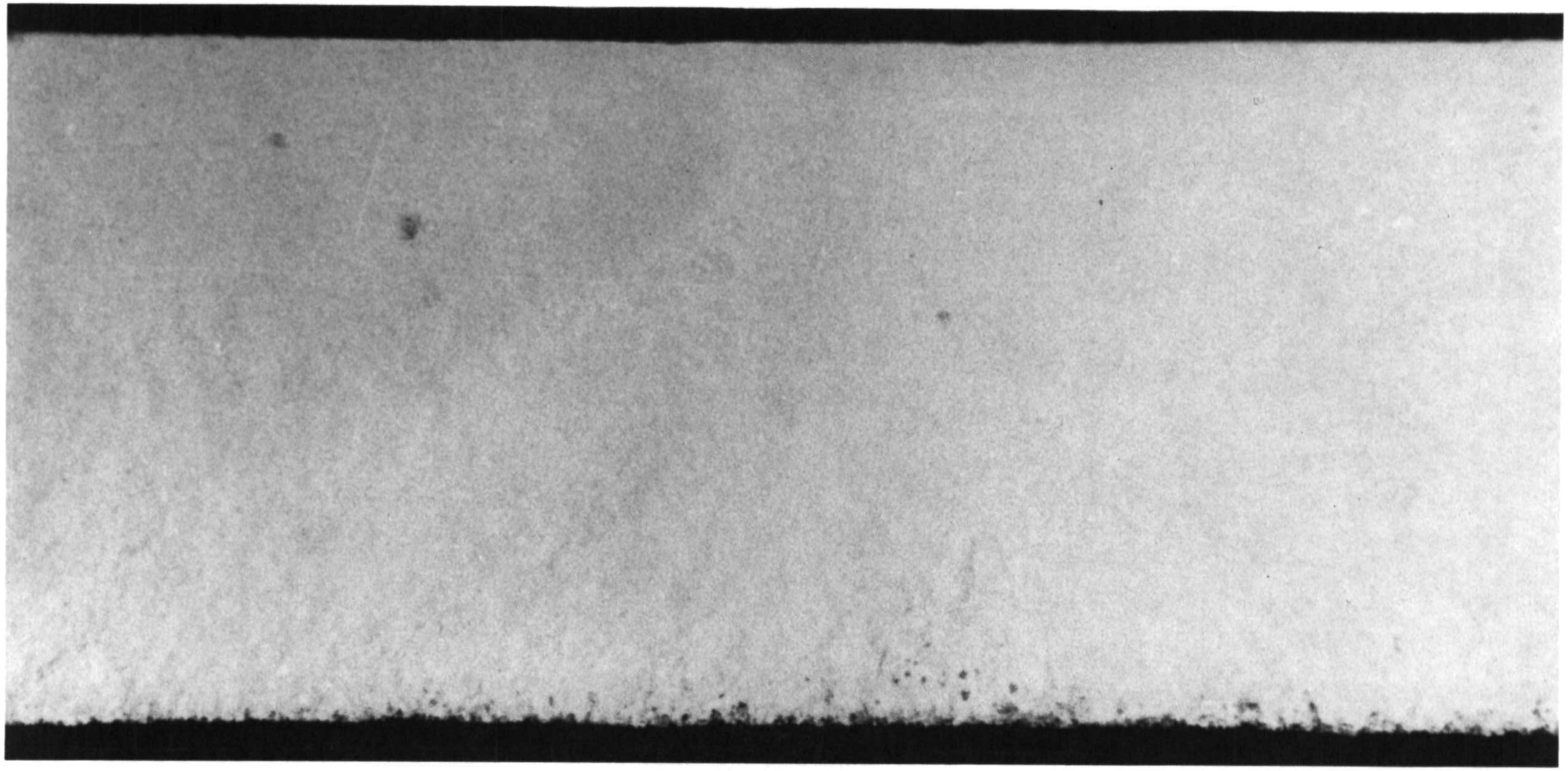

Fig. 15. - Continued.

(c) $p = 20.7$ bar
$G = 2030$ kg m^{-2} s^{-1}
$\Delta T_{sub} = 31°C$
$q'' = 292$ kW m^{-2}

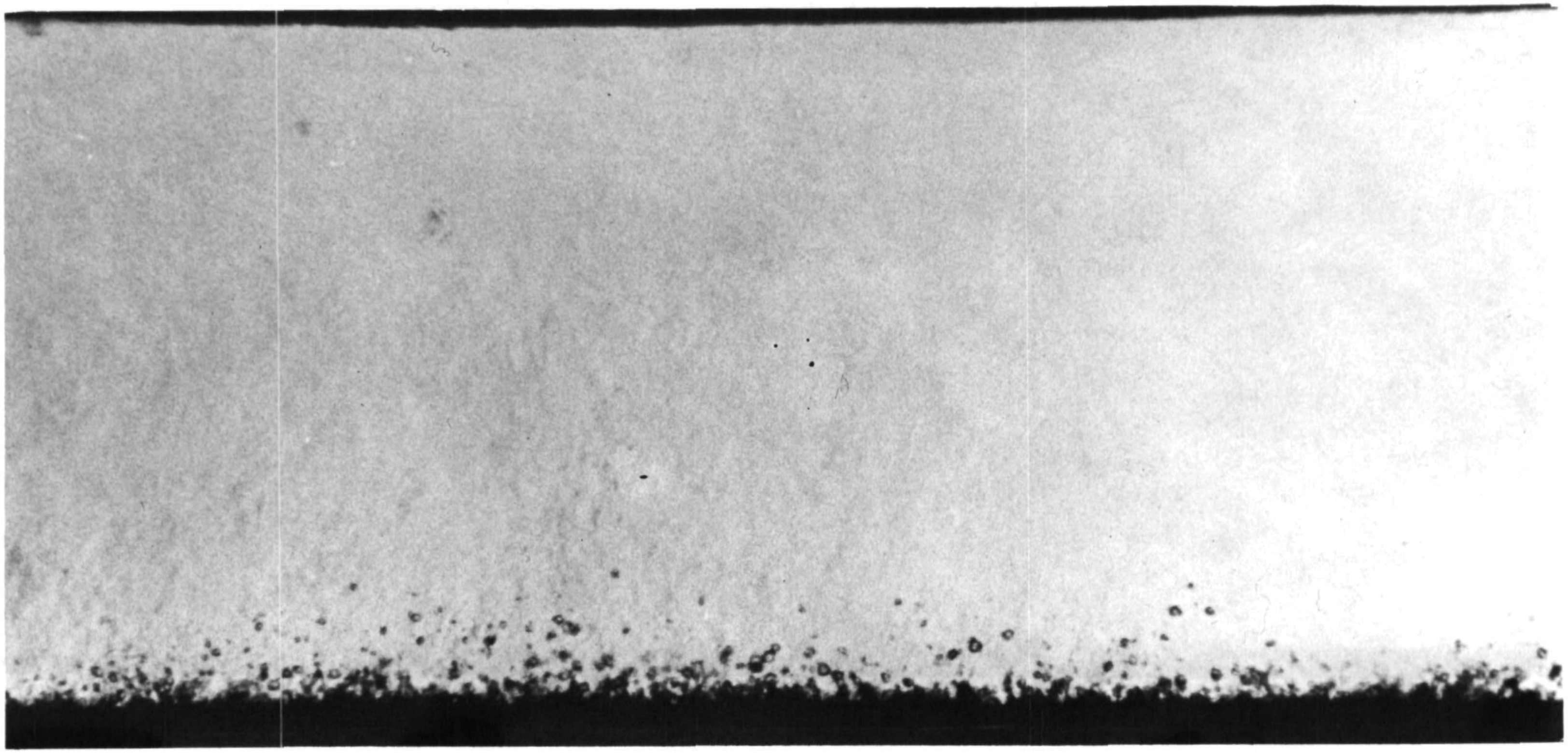

Fig. 15. - Continued.

(b) p = 20.7 bar
G = 5420 kg m^{-2} s^{-1}
ΔT_{sub} = 13°C
q'' = 324 kW m^{-2}

Fig. 16. - Continued.

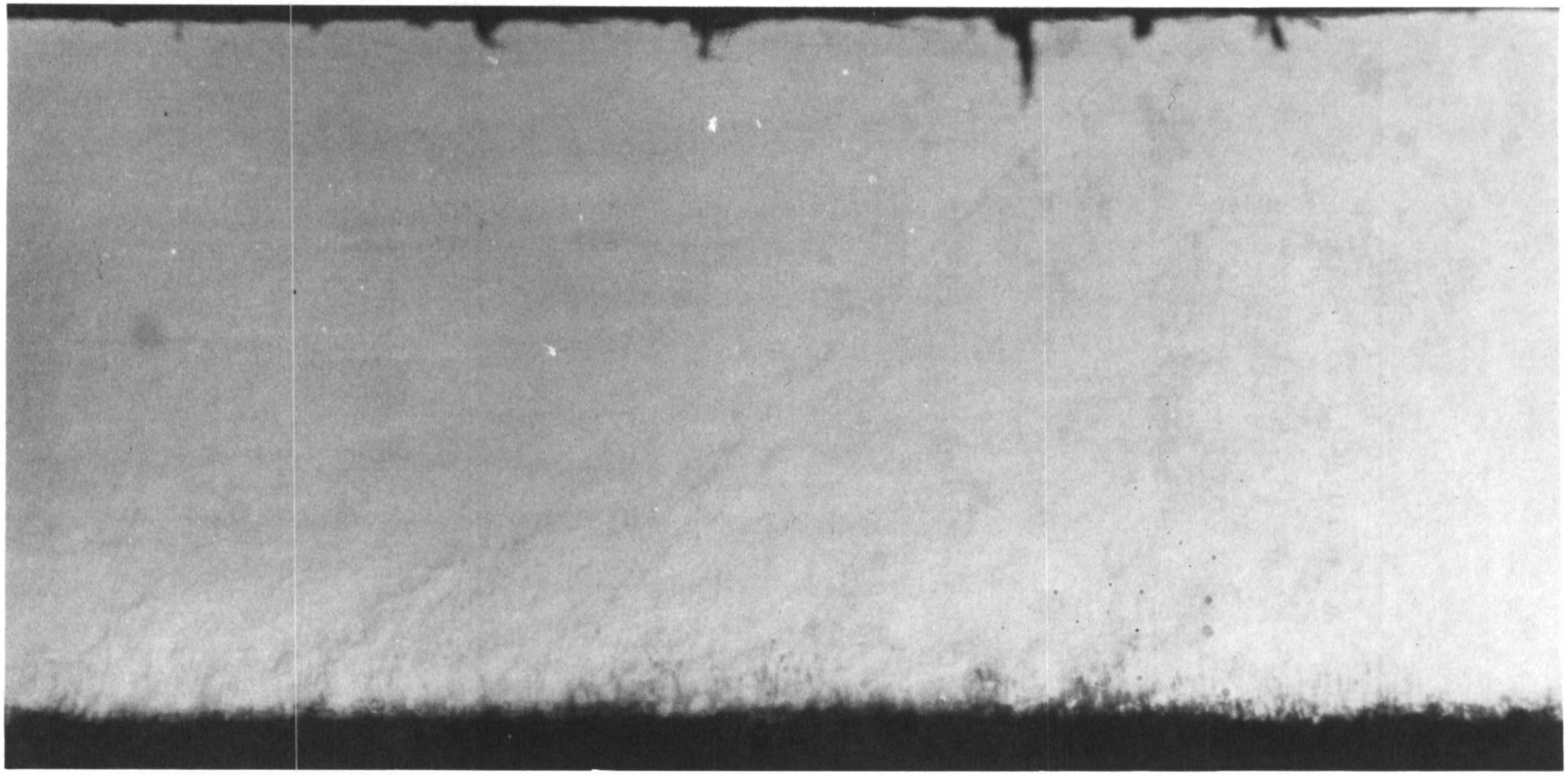

(c) p = 20.7 bar
G = 5420 kg m^{-2} s^{-1}
ΔT_{sub} = 18°C
q'' = 403 kW m^{-2}

Fig. 16. - Concluded.

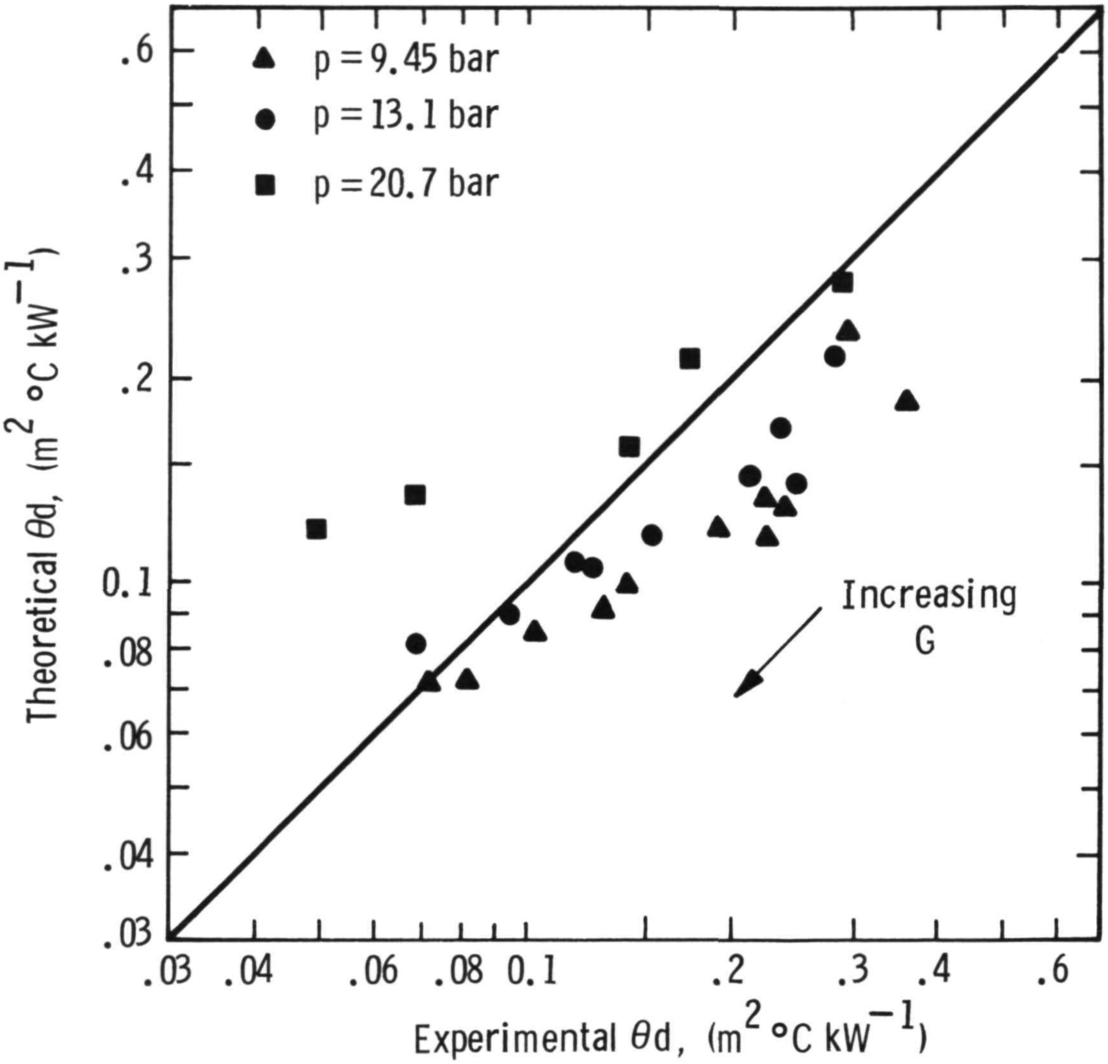

Fig. 17 — Comparison of bubble detachment data with Staub's model (ref. 10)

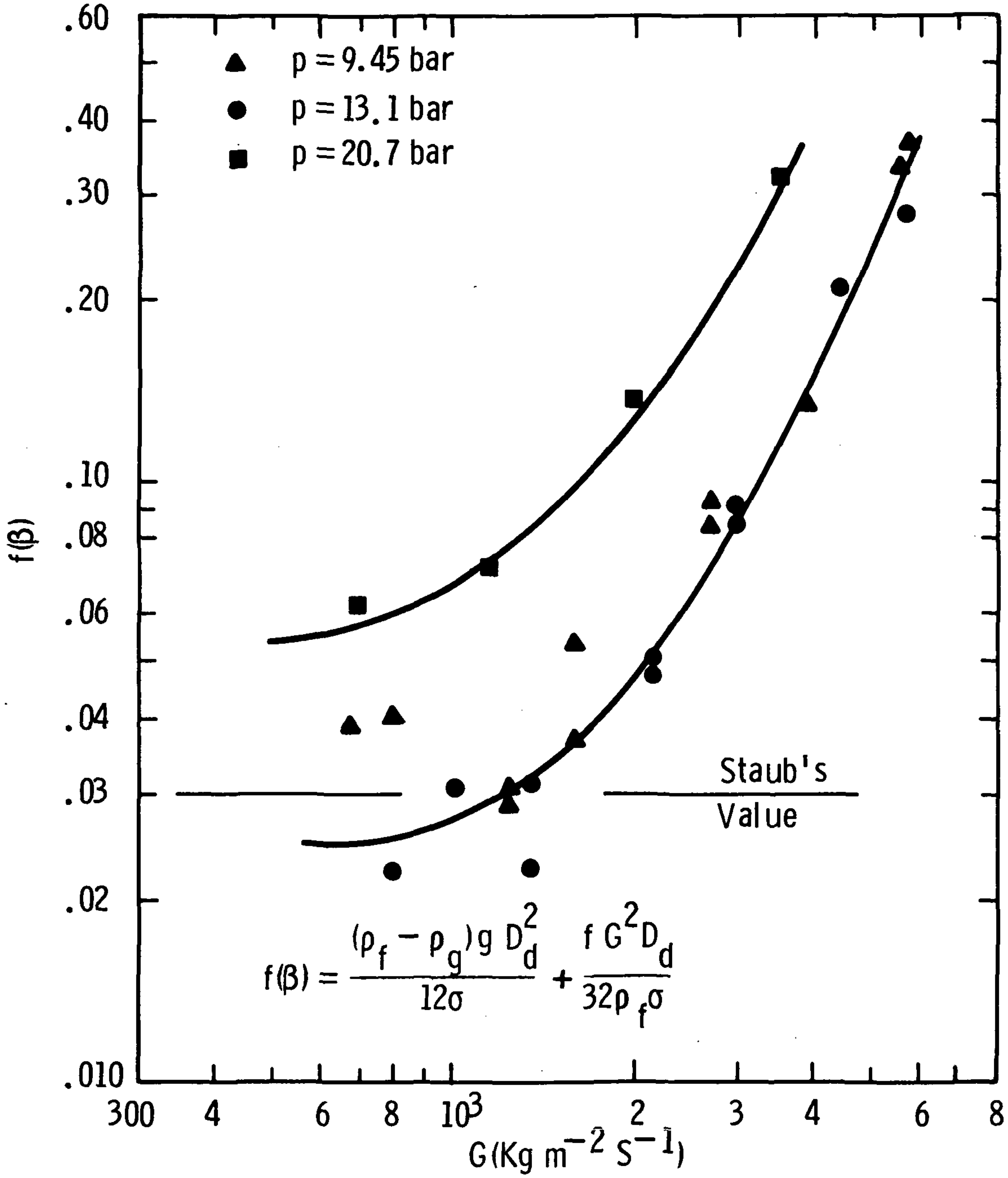

Fig. 18 — Experimental evaluation of f(β) from measured bubble layer thickness

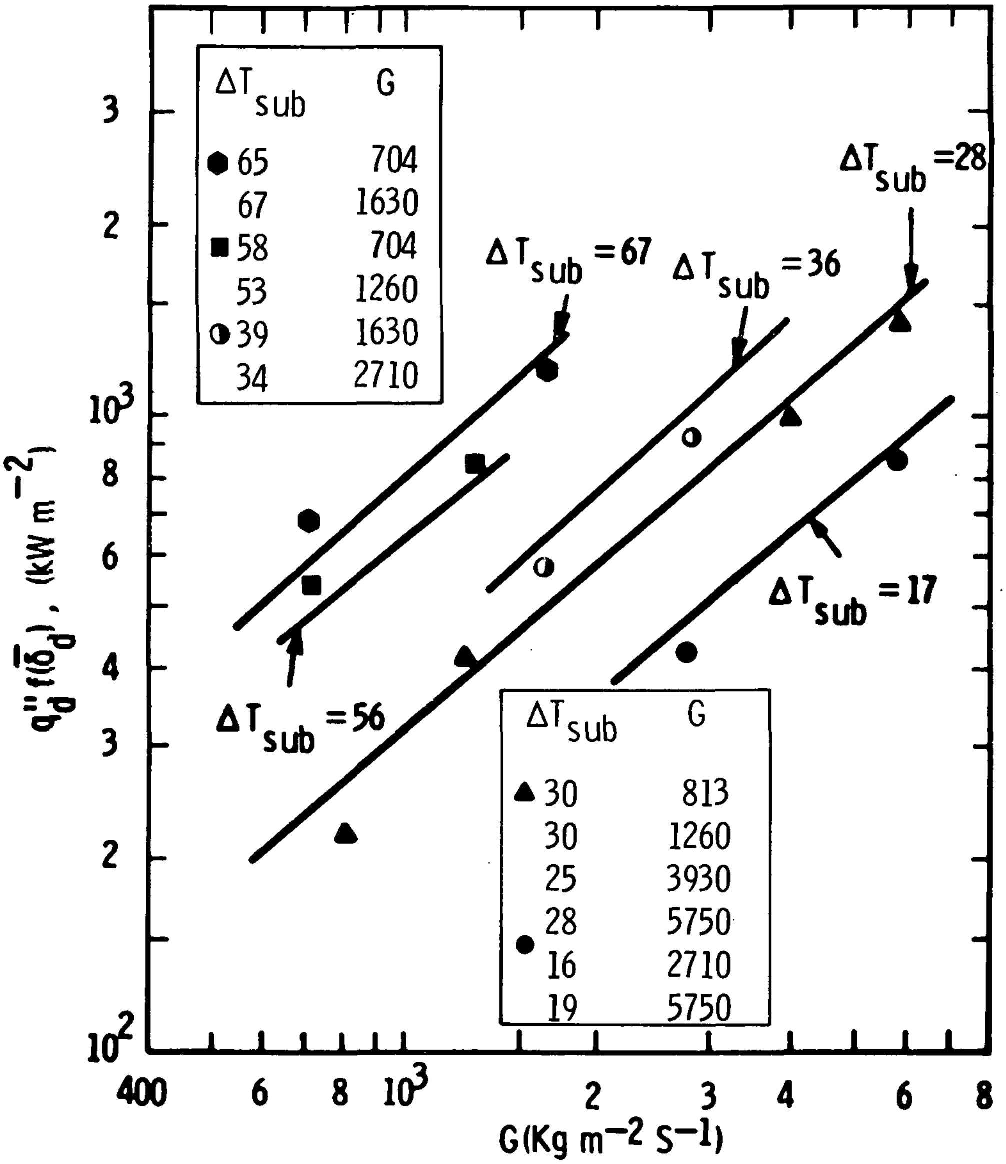

Fig. 19 — Comparison of bubble detachment data with the Larson—Tong model, R—113 and 9.45 bar

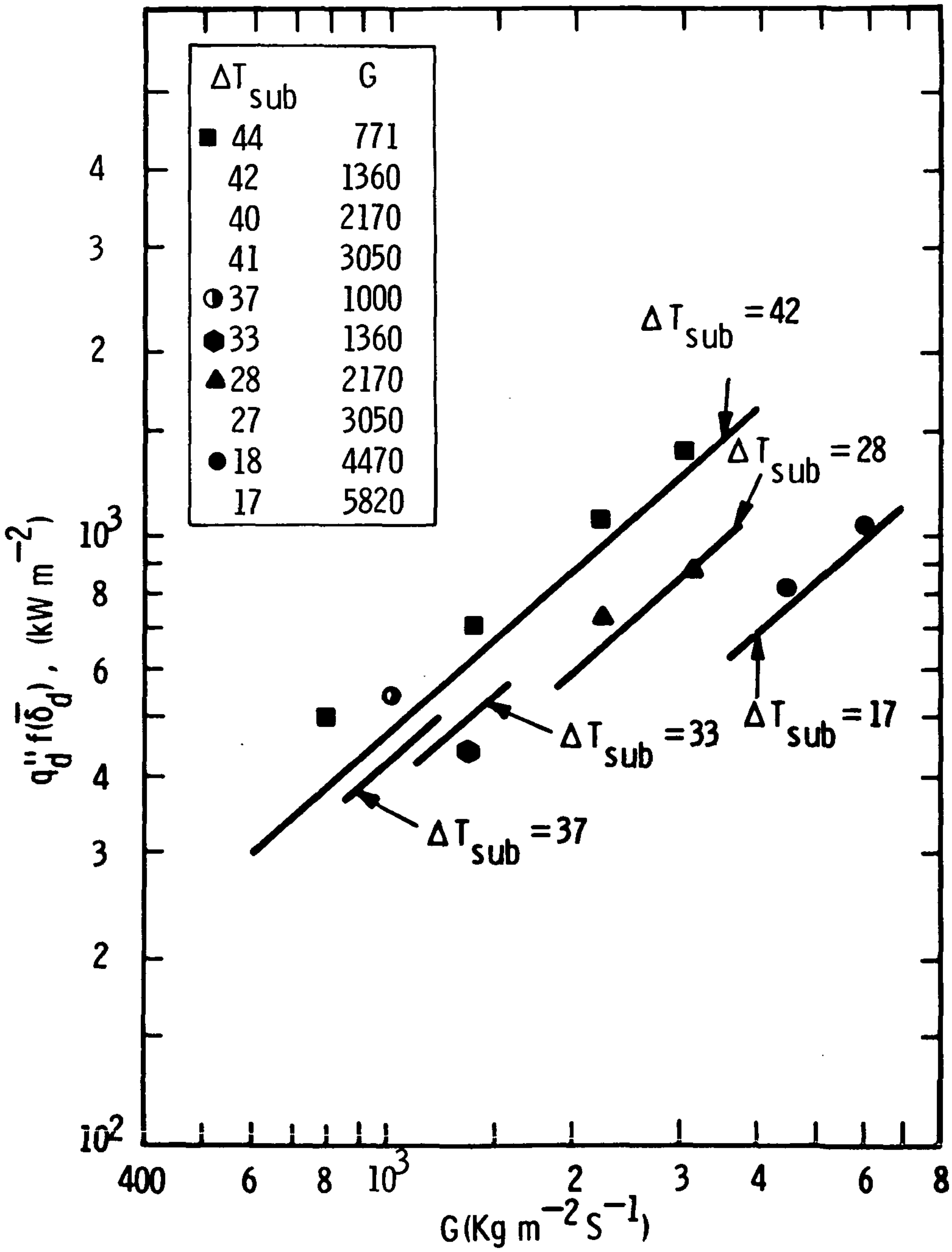

Fig. 20 — Comparison of bubble detachment data with the Larson—Tong model, R—113 and 13.1 bar

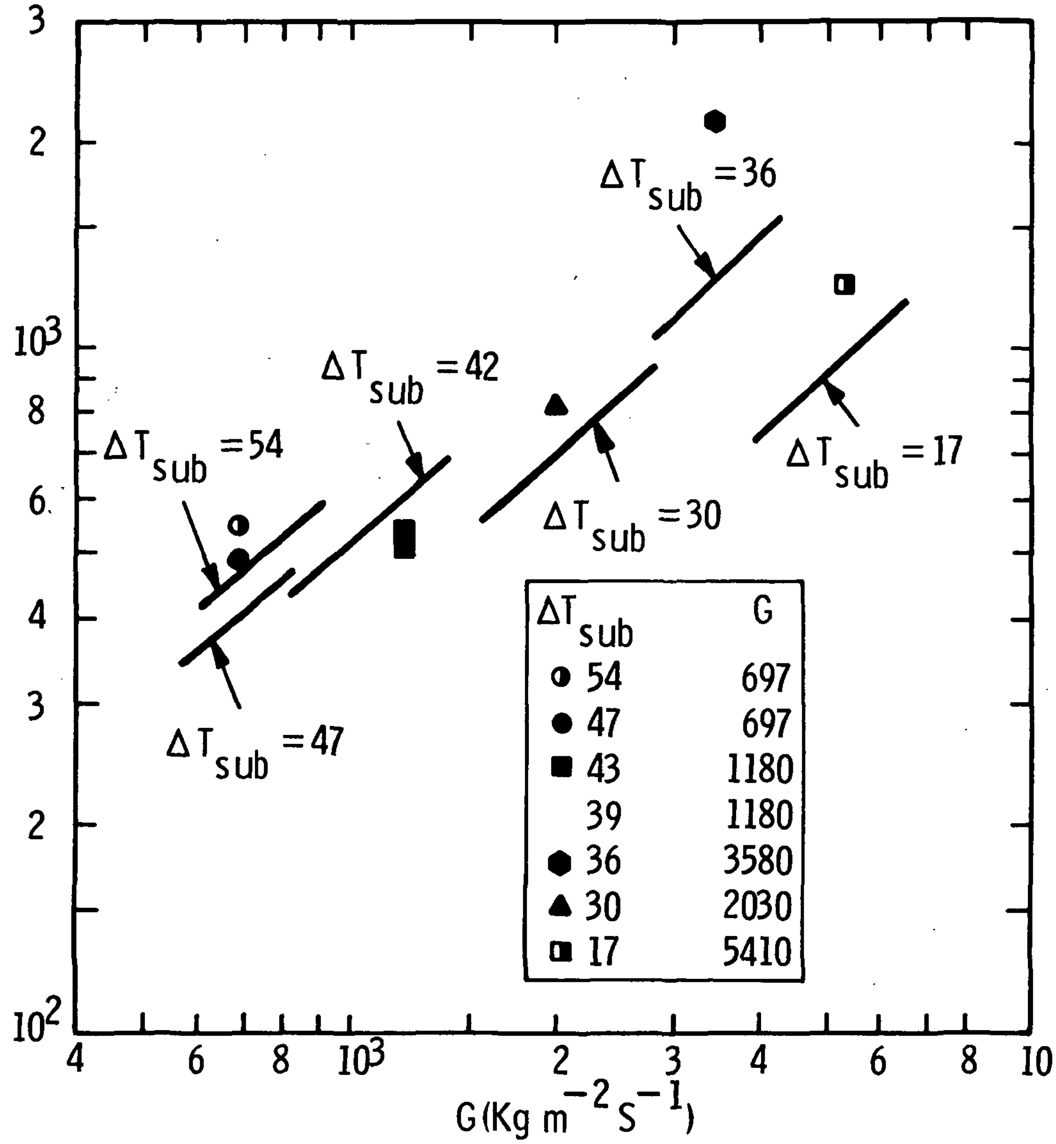

Fig. 21 – Comparison of bubble detachment data with the Larson–Tong model, R–113 and 20.7 bar

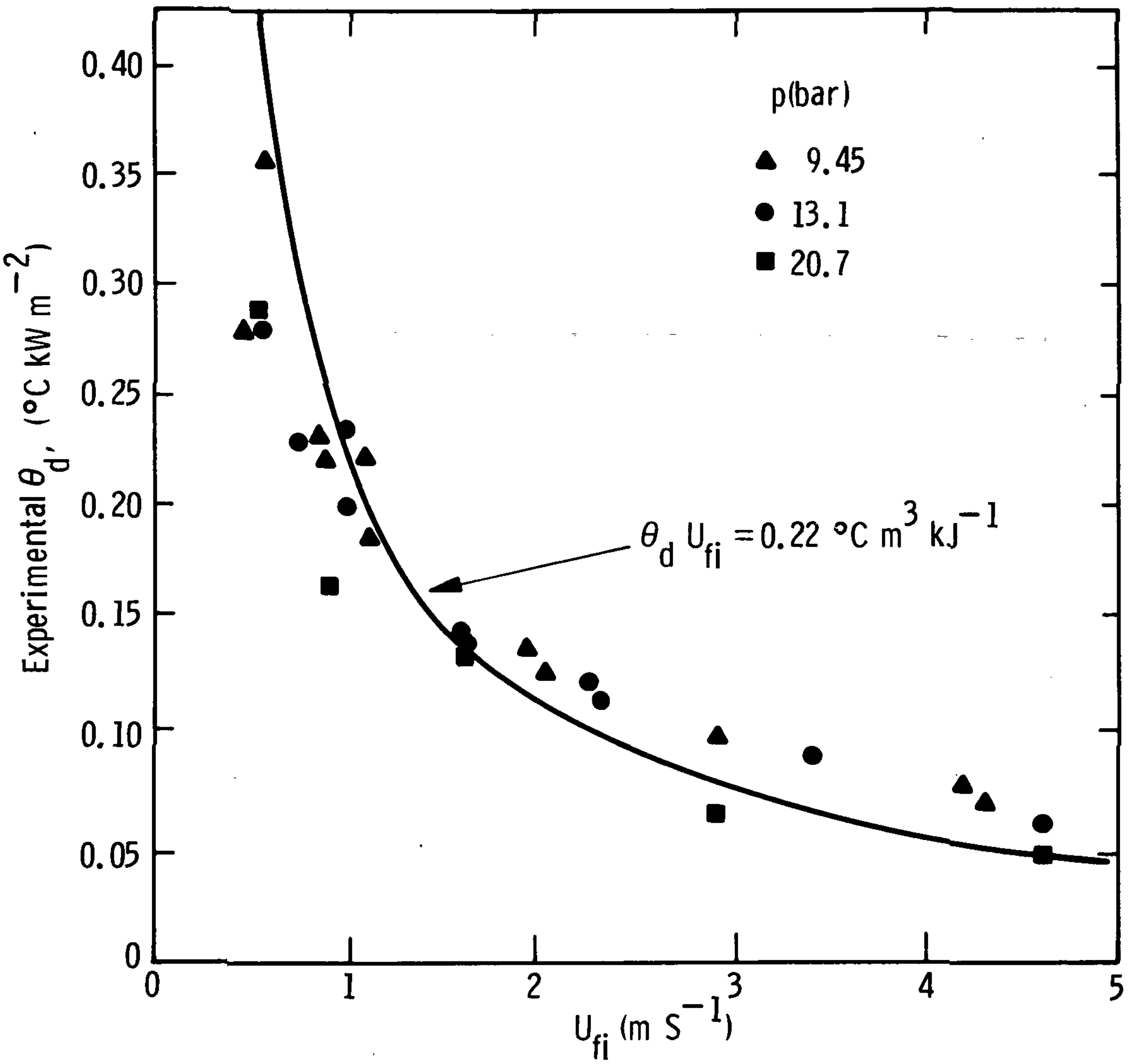

Fig. 22 — Bubble detachment data with Bowring's correlation parameters

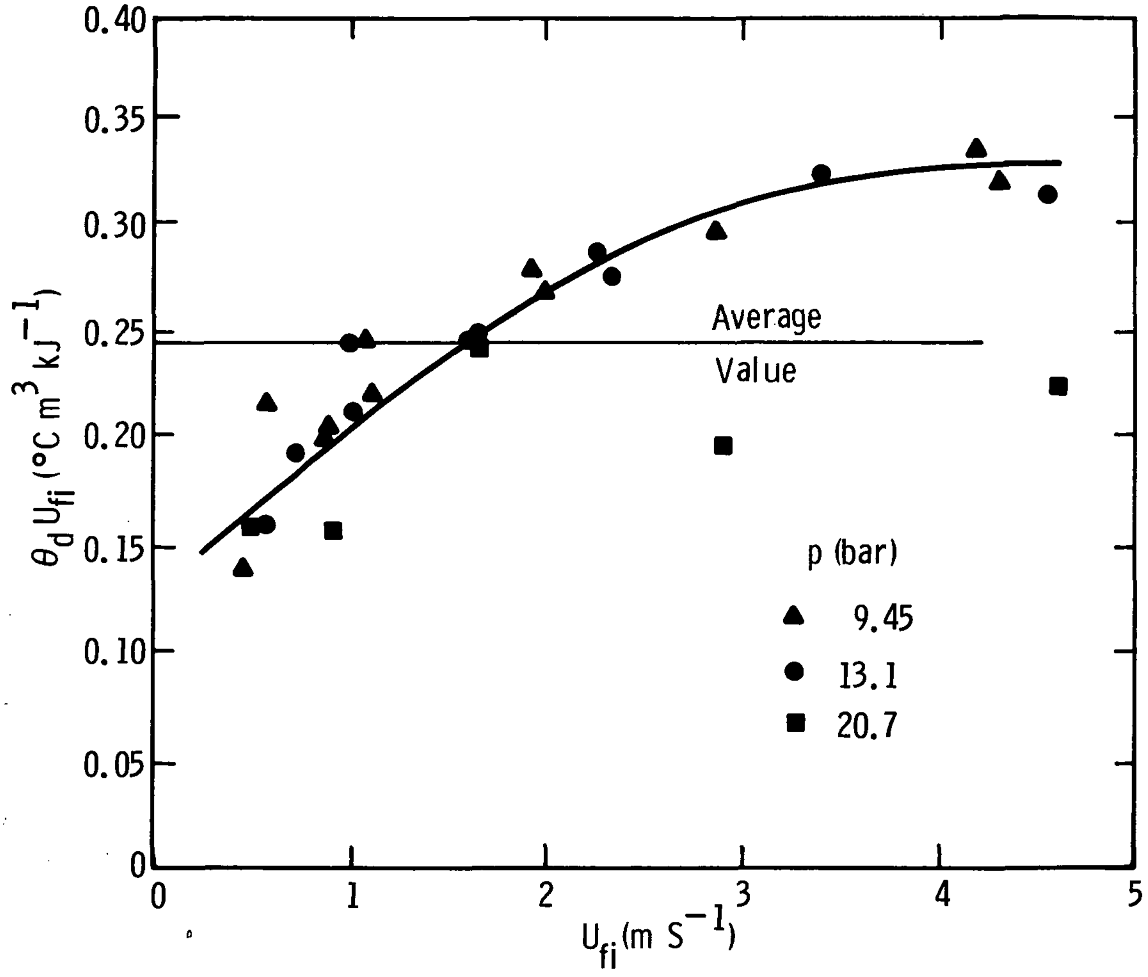

Fig. 23 – Behavior of Bowring's correlation constant based on present R–113 data

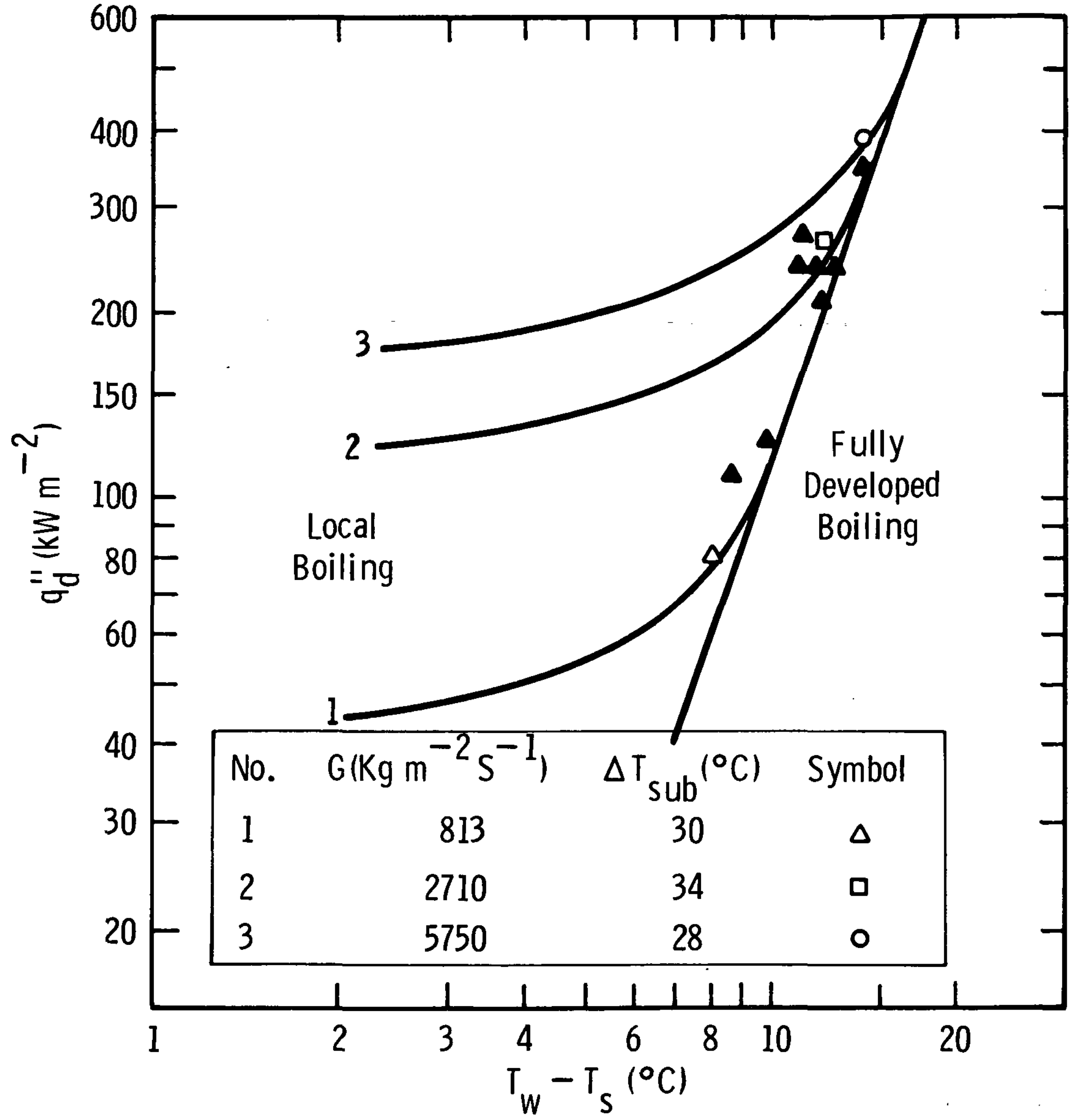

Fig. 24 — Bubble detachment data with boiling curve, R−113 and 9.45 bar

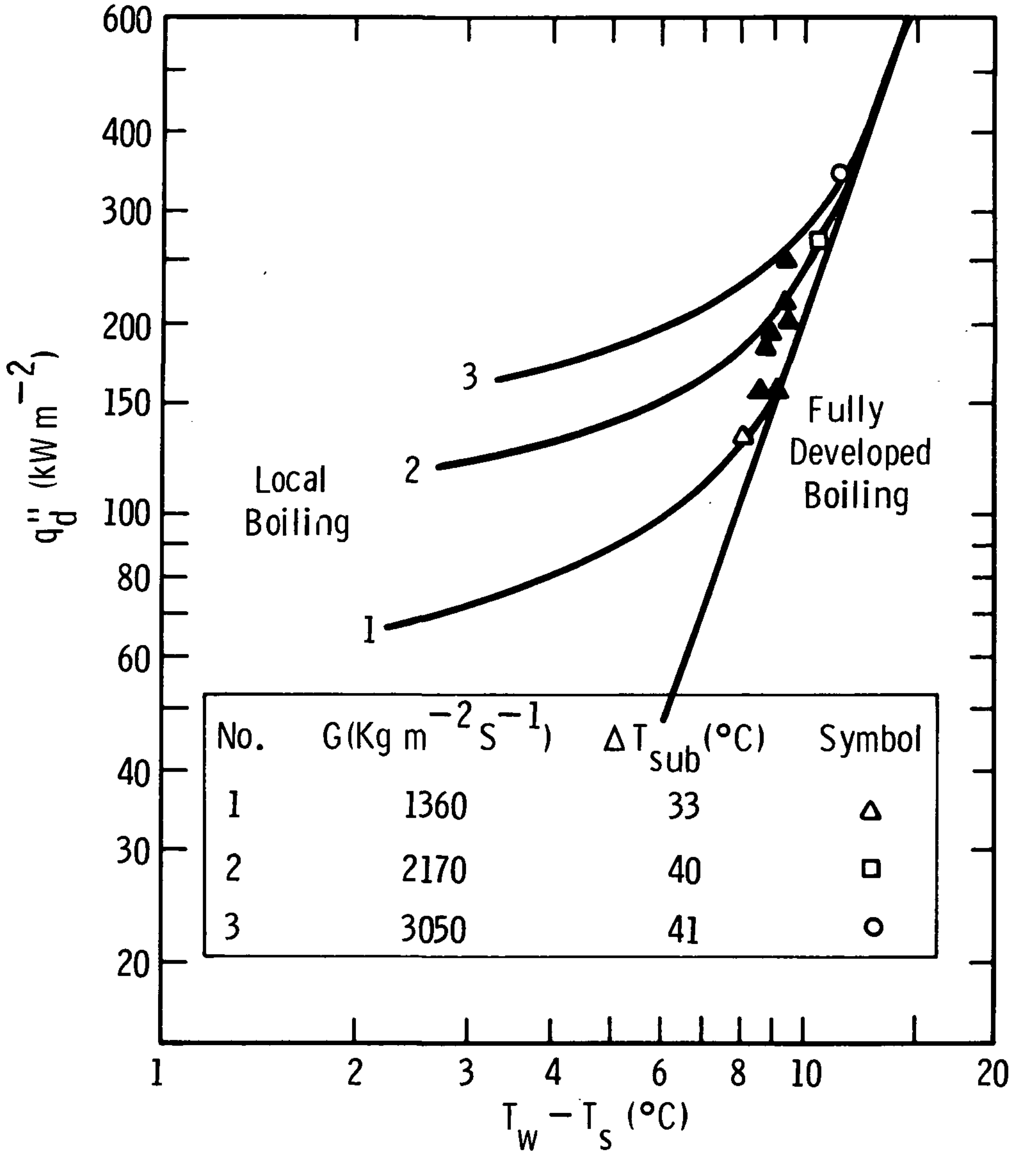

Fig. 25 — Bubble detachment data with boiling curve, R-113 and 13.1 bar

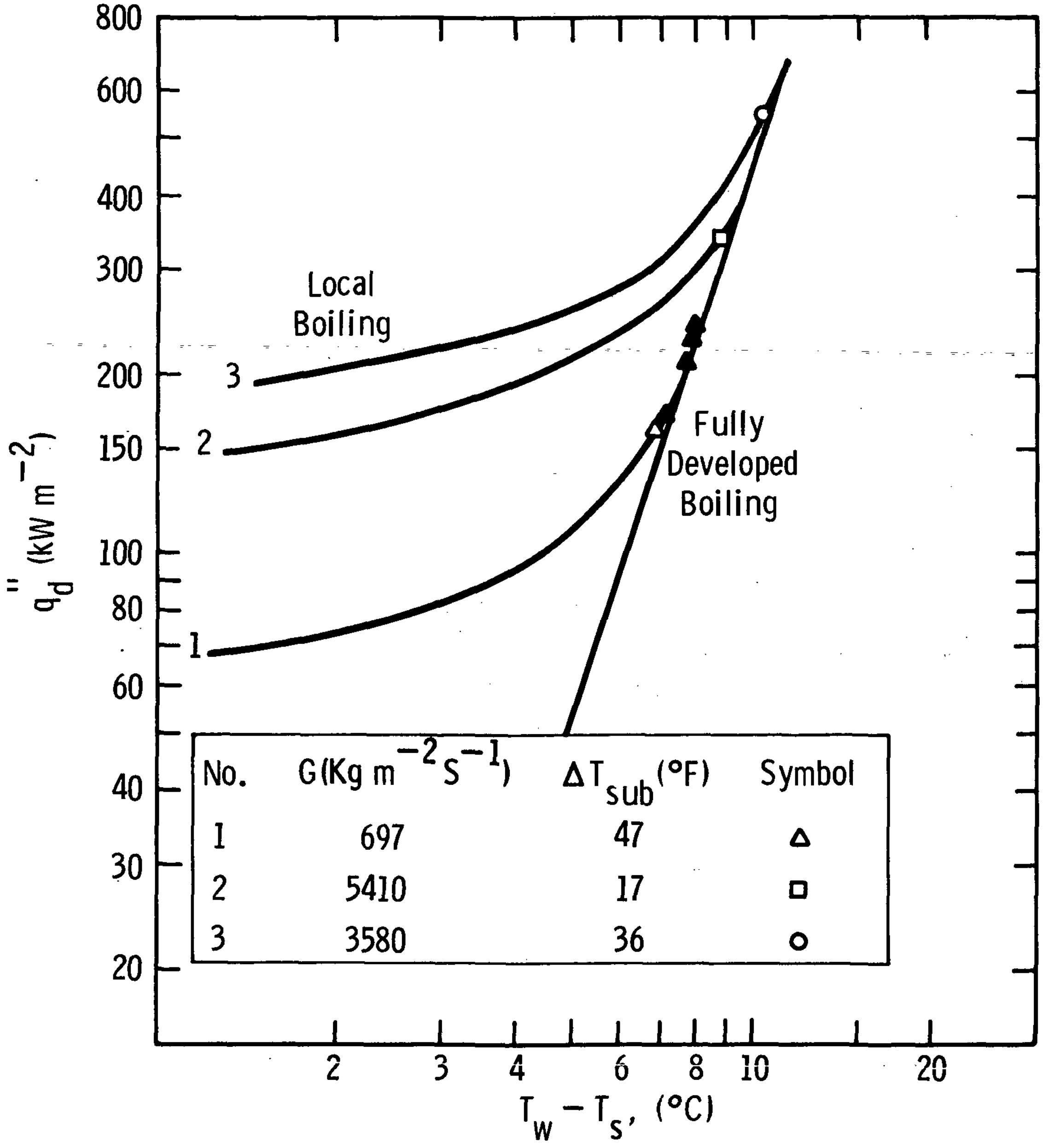

No.	G(Kg m^{-2}S^{-1})	ΔT_{sub}(°F)	Symbol
1	697	47	△
2	5410	17	□
3	3580	36	○

Fig. 26 – Bubble detachment data with boiling curve, R–113 and 20.7 bar

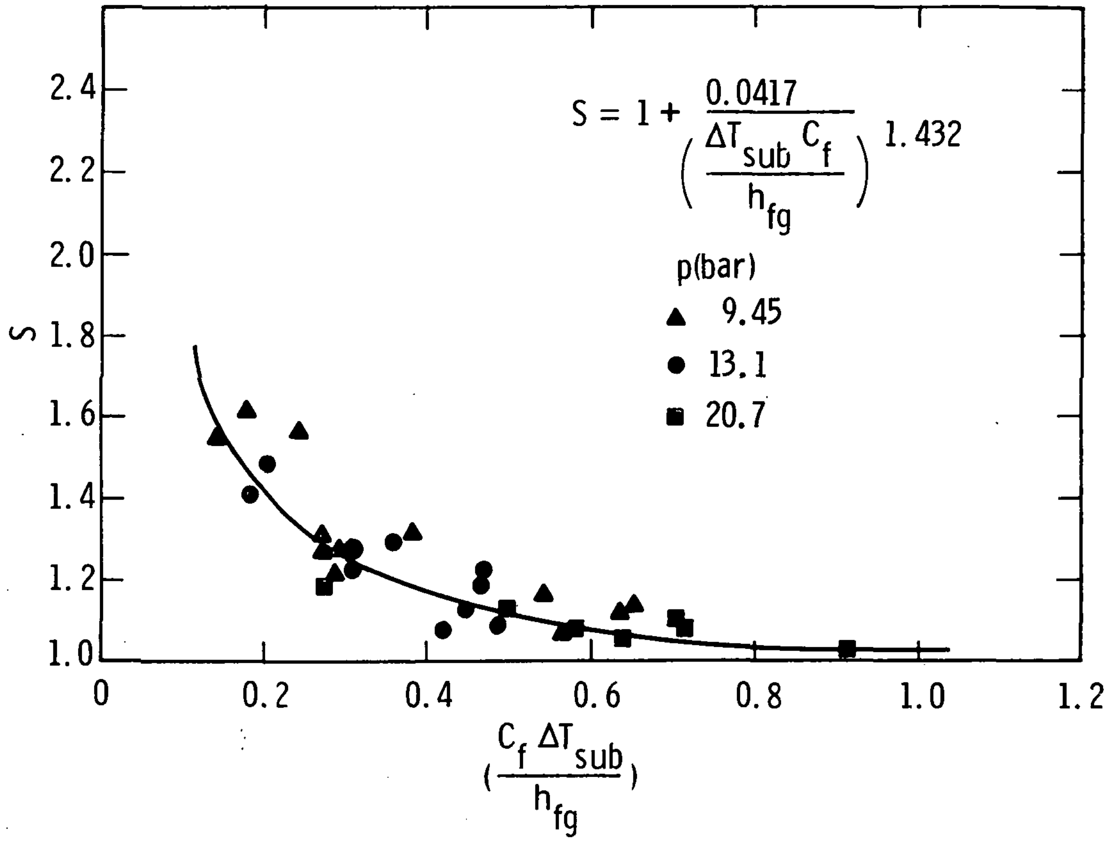

Fig. 27 —Correlation of bubble detachment with fully developed boiling R-113

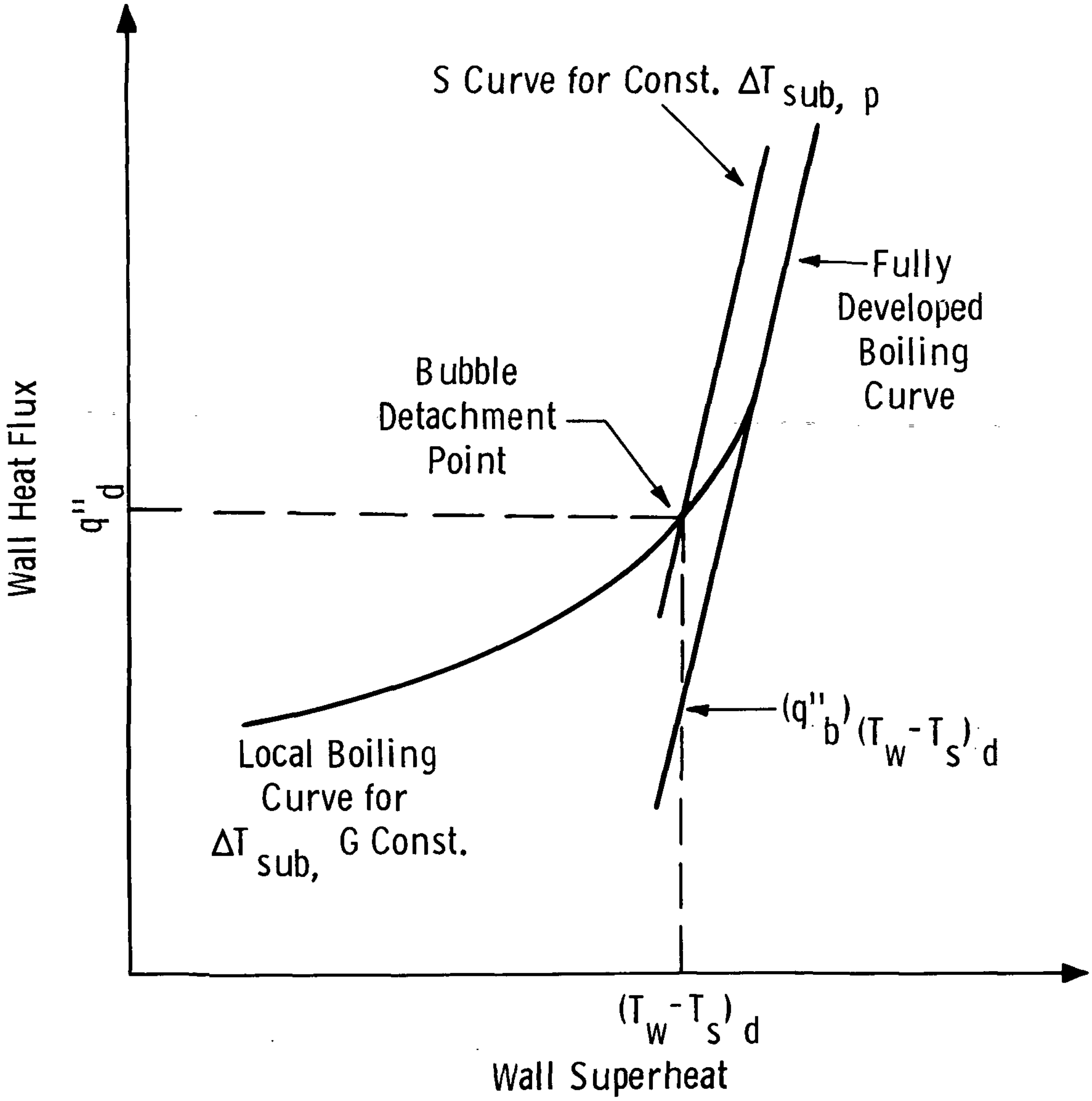

Fig. 28 —Graphical method of predicting bubble detachment using boiling curve information and subcooling parameter

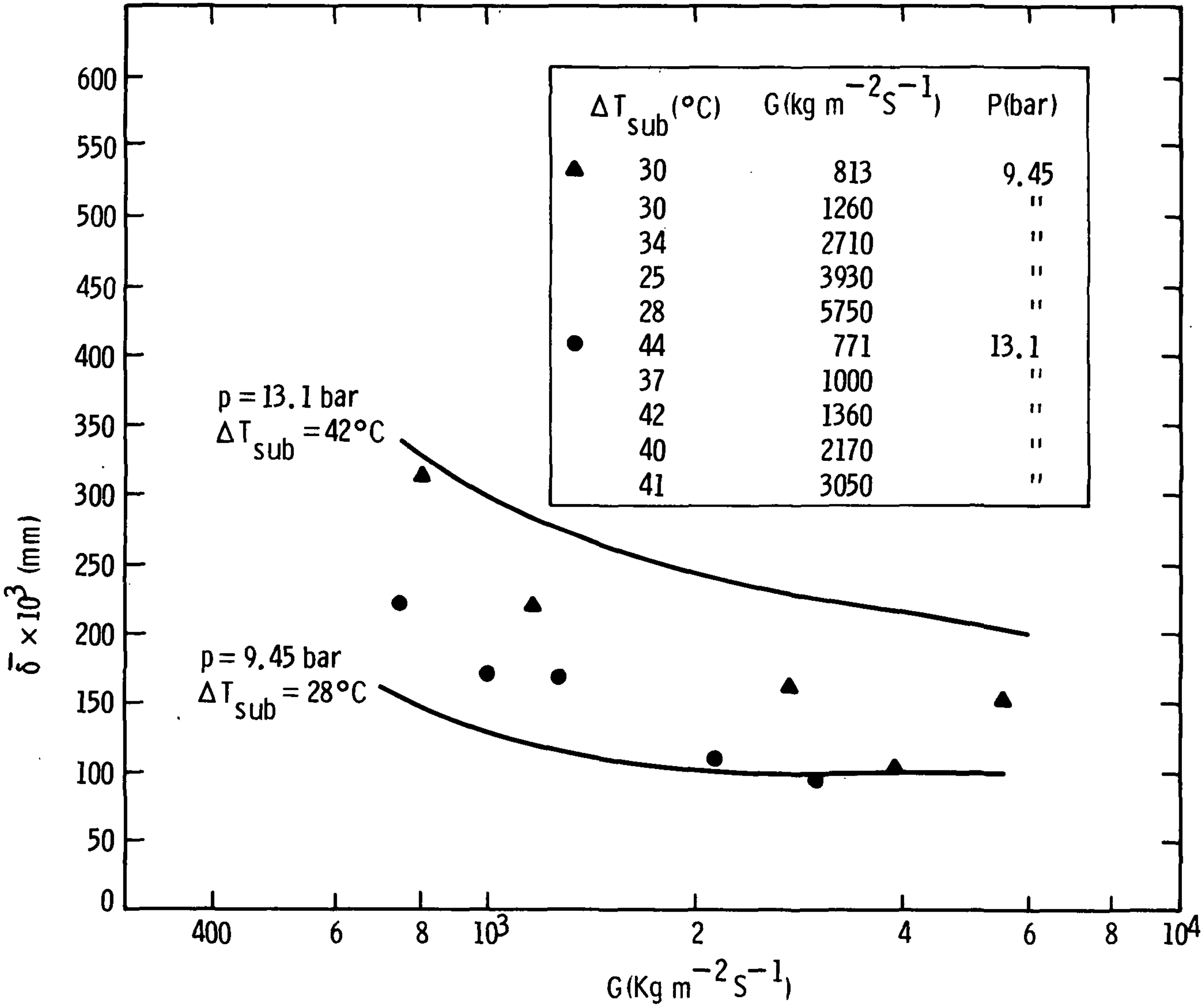

Fig. 29 – Comparison of the calculated and measured bubble layer thickness at bubble detachment, R–113

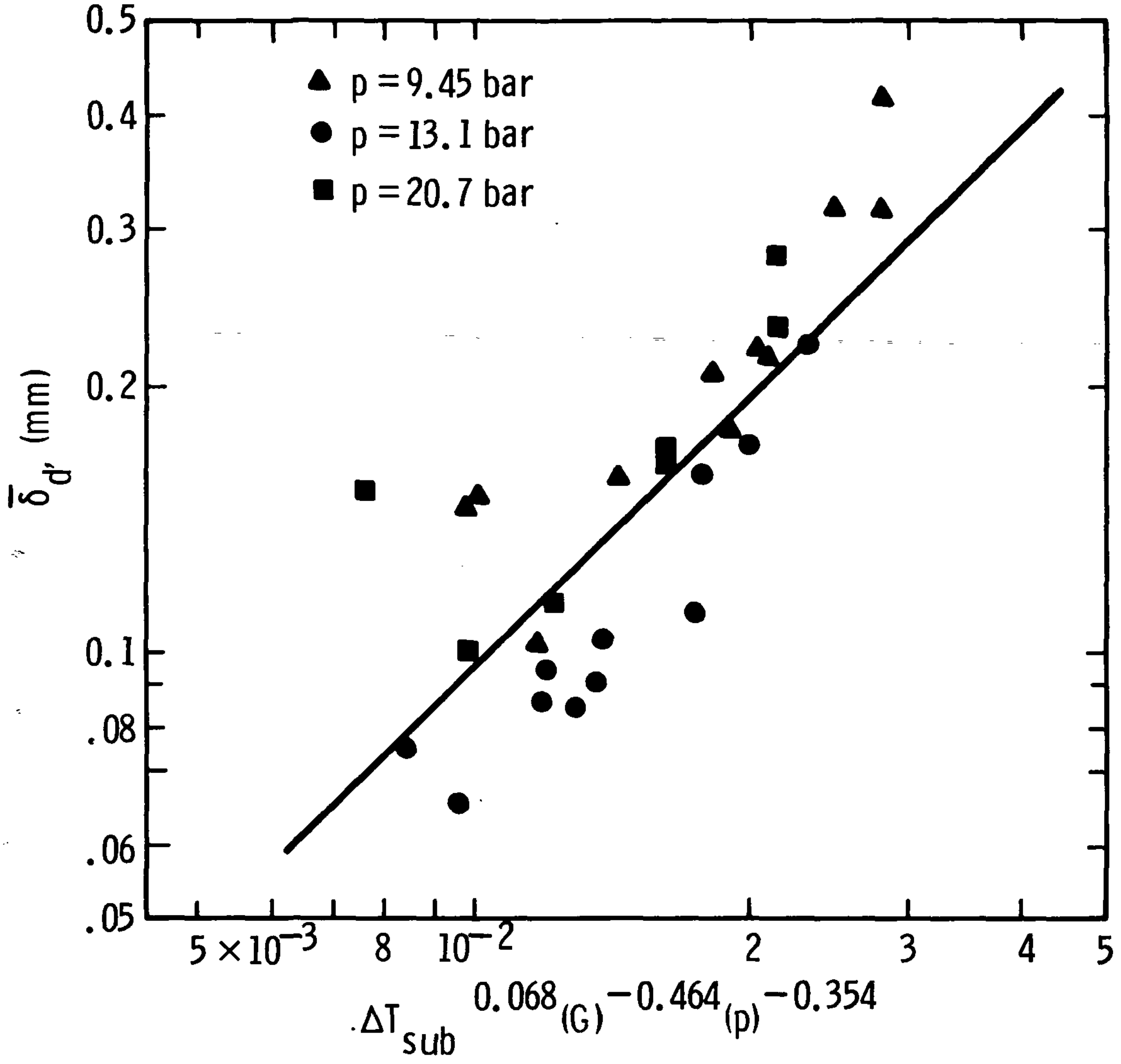

Fig. 30 — Correlation of the measured bubble boundary layer thickness at bubble detachment with major system parameters,

NASA-Langley, 1973 —— 33

NATIONAL AERONAUTICS AND SPACE ADMINISTRATION
WASHINGTON, D.C. 20546

OFFICIAL BUSINESS
PENALTY FOR PRIVATE USE $300

SPECIAL FOURTH-CLASS RATE
BOOK

POSTAGE AND FEES PAID
NATIONAL AERONAUTICS AND
SPACE ADMINISTRATION
451

U.S.MAIL

POSTMASTER : If Undeliverable (Section 158 Postal Manual) Do Not Return

---

> *"The aeronautical and space activities of the United States shall be conducted so as to contribute . . . to the expansion of human knowledge of phenomena in the atmosphere and space. The Administration shall provide for the widest practicable and appropriate dissemination of information concerning its activities and the results thereof."*
>
> —NATIONAL AERONAUTICS AND SPACE ACT OF 1958

NASA SCIENTIFIC AND TECHNICAL PUBLICATIONS

TECHNICAL REPORTS: Scientific and technical information considered important, complete, and a lasting contribution to existing knowledge.

TECHNICAL NOTES: Information less broad in scope but nevertheless of importance as a contribution to existing knowledge.

TECHNICAL MEMORANDUMS: Information receiving limited distribution because of preliminary data, security classification, or other reasons. Also includes conference proceedings with either limited or unlimited distribution.

CONTRACTOR REPORTS: Scientific and technical information generated under a NASA contract or grant and considered an important contribution to existing knowledge.

TECHNICAL TRANSLATIONS: Information published in a foreign language considered to merit NASA distribution in English.

SPECIAL PUBLICATIONS: Information derived from or of value to NASA activities. Publications include final reports of major projects, monographs, data compilations, handbooks, sourcebooks, and special bibliographies.

TECHNOLOGY UTILIZATION PUBLICATIONS: Information on technology used by NASA that may be of particular interest in commercial and other non-aerospace applications. Publications include Tech Briefs, Technology Utilization Reports and Technology Surveys.

Details on the availability of these publications may be obtained from:

SCIENTIFIC AND TECHNICAL INFORMATION OFFICE

NATIONAL AERONAUTICS AND SPACE ADMINISTRATION

Washington, D.C. 20546